Towards new hermeticity test methods for MEMS

Suzanne Costello (née Millar)

Submitted for Degree of Engineering Doctorate in Microsystems
Engineering

Heriot-Watt University

School of Engineering and Physical Sciences

July 2011

ABSTRACT

Hermeticity is a measure of how well a package can maintain its intended ambient cavity environment over the device lifetime. Since many Micro-Electro-Mechanical Systems (MEMS) sensors, actuators and microelectronic devices require a known cavity environment for optimum operational performance, it is important to know the leak rate of the package for lifetime prediction purposes. In this field, limitations in the traditional leak detection methods and standards used originally for integrated circuits and semiconductors have been blindly and often incorrectly applied to MEMS and microelectronic packages. The aim of this project is to define accurately the limitations of the existing hermeticity test methods and standards when applied to low cavity volume MEMS and microelectronic packages and to demonstrate novel test methods, which are applicable to such packages. For the first time, the use of the Lambert-W function has been demonstrated to provide a closed form expression of the maximum true leak rate achievable for the most commonly used existing hermeticity test method, the helium fine leak test. This expression along with the minimum detectable leak rate expression is shown to provide practical guidelines for the accurate testing of hermeticity for ultra-low volume packages. The three leak types which MEMS and microelectronic packages are subject to: molecular leaks, permeation and outgassing, are explained in detail and it is found that the helium leak test is capable of quantifying only molecular leak in packages with cavity volumes exceeding 2.6 mm^3. With many MEMS and microelectronic package containing cavities with lower volumes, new hermeticity test methods are required to fill this gap and to measure the increasingly lower leak rates which adversely affect such packages. Fourier Transform Infra-Red (FTIR) spectroscopy and Raman spectroscopy are investigated as methods of detecting gas pressure within MEMS and microelectronics packages. Measured over time, FTIR can be used to determine the molecular and permeation leak rates of packages containing infra-red transparent cap materials. Future work is required to achieve an adequate signal to noise ratio to enable Raman spectroscopy to be a quantitative method to determine molecular leaks, permeation leaks and potentially outgassing. The design, fabrication and calibration procedure for three in-situ test structures intended to monitor the hermeticity of packages electrically are also presented. The calibration results of a piezoresistive cap deflection test structure show the structure can be used to detect leak

rates of any type down to 6.94×10^{-12} atm.cm^3.s^{-1}. A portfolio of hermeticity test methods is also presented outlining the limitations and advantages of each method. This portfolio is intended to be a living document and should be updated as new research is undertaken and new test methods developed.

DEDICATION

This thesis is dedicated to my husband,

Laurie, with love and thanks

for all his support, encouragement,

understanding and for always believing in me.

ACKNOWLEGEMENTS

ACADEMIC REGISTRY

Research Thesis Submission

Name:	SUZANNE COSTELLO		
School/PGI:	School of engineering and Physical Sciences		
Version: *(i.e. First, Resubmission, Final)*	Final	Degree Sought (Award **and** Subject area)	Doctor of Engineering in Microsystems Engineering

Declaration

In accordance with the appropriate regulations I hereby submit my thesis and I declare that:
1) the thesis embodies the results of my own work and has been composed by myself
2) where appropriate, I have made acknowledgement of the work of others and have made reference to work carried out in collaboration with other persons
3) the thesis is the correct version of the thesis for submission and is the same version as any electronic versions submitted*.
4) my thesis for the award referred to, deposited in the Heriot-Watt University Library, should be made available for loan or photocopying and be available via the Institutional Repository, subject to such conditions as the Librarian may require
5) I understand that as a student of the University I am required to abide by the Regulations of the University and to conform to its discipline.

* *Please note that it is the responsibility of the candidate to ensure that the correct version of the thesis is submitted.*

Signature of Candidate:		Date:	

Submission

Submitted By *(name in capitals):*	
Signature of Individual Submitting:	
Date Submitted:	

For Completion in the Student Service Centre (SSC)

Received in the SSC by *(name in capitals):*			
Method of Submission (Handed in to SSC; posted through internal/external mail):			
*E-thesis Submitted (**mandatory for final theses**)*			
Signature:		Date:	

Table of Contents

List of Tables and Figures

TABLES

FIGURES

List of Publications

Journal Papers:

Millar, S., Desmulliez, M.P.Y. and McCracken, S., "Review of test methods for measurement of hermeticity in packages containing small cavities" accepted for publication to IEEE Advanced Packaging.

Millar, S., Desmulliez, M.P.Y. and McCracken, S., "Leak detection methods for glass capped and polymer sealed MEMS Packaging", *Journal of Microsystems Technology*, Vol 17, No 4, pp 677-684 (2011), DOI: 10.1007/s00542-010-1200-z.

Millar, S. and Desmulliez, M.P.Y., "MEMS ultra low leak detection methods: a review", *Sensor Review*, Vol 29, No 4, pp.339-344 (2009).

Conference Papers:

Millar, S. and Desmulliez, M.P.Y., "Ultra low leak detection methods for MEMS packaging" *Proceedings MicroTech 2009*, Edinburgh, (2009).

Millar, S., Desmulliez, M.P.Y. and Yu, W., "A review of hermeticity test methods for packages with small cavities (invited paper)", *Proceedings IMAPS - CPMT Poland 2009*, Gliwice, Pszczyna, Poland, (2009).

Lorenz, N., Millar, S. and Hand, D., "Localised laser joining of micro-devices for hermetic packaging using a glass frit intermediate layer", *Proceedings of the 5th International WLT-Conference on Lasers in Manufacturing*, Munich, (2009).

Lorenz, N., Smith, M.D., Millar, S., Desmulliez, M. and Hand, D.P., "Advances in laser based joining processes of micro-devices using localised heating", *28th International Congress on Applications of Lasers & Electro-Optics*, Orlando, FL, US (2009).

Millar, S., Desmulliez, M.P.Y. and McCracken, S., "Leak detection methods for glass capped and polymer sealed MEMS packages," *Proceedings of Design, Test, Integration and Packaging,* Seville, Spain (2010).

Lorenz, N., Millar, S., Desmulliez, M, and Hand, D.P., "Laser based vacuum packaging of micro-devices using localised heating", *Proceedings of LPM2010 - the 11th International Symposium on Laser Precision Microfabrication,* Stuttgart, Germany (2010).

Millar, S., Desmulliez, M.P.Y., Cargill, S., and McCracken, S., "In-situ test structures for ultra low leak detection," *Electronic System-Integration Technology Conference (ESTC),* pp.1-4, (2010).

Chapter 1

Introduction and Thesis Outline

1.1   Introduction

Leak detection of small semiconductor, integrated circuit and microelectronic packages started in the 1960's when it was observed that corrosion of devices occurred when moisture levels in the package cavity exceeded 5000 ppm [1.1]. The helium leak test was firstly used to determine the leak rate of packages. In those days, the typical volume of the package cavity volume was 0.1 cm^3, and a helium leak rate of 5×10^{-10} atm.cm^3.s^{-1} ensured that no more than 5000 ppm moisture would ingress into the cavity over a typical device lifetime of 8 years [1.2]. Mass spectroscopy at that time permitted the detection of leak rates between 1×10^{-6} and 1×10^{-8} atm.cm^3.s^{-1} helium. To allow the use of the test method, it was agreed that the maximum permissible leak rate of packages should be increased beyond the calculated safe leak rate into the detectable range of the test method [1.2]. This was the beginning of a series of concerns regarding the determination of package leak rates and the definition of 'hermeticity'. Whilst no package is completely hermetic, many can be regarded as sufficiently hermetic for the environment in which they operate, the sensitivity of the device which they protect and the expected lifetime of the device.

The main objective of a traditional integrated circuit, semiconductor or microelectronic package is to keep moisture out of the package. Water alone is not corrosive but the combination of ionic contaminants and available moisture renders this mixture corrosive [1.1]. Reducing water content simply reduces the mobility of corrosive ionic contaminants, hence increasing mean time to failure. MEMS packages, in that regard, must not only prevent moisture ingress but also allow environmental interaction with the outside world to enable the MEMS to act as a sensor or actuator [1.3]. Some MEMS also require more stringent protection from moisture to minimise failure due to stiction. Packages containing a vacuum cavity must have ultra low leak rates to maintain the vacuum necessary for optimum performance of the device. For these reasons MEMS are generally wafer level bonded before dicing to ensure as hermetic a

package as possible. This often means lower cavity volumes which require an even lower leak rate to ensure hermeticity, particularly in vacuum applications. Advances in microelectronics technology have also meant a reduction in free cavity space in packages resulting in a minimum leak rate requirement which current hermeticity test methods are not able to detect. A typical MEMS package has a volume of 0.1 mm^3, a sealed cavity pressure of 10^{-2} atm, a lifetime of 5 years and an acceptable pressure increase over this lifetime of 10%. Using the standard definition of leak rate, L, represented by equation 1.1, the maximum acceptable leak rate of this package is 6.34×10^{-16} atm.cm^3.s^{-1}. This leak rate is several orders of magnitude lower than the minimum detectable leak rate of traditional hermeticity test methods.

$$L = \frac{\Delta PV}{t} \qquad\qquad (1.1)$$

where ΔP is the maximum acceptable change in cavity pressure over the device lifetime, V is the volume of the cavity and t is the device lifetime.

Other types of MEMS have been developed for biotechnology and consumer applications which have different packaging requirements. These do not necessarily need hermetic packaging and so new packaging materials and techniques are being developed. These new 'near-hermetic' or 'quasi-hermetic' packages are able to protect against moisture ingress but are fabricated using materials which are permeable to gases [1.3]. Knowledge of the leak rate of these packages is still therefore required to aid lifetime prediction but conventional test methods are not suited to quantifying leak rates caused by permeation.

In contrast, some complex MEMS requiring ultra high vacuum packaging are also being developed, often for military and aerospace applications where long lifetime and exceptionally low leak rates are essential. Outgassing from internal material layers can become a dominant leak source in this type of package especially when hermetic packaging methods have been fully optimised [1.4].

This thesis presents the novel determination of the theoretical limits of the traditional helium leak test method. This work is intended to provide a boundary for use of traditional hermeticity test methods and ensure that users understand which leak types

the traditional test methods are detecting. This work highlights also the package types and leak types that cannot be assessed using traditional tests. Three in-situ test structures have been designed, fabricated and calibrated to provide a solution to the hermeticity testing problem for low cavity volume and ultra high vacuum packaging. This thesis presents the first use of thermal van der Pauw and piezoresistive cap deflection test structures for the determination of package hermeticity. The third test structure, the micro-Pirani gauge has been used for this purpose previously by Dr Brian Stark [1.5]. To determine fabrication compatibility with a standard MEMS foundry process, a micro-Pirani gauge has been fabricated using the same multi-project wafer service as the other test structures. The sensitivity and accuracy of the micro-Pirani gauge for hermeticity testing purposes are compared to those of the other test structures. Optical test methods proposed by other research groups have also been further characterised to determine their suitability for use with specific package types.

There is a lack of literature in this field, the only textbook currently available on this subject, to the best of the author's knowledge, is *Hermeticity of Electronic Packaging* by Hal Greenhouse [1.1]. In view of new research, new package types, new understanding of leak types and hermeticity testing methods, some parts of this reference text require significant updating and correction. The industry standards used to regulate the way in which the traditional test methods are used to measure hermeticity are out-of-date, particularly with regards to the cavity volumes of interest. These standards require updating to ensure accurate hermeticity testing of ultra low cavity packages. Throughout this project the author of this thesis has been part of a task force led by Ron Foster of Axept, Steve Martell of Sonoscan and supported by SEMI to produce an international standard for hermeticity testing covering leak channel testing of low cavity volume packages, permeation rates and outgassing. Results of this task force are expected in late 2011.

In summary, this thesis aims to show the theoretical and practical limitations of traditional and newly proposed hermeticity test methods when applied to low cavity volume packages. Novel test structures are proposed as a solution to the hermeticity testing problems for ultra-low volume, vacuum packaged cavities. This thesis contains the theory behind leak testing and information about the practical implications associated with the test methods. For this reason, this thesis can also be considered as an

updated reference of hermeticity testing issues and solutions for packaging engineers in industry and research alike.

1.2 Thesis Outline

The outline of this thesis is depicted using the following flow chart.
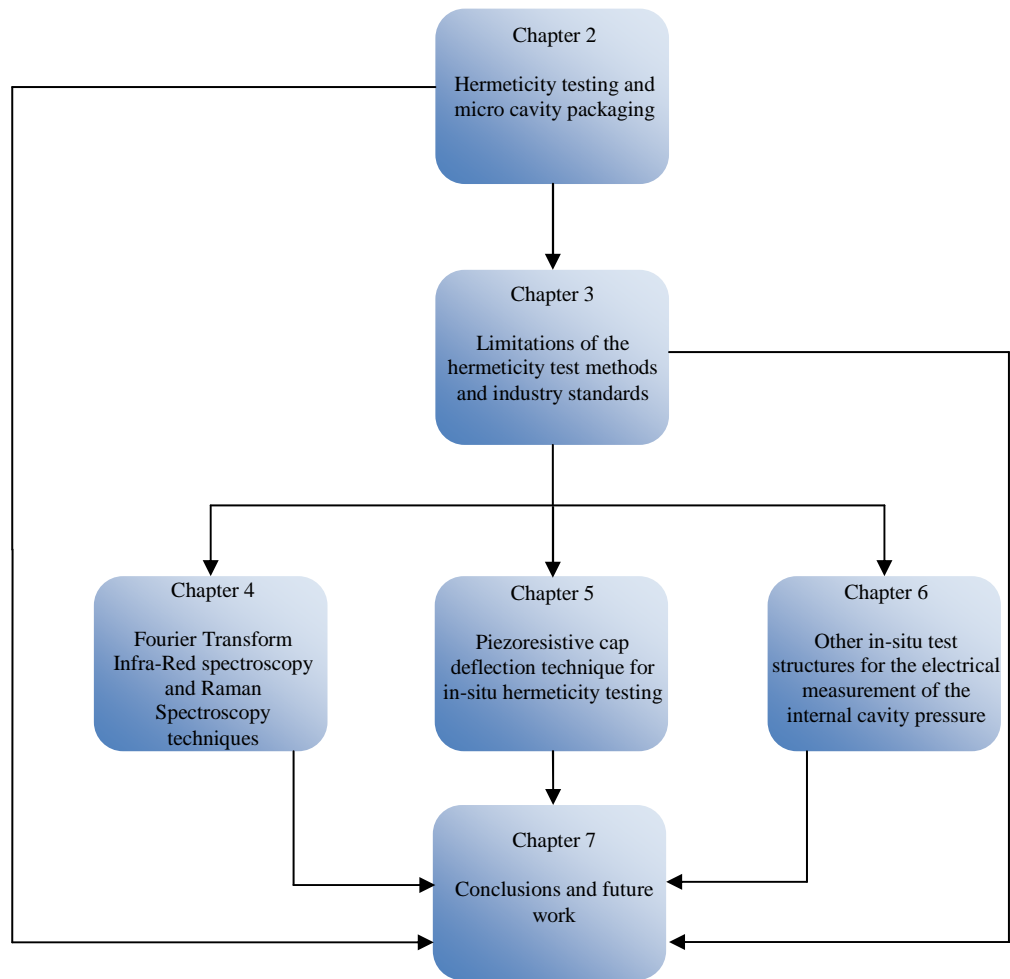
Figure 1.1: Flow chart of thesis outline.

- Chapter 2 provides background on traditional hermeticity test methods and micro-cavity packaging. One section of this chapter describes the history of MEMS, reviewing technology and packaging developments, test methods and revisions of the standards throughout the years. This section aims to show how hermeticity testing has developed with the ever changing products of the microelectronics industry and the introduction of MEMS. Chapter 2 also

describes the type of packaging materials and techniques used in the microelectronics and MEMS industries. Traditional hermetic packaging materials and techniques are described firstly and the relatively recent introduction of 'near-hermetic' or 'quasi-hermetic' packaging materials and techniques are explained. Traditional hermeticity test methods such as helium fine leak testing, radioactive isotope leak detection and various gross leak detection methods are also described in Chapter 2. Added in the later versions of the military standards, optical leak detection and cumulative helium leak detection (CHLD) are explained. A description of the leak types associated with both hermetic and non-hermetic packages concludes this chapter. The mathematical description of the flow mechanisms is provided to enable a distinction between the different types of leak and highlight the need for new hermeticity test methods.

- Chapter 3 provides the theoretical and practical limitations of the existing hermeticity test methods given in the standards. This chapter aims to show the absolute limits of these tests when applied to MEMS and low cavity volume microelectronic packages. This chapter will also discuss the leak detection requirements of the MEMS industry by examining a market study compiled to establish hermeticity testing needs of the MEMS industry.

- Developments made in the use of Fourier Transform Infra-Red (FTIR) spectrometry and Raman spectroscopy as hermeticity test methods are provided in Chapter 4. The practical and theoretical limitations for the use of these test methods with MEMS and low cavity volume microelectronics are shown.

- Chapter 5 presents the design, fabrication and calibration of a peizoresistive cap deflection in-situ test structure designed to give an electrical response to changing cavity ambient pressure. This test structure is designed to give quick results and a more sensitive measurement of leak rate using the package cap as the test structure.

- The theory, design and calibration of two more in-situ test structures; the micro-Pirani and thermal Van der Pauw test structure are described in Chapter 6.

- The overall conclusions and results of this work are summarised in Chapter 7. Future work and research opportunities are then proposed.

1.3   References

[1.1]   H. Greenhouse, '*Hermeticity of Electronic Packages*', William Andrew publishing, 2000.

[1.2]   F.N. Sinnadurai, '*Handbook of Microelectronics Packaging and Technologies*', Electrochemical Technologies, 1985.

[1.3]   M.J. Madou, '*Fundamentals of Microfabrication. The Science of Miniturization*', Second Edition, CRC Press LLC, 2002.

[1.4]   M. Moraja, '*Hermetic Packaging Design of MEMS*', FSRM Courses in Microtec and Nanotec, 2010.

[1.5]   B.H. Stark, J. Chae, A. Kup, A. Oliver and K. Najafi '*A high-performance surface-micromachined pirani gauge in SUMMIT V*', 18th International Conference on Micro Electro Mechanical Systems, 2005.

Chapter 2

Hermeticity Testing and Micro-Cavity Packaging

2.1   The history of hermeticity testing

The methods currently available for hermeticity testing of low cavity volume packages are listed and regulated by several standards such as the US Military Standards MIL-STD-883H T.M.1014.13 and MIL-STD-750E T.M.1071.8. European standards also exist although they are largely based on the US military standards. In both industry and academia, MIL-STD-883H TM1014.13 is the most commonly used to determine the hermeticity of packages.

In figure 2.1, a timeline shows the introduction and enhancement of these standards throughout the years. The first use of leak test methods are noted along with the new technologies that led to improvements in testing accuracy and the extension of the detectable range of the test methods. On the same timeline, the most significant developments of technology used in the microelectronics and MEMS industries are shown to highlight the changes in package materials and cavity volumes since the 1950's. The response of industry to changing packaging and testing requirements are also noted.

Advances in microelectronics and MEMS technologies	1940's	1950's	1960's	1970's	1980's	1990's	2000's
	• 1ˢᵗ transistor: AT&T Bell Laboratories **(1947)**	• 1ˢᵗ IC is developed by Texas Instruments **(1958)**	• 1ˢᵗ ceramic flat packages and development of dual in-line package • Anisotropic etching is developed **(1967)** • Moore's law is presented **(1968)**	• National Semiconductor High volume pressure sensor production **(1974)**	• LIGA process developed • 1ˢᵗ polysilicon MEMS **(1984)** • Sacrificial layer technology is applied to micromachines **(1985)**	• Deep Reactive Ion Etching (DRIE) developed • Pister, UCLA 1ˢᵗ micromachined hinge – pseudo 3D structures **(1992)**	• Introduction of RF MEMS and BioMEMS

Inventions leading to advances in leak detection	1940's	1950's	1960's	1970's	1980's	1990's	2000's
	• Helium leak detector invented. Min. detectable leak rate = 10^{-6} atm.cm^3.s^{-1} **(1947)**	• 1ˢᵗ use of radioisotope fine leak test. **(1959)**	• Creation of first military standards for hermeticity testing. • Sinnadurai develops HAST at BT as packages passing MIL-STD-883 fail due to moisture ingress. **(1968)**	• Turbomolecular vacuum pump is invented – helium leak min. detectable leak rate = 10^{-9} atm.cm^3.s^{-1} • Flexible method for Helium leak detection introduced to Military standards **(1974)**	• Sinnadurai's work is published and plastic packaging proves more reliable in tropical surroundings.	• Optical leak detection added to MIL-STD-883 TM 1014 . **(1995)**	• Dry pump invention - helium leak min. detectable leak rate = 10^{-11} atm.cm^3.s^{-1} • Cumulative helium leak detection added to MIL-STD-750 TM 1071 **(2007)**

Figure 2.1: Timeline showing the history packaging and hermeticity test methods. Important landmarks in electronics and MEMS technologies are indicated on the time chart for completeness.

8

2.1.1 The history of microelectronics and MEMS technology development

The first transistor, shown in figure 2.2, was invented by William Shockley, John Bardeen and Walter Brattain of AT&T Bell Laboratories in 1947 [2.1]. The three inventors shared the Nobel Prize in Physics for their research into semiconductors and their discovery of the transistor effect in 1956. The first working integrated circuit, shown in figure 2.3, was demonstrated at Texas Instruments in 1958 by Jack Kilby [2.2]. Kilby also won the Nobel Prize in Physics in 2000 for his part in the invention of the integrated circuit. The idea was first published by Geoffrey W.A. Dummer who worked for the British Ministry of Defence in 1952 [2.3]. Robert Noyce of Fairchild Semiconductor is also credited with developing an integrated circuit made of silicon, 6 months after Kilby's invention was publicised [2.4].
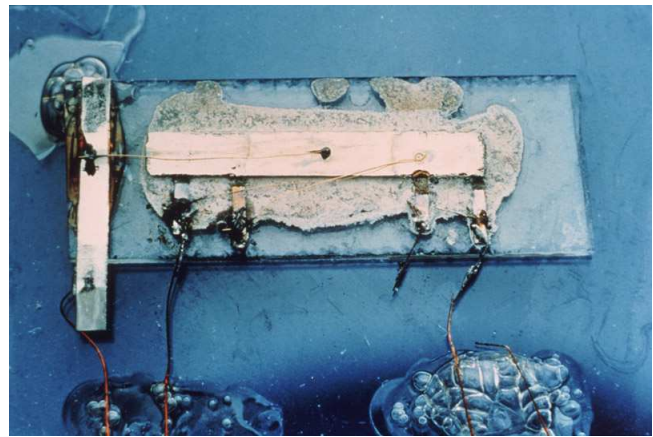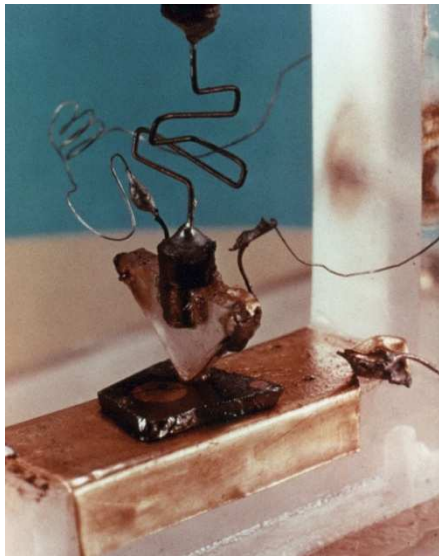
Figure 2.2: (left) the first transistor [2.5]. Figure 2.3(right) the first integrated circuit [2.6]

With continuing development in fabrication processes for IC manufacture, Gordon E. Moore gave his prediction in 1965, as shown in figure 2.4, stating that the number of transistors that can be inexpensively placed on an integrated circuit will double every two years for at least ten years [2.7]. Moore's law has been a fundamental driving force behind technological advances and the trend has continued through five decades and is not expected to stop until at least 2015 [2.8].

9
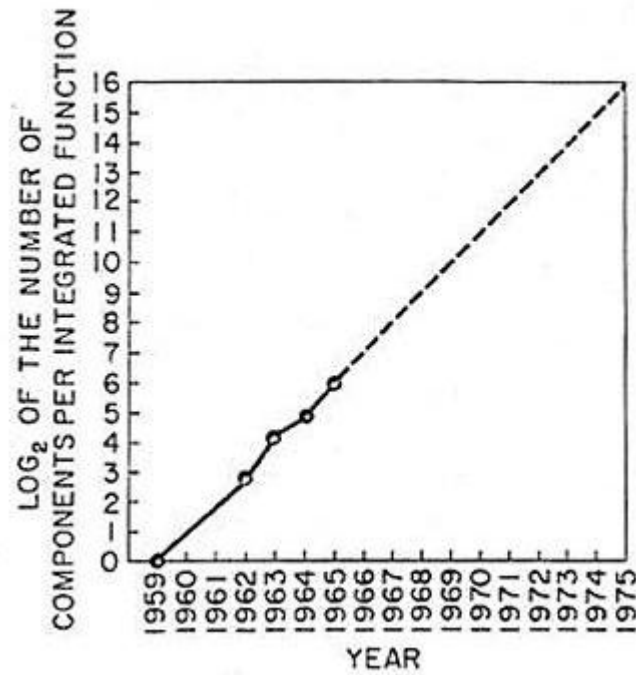
Figure 2.4: Moore's law [2.9]

In 1967, anisotropic etching was first developed by Bell laboratories. Wet etching however dates back to the 15th century when wax masks and acid based etchants were used to decorate armour. In 1822, Niépce developed photosensitive masks introducing a new level of tolerance to etching capabilities. During the Second World War, lithography based etching was used in printed circuit board, PCB, manufacture and, in 1961, the method was applied to silicon integrated circuits. Silicon can be isotropically wet etched using HF with HNO_3 to produced small, flat structures with aspect ratios of 2:1. This was generally adequate for the IC industry but Bell Laboratories set about developing anisotropic etching to allow higher aspect ratio etching in silicon to dielectrically isolate structures. In the 1970's the development of anisotropic etching led to V-groove and U-groove transistors. Silicon can be anisotropically etched using KOH and water. Figure 2.5 shows the differences between isotropic and anisotropic etching. In anisotropic etching there is little under etch as long as the mask has been aligned correctly. Anisotropic etching therefore gives a much tighter lateral control as well as thickness control of around 1μm. 300 μm to 500 μm silicon wafers can be anisotropically etched down to form diaphragms 10 μm to 20 μm thick. Depending on the crystalline orientation of the silicon substrate and the direction of mask alignment, various patterns can be etched into the silicon due to significantly different etch rates in different facet directions. This quality allows long narrow grooves with perpendicular

10

edges to be formed in [110] silicon, making this silicon orientation very useful in microsystems where high aspect ratio etching is often required. V-grooves and U-grooves can be formed in [100] silicon. Although [111] silicon is sometimes used in the IC industry, it is not easily wet etched. Anisotropic etching is however a slow process with etch rates of 1µm per minute or less, making the process expensive and time consuming. It is a temperature sensitive process but is not sensitive to agitation [2.10].
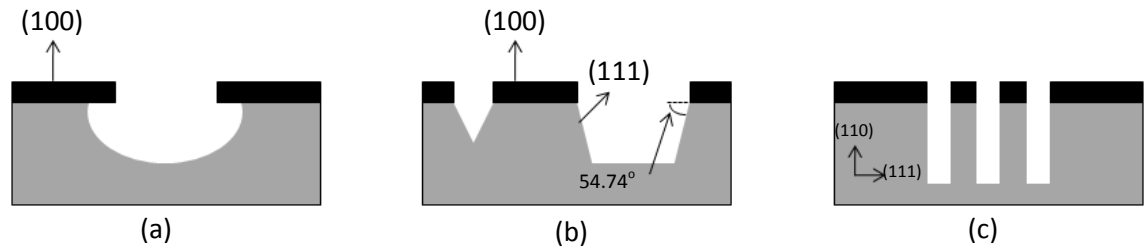
Figure 2.5 (a) isotropic etch in [100] silicon, (b) anisotropic etch in [100] silicon, (c) anisotropic etch in [110] silicon.

In 1974, National Semiconductor Corporation manufactured the first micromachined silicon pressure sensor and released the first silicon pressure transducer catalogue, closely followed by Honeywell, Foxboro/ICT, Endevco and Kulite [2.10]. Other types of micromachined structures started to be developed in the late 1970's with the first polysilicon MEMS developed in 1984 by Howe and Muller [2.11].

In 1985, sacrificial layer technology was applied to microsystems aiding the realisation of RF-MEMS in the 1990's [2.12]. At the same time, Deep Reactive Ion Etching, DRIE, was developed and the major limitations of anisotropic etching were overcome. Etch rates were dramatically increased, higher aspect ratios at depths greater than tens of microns could be achieved [2.10].

Currently, integrated circuit technology is still developing in accordance with Moore's Law. In the mid 1990's however, the MEMS industry underwent a change from standard silicon substrate based technology to include bioMEMS [2.10]. This meant a whole new market for micromachined products and this market still continues to grow as new technology is developed to process biocompatible materials. As fabrication technologies approach their limits and transistor dimensions can be reduced no further, the next stage in technology development calls for further functionality in micro and nanoelectronics. This type of trend is often referred to as 'more than Moore' and

incorporates post processing and integration of non-digital functionality into semiconductor products [2.13].

2.1.2 The history of microelectronics and MEMS packaging development

The first microelectronic devices were packaged in metal cases significantly larger than the device itself. These packages were hermetic and designed specifically to keep contaminants like water from entering the package and degrading the components. The first ceramic flat packages were introduced in the 1960's and were used for many years for military applications due to their high reliability. Ceramic, later plastic, dual in line packages (DIP) were developed in 1964 by Bryant Rogers of Fairchild Semiconductors for commercial applications. Throughout the 1980's the need for higher pin counts led to the development of the pin grid array (PGA) package, the ball grid array (BGA) package and small outline integrated circuits (SOIC) which occupied 30-50% less area and were 70% thinner than an equivalent DIP. In the 1990's packages were further developed with flip-chip ball grid array (FCBGA) packages, plastic quad flat packages (PQFP) and thin small outline packages (TSOP) providing even higher pin counts over smaller areas with lower profiles [2.14].

Packaging of MEMS is more challenging as these packages must not only meet the requirements of the integrated circuits such as power distribution, signal redistribution, mechanical stability and thermal management but also allow interactions with the external environment to measure or affect physical or chemical parameters [2.10]. The maximum permissible leak rate of a standard microelectronics package is based on the leak rate necessary to prevent ingress of more than 5000 ppm of moisture inside the package [2.15]. MEMS packages must often keep the moisture level even lower to prevent stiction of moveable parts and fogging of optical elements. The leak rate of MEMS packages must be especially low in the case of resonant MEMS as the package is required to ensure the integrity of a vacuum cavity over the device lifetime. The MEMS industry is still searching for a packaging method offering a solution to the problem of protecting the device circuitry and maintaining an ambient operating environment whilst enabling sensor or actuator interaction with the environment. For this reason, up to 70% of the costs of MEMS manufacture is in packaging and finding adequate packaging methods remains the greatest barrier to successful commercialisation of MEMS.

12

Despite these drawbacks, some MEMS device types have been extremely successful and have been bulk manufactured for over thirty years. The first commercially available MEMS devices were pressure sensors closely followed by accelerometers. Packaging of pressure sensors and inertial devices is more straightforward due to the effects that are to be measured. In the case of accelerometers and other physical sensors, the device and circuitry can be protected from the environment using hermetic packaging methods whilst the inertial effects the sensor measures are probed [2.10]. One of the most complex MEMS to package are those designed for chemical sensing and bioMEMS applications. To date, a hybrid MEMS solution whereby the MEMS and circuitry are fabricated on different substrates and combined in a package, such as DIP, is most commonly adopted for these applications [2.10].

Microsystems or MEMS are often cavity sealed to allow mechanical freedom for moveable parts and to allow resonant structures to be sealed in a vacuum environment. Bulk micromachining and silicon fusion bonded surface micromachining techniques were used firstly to create sealed cavities. This involves the anodic or direct fusion of glass or silicon substrate caps to etched cavities in silicon as shown in figure 2.6. Due to the thickness of the cap this cavity seal method is not suitable for die feature level (zero level) packaging [2.10].

Silicon/Polysilicon wafer

Bonding interface, covalent bond between suface oxide OH groups

Silicon wafer
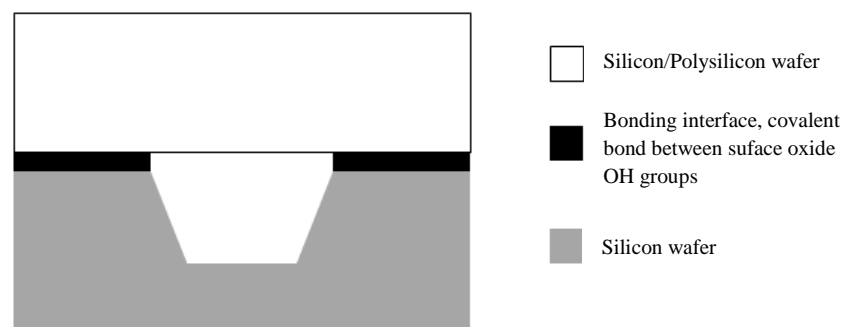
Figure 2.6: Cavity sealing using bulk micromachining

With the introduction of surface micromachining and polysilicon MEMS in the 1980's came a new way to seal cavities as an integral part of the fabrication process. As shown in figure 2.7, a micromachined surface package can be made by creating thin gaps between the substrate and structured cap using a sacrificial layer, often phosophosilicate glass (PSG) [2.10]. When this sacrificial layer is etched away, a thin gap of the order of 100 nm is formed [2.10]. These gaps can then be sealed by a number of methods

including reactive sealing which involves thermal oxidation of the polysilicon cap and silicon substrate at 1000°C [2.10]. These developments proved to be useful in the IC industry also and enabled a reduction in the cavity volume of many MEMS and IC packages [2.10].
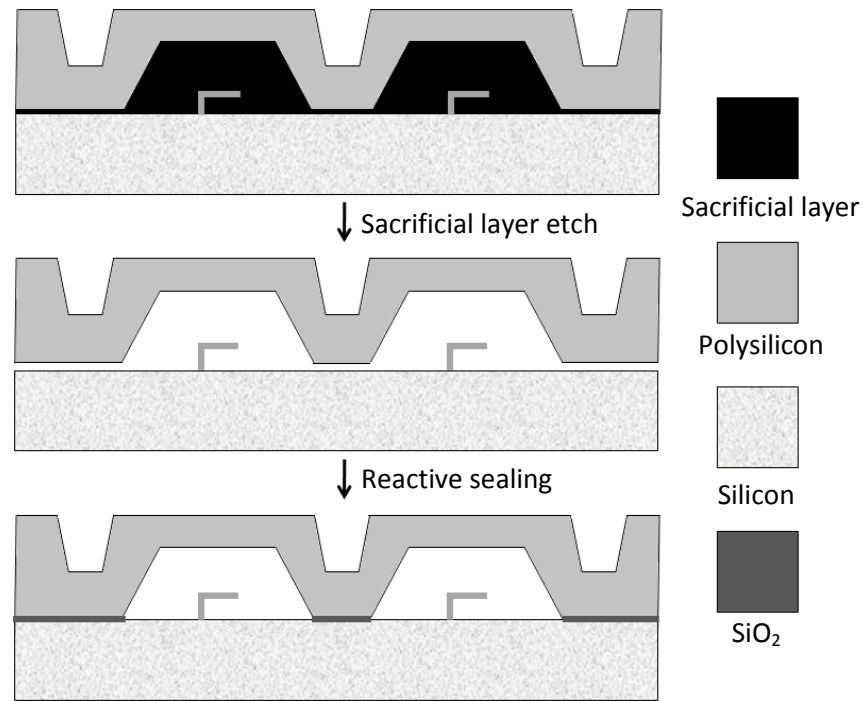
Figure 2.7: Cavity sealing using surface micromachined polysilicon [2.10]

With the development of bioMEMS and the demand for low cost consumer MEMS products, MEMS packaging methods began to expand in the late 1990's and 2000's. The need for biocompatibility meant that silicon was not always the first choice material and polymers began to be of interest. For low cost, short lifetime consumer applications, the focus of MEMS product engineers was to reduce the cost of packaging. New 'near-hermetic' or 'quasi-hermetic' packages were becoming increasingly attractive to this section of the industry. Some polymer materials were discovered to have low moisture permeation properties, making them hermetic enough for short lifetime, less sensitive MEMS devices. Less hermetic packaging methods also have the added benefit of lower sealing temperature and pressures making them more suitable for some applications. Research and development of this type of packaging is on the increase and so the advantages and disadvantages of these methods continue to be debated amongst the MEMS community.

2.1.3   The history of hermeticity test methods and standards

In 1947 the helium fine leak detection method was developed and used to measure small leaks in the gas diffusion process of uranium enriched plants. The method was developed by Nier et al. involved in the Manhattan Project to develop the first atomic bomb during World War II [2.16]. The method was originally capable of measuring leaks rates down to 10^{-7} Pa.m^3.s^{-1} (10^{-6} atm.cm^3.s^{-1}) or one part of helium in 200,000 parts of air [2.16]. The units of leak rate are commonly given as atm.cm^3.s^{-1}, mbar.l.s^{-1} or in SI units Pa.m^3.s^{-1}. Conversion factors are provided in Appendix A. This method of leak detection was used to determine the leak rate of the first IC packages. Packages are pressurised in helium then transferred to a chamber attached to a vacuum pump and helium mass spectrometer. The amount of helium leaking out of the package is quantified and the hermeticity of the package assessed. This method has to be used along with a gross leak test capable of measuring leak rates larger than those which can be detected by the helium test. In that respect, the liquid fluorocarbon gross test is most commonly used. This test involves pressurising the package in an indicator fluid with a low boiling point and transferring it to a detector fluid with a higher boiling point. The detector fluid is heated to a temperature below its own boiling point yet higher than that of the indicator fluid. Observation of bubbles coming from the package indicates a gross leak [2.17].

The use of the radioisotope fine leak test was first recorded in 1959. The method involves the sample being pressurised in an inert gas, N_2, containing a weak concentration of radioisotope, Kr-85. The gamma rays emitted from the sealed cavity are then counted to determine the leak rate and hermeticity of the package [2.18]. This test is thought to be a faster, more accurate fine leak test method although the initial set-up is expensive and an Atomic Energy Commission Licence is needed in the USA for possession and use of the equipment. For these reasons, industry has been relatively reluctant to adopt this method and helium leak testing is still most commonly used.

In the late 1960's the first standards to regulate the use of hermeticity test methods were created. The military standard, MIL-STD-883, T.M.1014, was initially made available and MIL-STD-750, T.M.1071, followed shortly afterwards.   Lack of package hermeticity became a concern when it became apparent that ingress of moisture caused

corrosion of devices. In fact, device failure has yet to be correlated to moisture ingress alone but extensive studies have shown that ionic contaminants combined with the availability of water leads directly to corrosion [2.15]. The general consensus in the industry is that moisture content should be kept below 5000 ppm or 3 monolayers of water on the internal walls of the package to minimise device corrosion, allowing thereby the calculation of the respective permissible leak rate [2.15]. Detailed reliability studies conducted at the time identified that typical devices required packaging with leak rates lower than 4.935×10^{-11} atm.cm^3.s^{-1} [2.19]. Leak detectors however were incapable of measuring such low leak rates and specification therefore had to be set orders of magnitude higher [2.19].

In 1968 British Telecommunications Laboratories noticed that some apparently 'hermetic' packages failed due to environmental contamination in tropical, humid environments such as those typical in India. Professor Nihal Sinnadurai worked on this problem and developed a test method now commonly known as HAST, high accelerated stress technique, to determine the packages which could best protect devices under extreme conditions. Around the same time, plastic packages were beginning to be developed by R&D departments, particularly in the telecoms industry. Sinnadurai discovered that many plastic packages were in fact better able to survive these harsh conditions than those deemed hermetic according to military standards. Initially, sceptics thought that plastic packages would be prone to contamination issues and moisture diffusions and so plastic packaging was quickly condemned in favour of traditional 'hermetic' packaging. Further work continued at BT in collaboration with plastic manufacturing companies and it was soon found that some plastics could offer reliable packaging solutions for integrated circuits. Sinnadurai's work was published in the early 1980's and further development of plastic packages continued [2.19].

During this time, the turbomolecular vacuum pump was invented and allowed the minimum detectable leak rate of the helium fine leak test method to be reduced to around 10^{-9} atm.cm^3.s^{-1} [2.20]. In 1974, the flexible method for determining the equivalent standard leak rate of packages was introduced to the military standards. This method, based on the Howl-Mann equation [2.21] described in later chapters, allows the actual test conditions to be input to the equation; the original test method had to be conducted according to specific test conditions [2.22, 2.23]. The flexible method is now preferred as it allows for more accurate testing and flexible test conditions.

The leak rate given by the helium leak detector is known as the measured leak rate. The standard leak rate is defined as the quantity of dry air at 25°C flowing through a leak where the high pressure side is 1 atm and the low pressure side is 1.316×10^{-3} atm (1 mmHg). The equivalent standard leak rate is the leak rate which would exist in a package with a given measured leak rate under standard leak rate conditions.

In 1995, optical leak detection was included in the military standards. This method involves the optical measurement of deflection of the lid of the package under certain external pressure conditions [2.24]. Further developments in vacuum technology, in particular the invention of the dry pump, led to further reductions in the minimum detectable leak rate of the helium fine leak test down to around 10^{-11} atm.cm^3.s^{-1}[2.20]. In 2007, cumulative helium leak detection (CHLD) was added to MIL-STD-750E T.M.1071.8 [2.25] and, in February 2010, to MIL-STD-883H T.M.1014.13 [2.22]. This method claims to be able to cover the leak range from gross leaks down to 4×10^{-14} atm.cm^3.s^{-1} [2.25]. Some controversy surrounding this test is discussed in section 2.3.

In summary, the microelectronics and MEMS industries have developed significantly since the invention of the transistor in 1947. Packaging of these devices has not been without controversy with many in industry and academia still preferring to house devices in traditional 'hermetic' packages. For some applications, such packaging is certainly still applicable but, with reducing cavity volumes, these packages now require lower leak rates to ensure hermeticity over the desired device lifetime. Hermeticity test methods and the standards used to regulate these have not managed to keep up-to-date with the new types of package, techniques and materials being used in industry. Figure 2.8 shows the detectable leak ranges of existing hermeticity methods and the maximum permissible leak rates of typical MEMS and microelectronic packages. MEMS structures are not only sensitive to the corrosive effects that moisture ingress promotes but are also subject to stiction of moveable parts, fogging of optical elements and changes in Q-factor due to pressure increase. Maximum acceptable leak rates for MEMS cavity volumes are therefore often lower than those in microelectronics. Plastic and polymer packaging has also proven to be applicable to microelectronic and MEMS packaging. However, as new packaging materials and techniques are employed in MEMS and microelectronic industries, one should be aware of the limitations of the existing hermeticity test methods to quantify the leak rates of these packages due to the significantly different flow mechanism involved as discussed in section 2.4 of this

chapter. For example, ultra high vacuum packaging of MEMS presents new challenges as outgassing from internal material layers becomes significant and detection becomes increasingly important to quantify the loss of vacuum integrity.
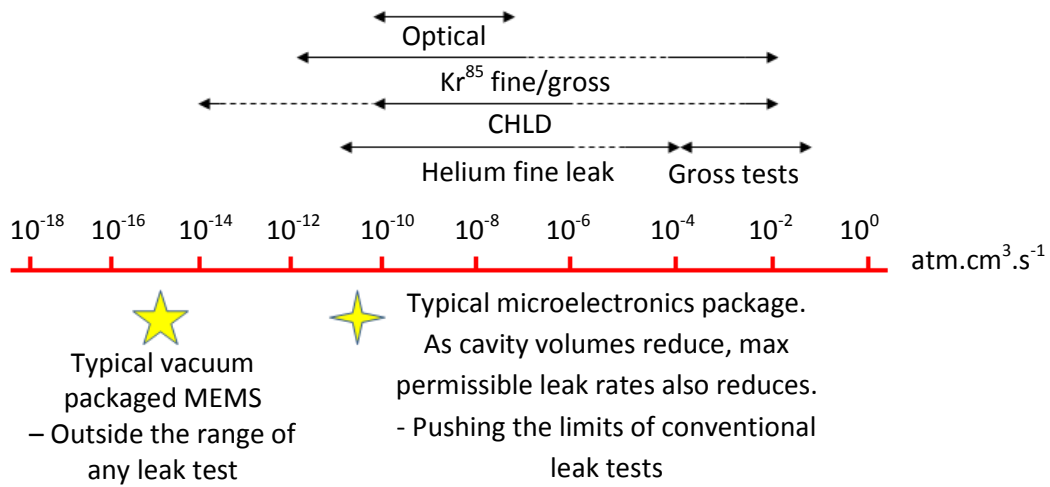
Figure 2.8: Detectable leak range of available test methods and maximum permissible leak rates of typical MEMS and microelectronics packages

2.2   MEMS packaging materials and techniques

As with microelectronics, MEMS packaging can be classified along different levels. Wafer level, which enters the category of level-0 packaging usually involves the capping at the wafer scale of MEMS. This is usually done with a cavity sealing process using anodic bonding, surface fusion bonding or an intermediate layer method [2.10]. There are several advantages to wafer level bonding; all the devices fabricated on the wafer are packaged in one step; the devices are protected during further wafer processing steps including dicing; and, assuming hermetic level-0 packaging, further levels can use cheaper, non-hermetic materials and techniques. An example of level-0 and level-1 packaging is given in figure 2.9.

(a)

(b)
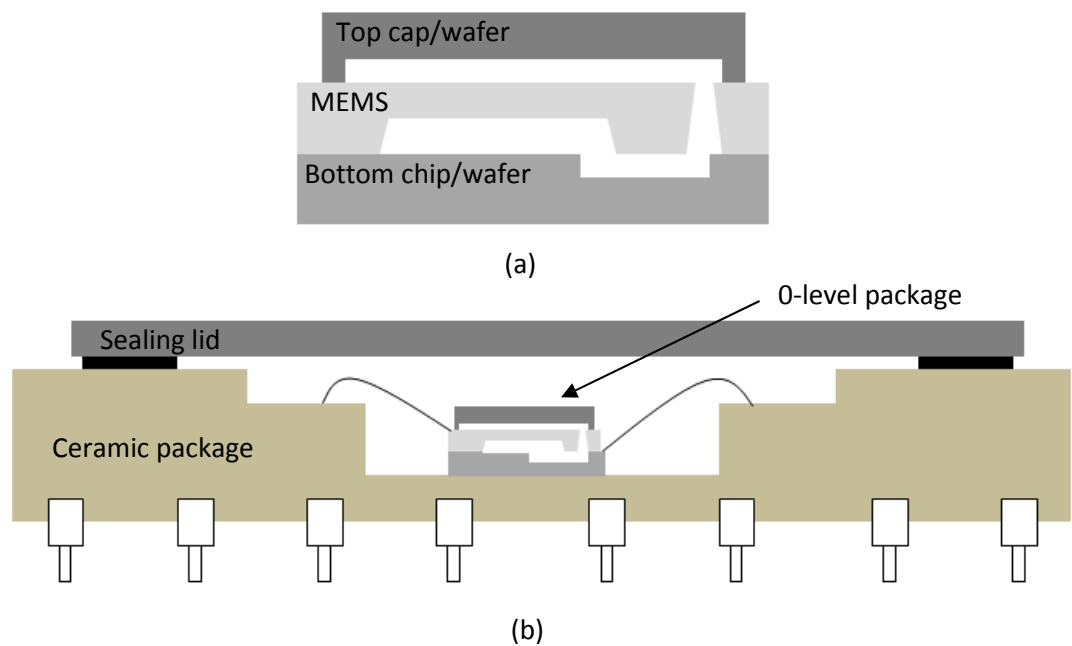
Figure 2.9: An example of (a) level-0 and (b) level-1 MEMS packaging.

Most commercially successful MEMS have used wafer bonding to seal and protect the MEMS in a cavity with controlled ambient conditions. The MEMS chip is then assembled beside the IC controller and signal processor in a standard IC plastic package such as a Dual In-line Package, DIP [2.26, 2.27]. A schematic of this is shown in figure 2.10, in which a MEMS chip and supporting IC are integrated in the same package. This type of packaging is known as a hybrid MEMS package, and has proven to be the most cost effective way of exploiting MEMS technology to date [2.10]. For this type of packaging, it is essential that the MEMS package is hermetic enough to ensure the internal cavity ambient environment is constant throughout the device lifetime. This is especially important when the structure is resonant and requires vacuum packaging for optimum operation.
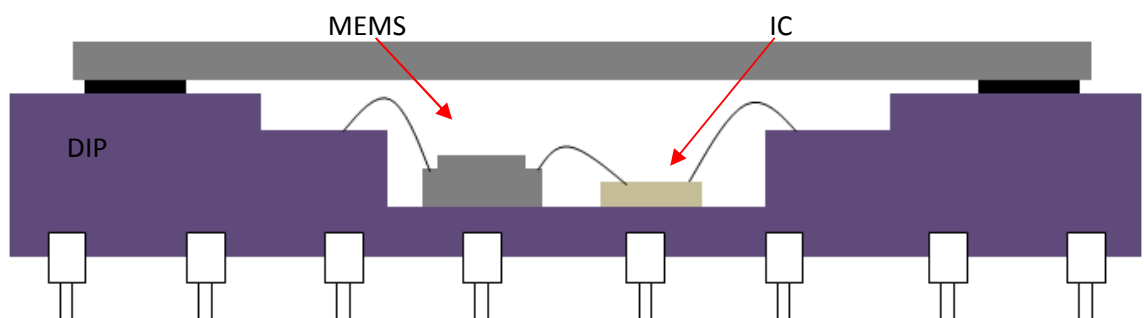
Figure 2.10: Hybrid MEMS

19

Over recent years however, MEMS technology has found several new markets including consumer electronics, data storage and biotechnology [2.26]. These new markets have slightly different packaging priorities compared to traditional markets such as the automotive industry, military and aerospace. Some of the new market sectors prioritise low cost packaging as the lifetime of their product is far shorter than is traditionally required and the output accuracy of the device is less important. For example, in the consumer industry, games consoles and mobile phones are updated almost every year so the end user is unlikely to need or expect the device to function well for more than a few years. They do however expect the cost of these products to be kept as low as possible. Since up to 70% of the cost of a traditionally silicon wafer bonded MEMS is in the packaging, this new demand for low cost, shorter lifetime devices has led manufacturers to look for lower cost, less hermetic packaging techniques [2.10].

In order to fully understand the method of testing hermeticity of MEMS packaging, it is essential to first of all understand the sealing methods themselves. This section describes the various packaging methods available for all MEMS types with a summary showing the most suitable packaging materials and techniques for specific device types and industry sectors with corresponding typical leak rates.

2.2.1   *Materials*

Silicon is the most commonly used substrate for high volume manufacturing and packaging of MEMS due to its well understood electrical properties and its use in the microelectronics industry. Single crystal silicon is one of the best materials for use in sensing applications. It has a yield strength comparable to steel, can be made with almost no defects such that the material is only deformed elastically at room temperature and is not subject to mechanical hysteresis as is the case in metals. Silicon also has a good thermal conductivity, making it an ideal heat sink material. The thermal expansion coefficient of silicon is low and reasonably closely matched to Pyrex, however, the thermal expansion coefficient is temperature dependant [2.10]. From a packaging perspective silicon is an ideal material for use in hermetic packages and its mechanical strength allows sensitive structures to be well protected. Polysilicon by its nature, is less sensitive to fractures caused by microdefects, making such material properties more controllable in a manufacturing environment [2.28].

Ceramics can also be used as a substrate for MEMS fabrication and hermetic packaging. Although it is very difficult and expensive to anisotropically etch structures into ceramics due to their inherent chemical resistance, structures can be cast into silicon molds. Gas phase deposition and chemical vapour deposition can be used to form the structures into molds but the high temperature sintering stage can shrink the structures and reduce accuracy. MEMS made using ceramics like SiC and SiN can be used in harsh environments where they are faced with high temperatures and high pressures [2.10].

When comparing the thermal expansion coefficients, quartz would appear to be a more suitable substrate packaging material as its thermal expansion coefficient is almost temperature independent. As a result, quartz packages tend to have low stress therefore a low likelihood to contain cracks. Quartz can be structured using a variety of techniques including diamond saw cutting, grinding, lapping, polishing, ultrasonic machining and wet and dry chemical etching [2.10]. Ultrasonic machining is best suited to producing small complex shapes and wet etching is preferred for mass manufacturing. Photolithography using gold or chromium masks is also applicable. Micromachined quartz structures have better tolerances than silicon structures and more shapes are possible [2.10]. There is no need for an insulating layer between conductors and the substrate and quartz micro-structures are well suited to high temperature and high shock applications.

Glass is commonly used to package optical MEMS devices or MOEMS as glass gives direct optical access to the device. Hermetic packaging is possible using glass although hydrogen, helium and neon molecules are able to permeate through glass making it less suitable for very high vacuum applications [2.29, 2.30]. These are only present in very small quantities in air so do not pose a problem in most cases.

Polymers are not hermetic packaging materials although polyimides and others offer an interesting low cost, low temperature sealing technique for a new generation of MEMS. Polyimide does however have interesting mechanical properties: it is a flexible substrate, has excellent thermal stability, good dielectric properties, chemical resistance, toughness and does not wear easily. Polyimide has strong carbon ring bonds and so does not melt and flow like most thermosetting and thermoplastic polymers.

21

Photosensitive polyimide is also available making this polymer an ideal negative photoresist for high aspect ratio fabrication since it is transparent. It is also an ideal material for use as a permanent photoresist [2.10]. Polymers are however porous materials and will allow gases to permeate through to the internal cavity. Figure 2.11 shows a graph which indicates the permeation rates of typical packaging materials.
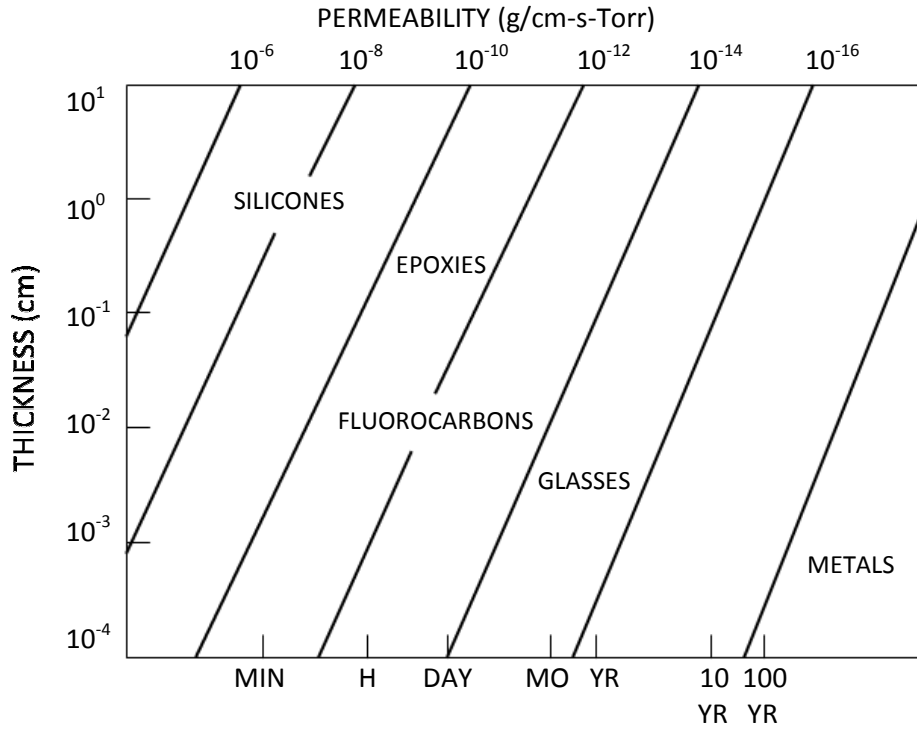
Figure 2.11: Graph of permeation rates though package materials [2.31]

2.2.2 Sealing techniques

Silicon fusion bonding, SFB, sometimes called direct wafer bonding usually involves two silicon wafers although sealing can be performed between silicon and quartz, GaAs and glass. Silicon fusion bonding is simpler, has higher yield and lower cost than most bonding techniques. It is also able to produce die that are 50% smaller in size than anodically bonded die. The wafers are brought into intimate contact at temperatures of 800-1100ºC in an oxidising environment. Bonding occurs between the OH groups present at the surface of native or grown oxides covering the wafers. For successful high strength, void free bonds, the bond should be made at temperatures greater than 1000°C. Wafers should have a surface roughness less than 4 nm and be hydrated to ensure abundant OH groups. Hydration can be achieved by soaking wafers in a H_2O_2-H_2SO_4 mixture, diluted H_2SO_4 or boiling nitric acid. Oxygen plasma can also increase

the numbers of OH groups on the surface of the wafers. The wafers should then be rinsed in deionised water and dried before they are brought together in clean air. Self bonding is initiated when the wafers are in intimate contact and covalent bonds are formed between the two wafer materials during the high temperature annealing process. Although the process is not fully understood, it is thought that the bonding mechanism can be described by the following reaction in which silanol bonds are transformed to siloxane bonds and water [2.10].

$$Si\text{-}OH + OH\text{-}Si \longrightarrow H_2O + Si\text{-}O\text{-}Si$$
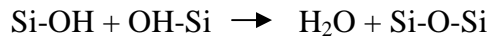
Low temperature direct wafer bonding is currently being investigated although the method still requires to be thoroughly tested to determine the methods bonding strength and hermeticity. For low temperature, 600ºC, direct wafer bonding the wafers require an extremely smooth finish with many preprocessing steps that could potentially increase outgassing during sealing. Polysilicon wafers can also be silicon fusion bonded as commonly used in MEMS wafer level packaging [2.32].

Anodic bonding, also called field assisted thermal bonding, electrostatic bonding or the Mallory process is used to create a hermetic seal between silicon and sodium rich glass such as Pyrex at relatively low temperatures [2.10]. A potential is applied across the two wafers that have been brought into intimate contact. Sodium ions are attracted to the cathode leaving space negative charges on the glass wafer surface. Electrostatic force holds the wafer together and covalent bonds are made during the annealing process at 180-500ºC. A voltage between 200 and 1000V should be applied depending on the thickness of the glass wafer and the temperature used. This process is shown schematically in figure 2.12.
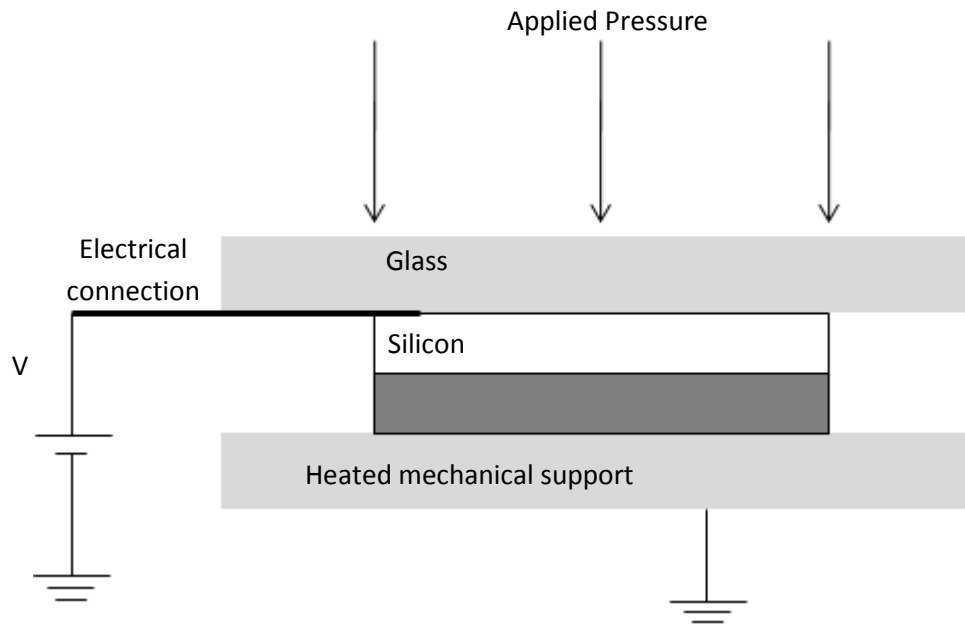
Figure 2.12: Anodic bonding schematic

Bonds can be made in 5 to 10 minutes depending on the process parameters and the bond area. This process requires less stringent surface roughness than is required for silicon fusion bonding and creates less residual stress in the package. For optimum results the wafers should have a surface roughness of less than 1µm, be dust free and have a native oxide less than 200 nm thick. To reduce stress, the temperature of annealing should be set above 315°C. The thermal coefficient of silicon is actually best matched to glass at a lower temperature but experiments have proven that wafer curvature changes from concave (compressive) to convex (tensile) at 315°C due to stresses other than those resulting from a thermal expansion mismatch. As tensile stress is preferred to compressive stress in most cases, temperatures over 315°C are recommended to avoid buckling of silicon structures [2.10].

Anodic bonding can also be used to seal GaAs wafers to glass wafers at 360°C, 800V for 30 minutes. For optimum bonding results, the GaAs wafer should be prebaked at 400°C for 15 minutes in an N_2 and H_2 atmosphere to remove oxides before bonding. To decrease the annealing time from an hour to 5 minutes at 400°C and 600V, a metal mesh is used to deliver the electric field evenly over the glass wafer. Silicon dioxide and aluminium layers can be used to protect the silicon substrate from high electric

fields experienced during anodic bonding. This creates a good hermetic bond although the aluminium will creep over time leading to drift in sensor output. To minimise this effect, polysilicon can used instead of aluminium. It is also possible to anodically bond two silicon wafers by sputtering or evaporating a thin layer, 4 – 7 µm, of borosilicate glass on one wafer [2.10].

Intermediate layers of glass frit, solder or eutectic can be used to create hermetically sealed packages. Low pressure chemical vapour deposition (LPCVD) of phosphosilicate glass, PSG, can seal two silicon wafers at 1100°C in 30 minutes. Glass frit can be deposited by spraying, screen printing, extrusion or sedimentation to wafers and pre-glazed to remove organic residues. The wafers are then brought into intimate contact and heated to 415 - 650°C until glass reflows under 6.805×10^{-2} atm (1 psi) of pressure. Devitrifying glasses provide a thermosetting seal whereby the glass crystallises during sealing and the mechanical properties of the glass are changed. Low melting point vitreous glass is also available and provides a thermoplastic seal which melts and flows during sealing but does not experience any change in mechanical properties. Glass frit bonding offers a hermetic seal but the mechanical and chemical behaviour of the material is yet to be thoroughly studied [2.10].

A wide range of low melting temperature alloys can be used as an intermediate layer to provide a hermetic seal. Eutectic alloys are deposited on one wafer and the wafers are brought together and heated above the eutectic temperature. Gold-silicon eutectic bonding is often used as silicon is a common substrate material and gold is often used as a thin-film material during MEMS fabrication. A gold-silicon eutectic bond can be made at 363°C with a fracture strength of 148 MPa, which compares well with a typical silicon fusion bond fracture strength of 5 – 15 MPa [2.10]. Low temperature intermediate bonding techniques are also being developed, whereby glass frit or eutectics can be heated to the required bonding temperature directly by lasers [2.33]. This type of bonding helps to reduce the temperature in the centre of the package where the sensitive MEMS structures are fabricated, whilst still producing a good quality hermetic seal [2.33].

Polymers can be used to seal wafers at low temperatures and pressures. Photoresist materials such as AZ-4000, SU-8 and PMMA can be used to photopattern seal rings around die features for level-0 device protection [2.10]. They typically form low

temperature, high strength bonds with low stress due to the elastic properties of the polymers [2.34]. However, polymer seals have high vapour pressure, poor mechanical properties and are not hermetic [2.34]. The new market interest in low cost packaging has led to a marked increase in research into alternative seal materials. Polymers such as Benzo-Cyclo-Butene, BCB, and Liquid Crystal Polymer, LCP, used as intermediate bonding materials offer very low moisture permeation rates providing protection from corrosion for a period of months to years depending on the seal thickness [2.35, 2.36, 2.37]. Packages using this type of seal are now known as 'near-hermetic' or 'quasi-hermetic' packages [2.38, 2.39, 2.40, 2.41]. Parylene has also been suggested as a material that can be used to coat non-hermetic package to lower moisture permeation rates [2.42].

2.2.3   Summary of MEMS packaging materials and techniques

With the wide variety of MEMS available and the number of different industry sectors in which they are used, it is important to understand which packaging materials and techniques are best suited to each application. In order to determine the level of protection that the package must provide, both in terms of hermeticity and mechanical protection, the expected lifetime and operating conditions must be known. The temperature range that the device will go through is of particular interest so as to avoid the dew point and hence the condensation of water vapour within the package.

The maximum tolerable leak rate will depend on whether the package has been vacuum packaged, the volume of the package cavity, the expected lifetime of the device and the sensitivity of the internal structure to changing ambient pressure and contaminants. Table 2.1 shows a summary of typical package leak rates in each industrial sector. Military, space, aviation and telecoms have the longest expected lifetimes in excess of ten years. The package required must be as hermetic as possible to protect the device from contamination and the most hermetic package materials and bonding techniques are necessary. The automotive industry has similar needs but due to cost pressures and lower expected lifetime, some device types can afford slightly less hermetic packaging. Glass caps, glass frit materials and other intermediate bonding techniques can therefore also be used in industrial applications. Biotechnology is one of the most challenging industry sectors with regards to packaging. Depending on the type of product, the lifetime requirements can vary significantly. For example, implantable devices will

require the longest lifetime possible to ensure the device can be left safety inside the body for a number of years. Conversely, disposable point-of-care test devices have a lifetime requirement of only one use but sometimes can have a shelf life of many years. Generally, biocompatible materials are required for packaging, excluding thereby silicon and most metals. The most significant packaging requirement is to isolate biological and chemical specimens in the package. The package need not be impermeable to gases but must protect from or contain biological fluids and chemicals. For this reason the leak rate requirements of the package can differ significantly from those of the other industry sectors. This will be discussed more thoroughly in section 2.4 of this chapter when permeation rates are discussed. The consumer sector requires hermetic packages at the lowest cost as the end user is unlikely to expect lifetimes greater than a few years. Cheaper packaging materials such as adhesives and polymers can then be used in packaging.

Industry Sector	Lifetime (years)	Temperature Range (°C)	Permissible Leak Rate (atm.cm^3.s^{-1})	Package and seal materials	Bonding methods
Military Space Aviation	>10	-55 to 150	10^{-13} to 10^{-16}	Metals/Si Ceramics	SFB Anodic
Telecoms	>10	-20 to 65	10^{-13} to 10^{-16}	Metals/Si Ceramics	SFB Anodic
Automotive	5 – 10	-40 to 125	10^{-10} to 10^{-16}	Metal/Si Ceramics Glass	SFB Anodic Glass Frit Eutectic/Solder
Industrial	2-5	-20 to 65	10^{-10} to 10^{-16}	Metals/Si Ceramics Glass	SFB Anodic Glass Frit Eutectic/Solder
Biotechnology	From single use to 10 (subject to application)	Often around body temperature – isolation of biological and chemical samples more relevant in this industry sector	10^{-6} to 10^{-16}	Glass Polymers	Polymer Adhesive
Consumer	~ 2	0 to 50	10^{-6} to 10^{-16}	Metals/Si Ceramics Glass Polymers	SFB Anodic Glass Frit Eutectic/Solder Polymer Adhesive

Table 2.1: Summary of MEMS packaging by industry sector.

2.3 Traditional hermeticity test methods

In this section, the various hermeticity test methods listed in military standards MIL-STD-883H T.M.1014.13 and MIL-STD-750E T.M.1071.8 are described in detail. The first two test methods discussed are the helium fine leak test and the radioisotope fine leaks test. These are the most commonly used hermeticity test methods but both require to be used in conjunction with a gross leak test to cover the full range of possible leak rates. There are many gross test methods described in the military standards and these will be described in section 2.3.3 to 2.3.6. The final two test methods described are tests which combine fine and gross leak detection and have been recently added to the military standards.

2.3.1 Helium fine leak test

The helium fine leak test is described in both military standards but tighter reject limits are placed on packages in MIL-STD-750E T.M.1071.8. Helium fine leak detection relies on a helium mass spectrometer to measure the amount of helium leaking out of the package being tested [2.22, 2.23, 2.43, 2.44].

Before the helium fine leak test can be done, the device to be tested should be either packaged in helium or the packaged device should be pressurised, 'bombed', in helium for a length of time and at a pressure dictated by the standards and dependent on the cavity volume of the package. After this pressurisation step, the package should be removed from the 'bombing' chamber and transferred to helium leak detector chamber within a certain time. This time is known as *the dwell time* and should be kept under an hour to ensure the helium which has been forced into the test package does not leak out before the test can be conducted. When the helium leak detector, shown schematically in figure 2.13, is started, the chamber in which the test package is located is pumped down, this is known as *the initialisation time* [2.45]. Valve V3, shown in figure 2.13, is then opened and the gas leaking from the package is directed to an ionisation chamber which is initially under vacuum [2.22, 2.23].
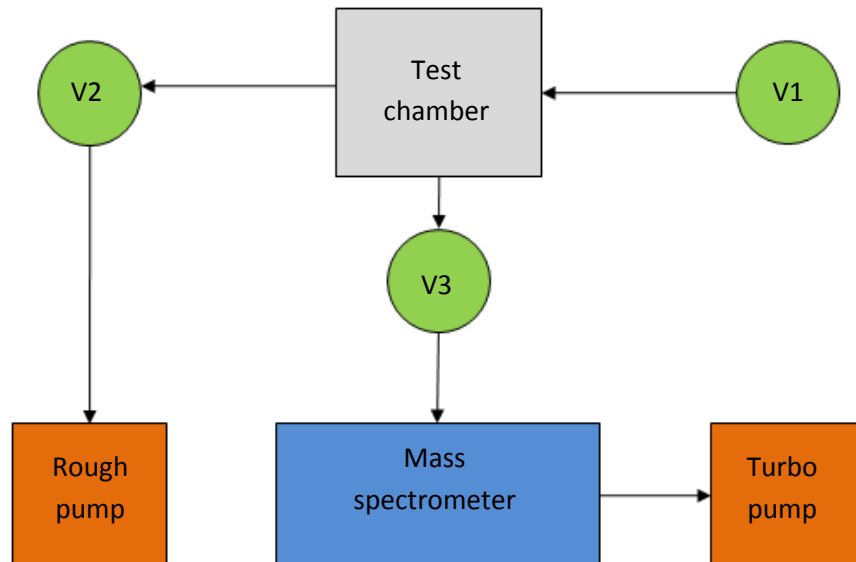
Figure 2.13: Schematic of the helium leak detector [2.25]

The gas molecules leaking from the test package collide with a stream of electrons produced by a hot filament to create ions quantitatively proportional to the pressure of gas in the ionisation chamber.   The ions are repelled out through an exit slit and enter a magnetic field in a straight ribbon. All helium ions are deflected, through Lorentz's law, along a certain path by the magnetic field as shown in figure 2.14.   These ions are collected and the current produced by this ion flow is used to drive an amperemetre. The recorded current is proportional to the pressure of helium entering the mass spectrometer and a helium leak rate of the package is determined.   This leak rate is called *the measured leak rate*.   The helium leak test process is depicted in figure 2.15 [2.22, 2.23].
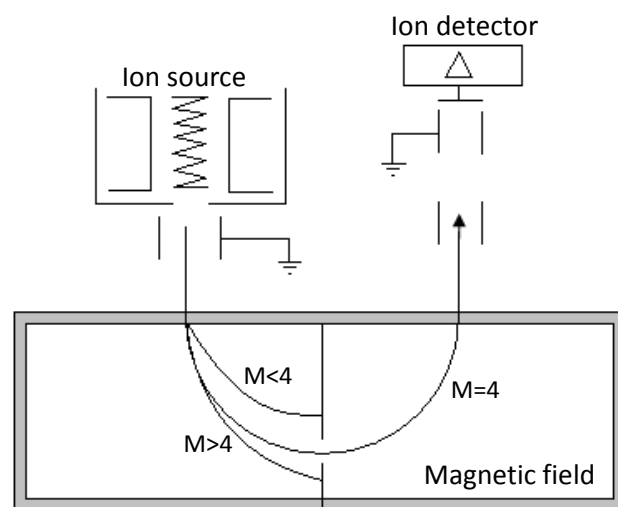
Figure 2.14: Deflection of helium ions under magnetic field.

M is the molecular weight of the molecule expressed in grams.
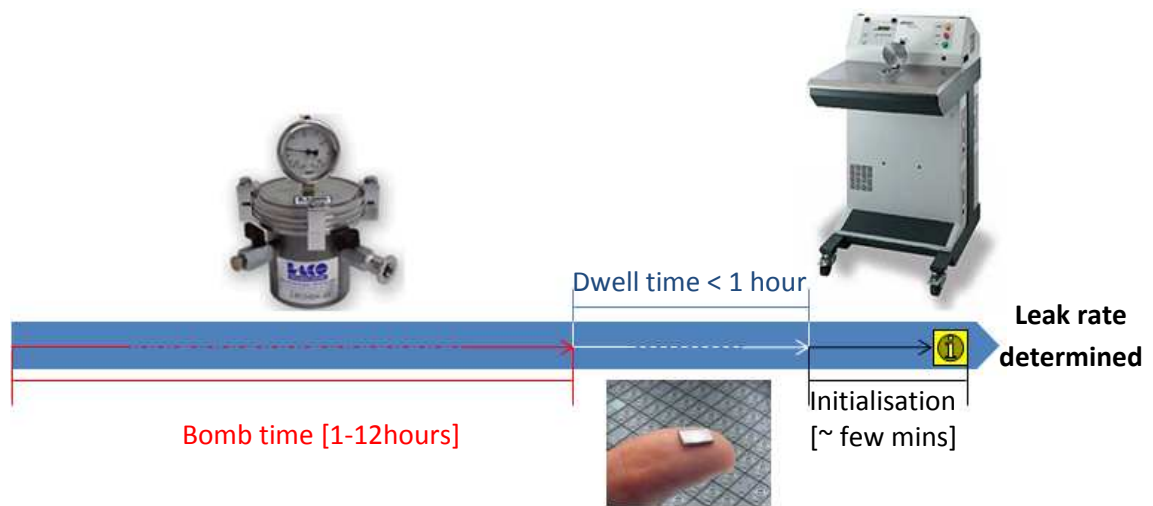
Figure 2.15: Timeline for the helium fine leak test method

The measured helium leak rate is the helium leak rate of the package under the specific test conditions employed. Before the leak rate of packages can be compared, the measured leak rate should be converted to *an equivalent standard leak rate* as described in section 2.1.3. The equivalent standard leak rate is the measured air leak rate when the high pressure side is 1 atm and the low pressure side is 1 mmHg (1.3158×10^{-3} atm). The *reject leak rate* of a package can be calculated in one of two ways: by using a look-up table or by using the Howl-Mann equation given in the standards. Table 2.2 shows the test parameter and reject rates from MIL-STD-883H T.M.1014.13 and table 2.3 shows the tighter reject limits of MIL-STD-750E T.M.1071.8. The reject limits that MIL-STD-883H T.M.1014.13 and MIL-STD-750E T.M.1071.8 place on packages tested using the Howl-Mann equation, equation 2.1, are shown in table 2.4. The experimental parameters given must be precisely followed when using the conversion table. For this reason, the Howl-Mann equation, equation 2.1, is the preferred method. This equation gives the user a reject helium leak rate for the package considered and the test parameters employed from a standard leak rate that the package cavity volume should not exceed. Both military standards state that the package to be tested should be exposed to a minimum pressure of 2 atmospheres [2.22, 2.23].

Volume of package (V) in cm³	Bombing conditions			Reject limit (R₁) atm.cm³.s⁻¹ He.
	Pressure (psia) +/- 2	Min. exposure time (t₁) hours	Max. dwell time (t₂) hours	
<0.05	75	2	1	5×10^{-8}
≥0.05 - <0.5	75	4	1	5×10^{-8}
≥0.5 - <1.0	45	2	1	1×10^{-7}
≥1.0 - <10.0	45	5	1	5×10^{-8}
≥10.0 - <20.0	45	10	1	5×10^{-8}

Table 2.2: Helium fine leak test parameters and reject limits from MIL-STD-883H T.M. 1014.13 [2.22]

Volume of package (V) in cm³	Bombing conditions			Reject limit (R₁) atm.cm³.s⁻¹ He.
	Pressure (psia) +/- 2	Min. exposure time (t₁) hours	Max. dwell time (t₂) hours	
< 0.01	75	2	1	5×10^{-9}
> 0.01 ≤ 0.05	75	3	1	1×10^{-8}
> 0.05 ≤ 0.5	75	4	1	1×10^{-8}
> 0.5 ≤ 1.0	75	2	1	1×10^{-8}
> 1.0 ≤ 10.0	60	5	1	5×10^{-8}
> 01.0 ≤ 20.0	45	10	1	5×10^{-8}

Table 2.3: Helium fine leak test parameters and reject limits from MIL-STD-750E T.M. 1071.8 [2.23]

The Howl-Mann equation reads:

$$R_1 = \frac{LP_E}{P_0}\left(\frac{M_A}{M}\right)^{1/2}\left\{1 - e^{-\left[\frac{Lt_1}{VP_0}\left(\frac{M_A}{M}\right)^{1/2}\right]}\right\}e^{-\left[\frac{Lt_2}{VP_0}\left(\frac{M_A}{M}\right)^{1/2}\right]}$$

(2.1)

where R_1 is the measured leak rate in atm.cm³.s⁻¹ helium, L is the equivalent standard leak rate in atm.cm³.s⁻¹ air, P_E is the bomb pressure in atm, P_0 is the atmospheric pressure in atm, M_A is the molecular weight of air in grams (28.7g), M is the molecular weight of helium in grams (4g), t_1 is the bomb time in seconds, V is the package cavity volume in cm³ and t_2 is the dwell time in seconds [2.22, 2.23].

MIL-STD-883H		MIL-STD-750E	
Volume (cm^3)	Reject equivalent standard leak rate (atm.cm^3.s^{-1})	Volume (cm^3)	Reject equivalent standard leak rate (atm.cm^3.s^{-1})
< 0.01	1×10^{-9}	< 0.01	5×10^{-8}
> 0.01 ≤ 0.5	5×10^{-9}	> 0.01 ≤ 0.4	1×10^{-7}
> 0.5	1×10^{-8}	> 0.4	1×10^{-6}

Table 2.4: Failure criteria for flexible method stated in both military standards [2.22, 2.23]

Many package manufacturers use the helium leak test to measure the leak rate of batches of packages. Should the leak rate of the batch exceed the expected leak rate, the packages are tested individually to find the leaking packages. Other users choose to 'bomb' packages in batches and test them individually in the helium leak detector, taking care to ensure the last package is tested before the dwell time exceeds one hour [2.22, 2.23].

Other ways of using the helium leak test include the through-hole leak detection method is which the package containing a hole through its base is attached directly to the helium leak detector [2.22, 2.23, 2.43, 2.44, 2.48]. Once the detector is ready for use and the test package is securely attached to the leak detector using o-rings, the package is either sprayed with helium as shown in figure 2.16 or exposed to a global helium test whereby the package is surrounded in a tent of helium [2.22, 2.23]. Before this test method can be used the leak rate of the o-ring must be established by fixing a piece of packaging material containing no holes with o-rings to the helium leak detector. This will form the background helium leak rate which should be deducted from the leak rate of the package being tested. For this reason, through-hole testing has a higher minimum helium leak rate, usually around 10^{-9} atm.cm^3.s^{-1}. This type of testing is destructive, but the spray method can be useful to locate leaks [2.22, 2.23].
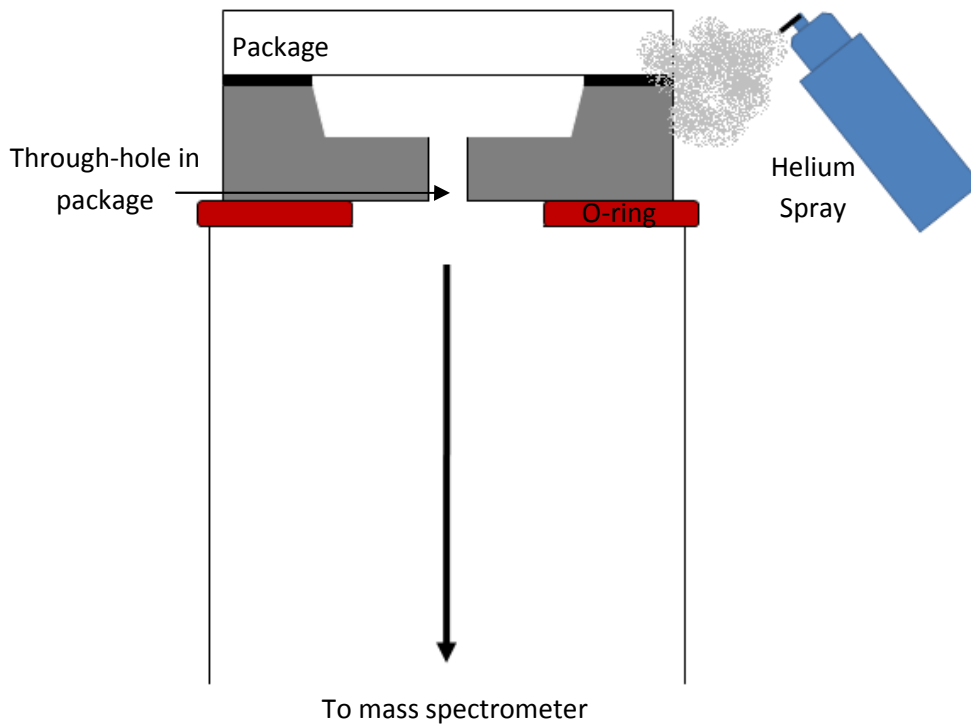
Figure 2.16: Through-hole helium leak detection method

The sensitivity or minimum detectable leak rate of this method is dependent on the sensitivity of the mass spectrometer used which is, in turn, dependent on the level of vacuum achievable in the system. Today, most commercially available leak detectors are able to measure leak rates down to 10^{-11} atm.cm^3.s^{-1}. With this test method it is possible to achieve erroneous results due to virtual leaks coming from the slow release of trapped helium in the interior of the chamber. It is also possible that gross leaks are missed due to helium leaking out of the package during the dwell time, hence the need to use this fine leak test in conjunction with a gross leak test. Generally, the fine leak test is carried out first since the gross leak test can be destructive or liquids used can temporarily clog fine leak channels making the fine leak test invalid [2.22, 2.23].

2.3.2 *Radioisotope leak detection*

The radioisotope method of leak detection can be done in combination with a radioisotope gross leak test which is recommended for time saving reasons but not suitable for every package type [2.18]. The combinational test is discussed first

followed by individual versions of the fine leak test. Both the wet and dry versions of the radioisotope gross leak tests will be described. All the methods should be conducted using a gas handling system to minimise the operators contact with the radioisotope, Kr^{85}, present in the tracer gas mixture [2.22, 2.23, 2.44].

The radioisotope gross/fine combination test requires that the packages to be tested are placed in a pressurisation chamber which may be filled with inert material to reduce cycle time and make the test more efficient. The chamber is firstly evacuated to 6.579×10^{-4} atm (0.5 torr) and then filled with a mixture of Kr^{85} and air at at least 3 atm (45 psi), for a minimum duration of 12 minutes. The concentration of Kr^{85} in the Kr^{85}/air gas mixture should be no less that 100 µCi/cm³. The actual pressure and soak time can be determined by equation 2.2 [2.22, 2.23].

$$ Q_s = \frac{R}{skTPt} \tag{2.2} $$

where Q_s is the maximum leak rate allowable, given in the military standards and presented in table 2.5, s is the specific activity of the Kr^{85} tracer gas in micro Curies (µCi), T is the soak time in hours and t is the conversion from hours to seconds (3600). R is the reject count rate and should not be less than 500 counts/min. This can also be described as the count rate above the ambient background if the package were to have a leak rate Q_s after pressurisation. P is the difference between the square of the bomb pressure and the square of the original pressure of the package to be tested. The bombing pressure and soak time should be adjusted to suit equation 2.2 and the requirements of the test stated above [2.22, 2.23].

MIL-STD-883H T.M. 1014.13		MIL-STD-750E T.M. 1071.8	
Volume of package (cm³)	Q_s (atm.cm³.s⁻¹)	Volume of package (cm³)	Q_s (atm.cm³.s⁻¹)
<0.01	1×10^{-8}	<0.05	5×10^{-9}
>0.01, ≤0.4	5×10^{-8}	>0.05, <0.5	1×10^{-8}
>0.4	5×10^{-7}	>0.5, <20.0	5×10^{-8}

Table 2.5: Test limits for radioisotope fine leak test from MIL-STD-883H T.M. 1014.13 and MIL-STD-750E T.M. 1071.8 [2.22, 2.23]

After pressurisation for the required soak time, the tracer gas should be returned to storage within 3 minutes to leave a pressure of 2.632×10^{-3} atm (2 torr) in the

pressurisation chamber. The tank should then be back filled with air and the packages moved and measured at the counting station within 10 minutes. The actual leak rate of the package in atm.cm^3.s^{-1} Kr, Q, can be calculated using equation 2.3 where $Q_{c/m}$ is the actual leak rate in counts per minute, Q_s and R are as previously defined [2.22, 2.23].

$$Q = \frac{Q_{c/m} * Q_s}{R} \qquad (2.3)$$

Due to surface sorption issues, the combinational gross/fine radioisotope test cannot always be performed. During the bombing process, the tracer gas is absorbed in some packaging materials. In such a situation, the package requires a 'wait time' during which the absorbed tracer gas is released from the package and the leak rate can be assessed. Due to the short test time necessary for effective combinational testing, the test is not compatible with these types of packages. To determine whether the package to be tested requires a 'wait time', a sample package should be bombed according to the test procedure and the count rate measured every 10 minutes. When the count rate becomes asymptotic with time, surface sorption is no longer a problem and this time should be noted as the 'wait time' [2.22, 2.23].

The pressurisation procedure described above for the combinational test should be followed for the radioisotope fine leak test with the exception that the tracer gas mixture should be Kr^{85}/N$_2$ with a concentration of Kr^{85} in dry nitrogen of no less than 100μCi/cm^3. Removal of the tracer gas to storage after pressurisation should occur until 6.579×10^{-4} atm (0.5 torr) pressure exists in the chamber. This storage step should again be complete within 3 minutes and the chamber backfilled with air. The packages should then be transferred and measured by a scintillation crystal equipped counting station within 30 minutes. Package types that require a wait time should not be measured until after the 'wait time' has elapsed and should be tested within an hour. The failure criteria for the fine leak test are the same as those of the combinational test shown in table 2.5 [2.22, 2.23].

After the radioisotope fine leak test, the packages must be subjected to a gross leak test. There are two type of radioisotope gross tests; wet and dry. The dry radioisotope gross test can only be conducted on packages containing some Kr^{85} absorbing or adsorbing materials or on packages with an internal free volume of 0.02cm^3 or more. The dry

radioisotope gross test involves pressurising the packages to be tested in Kr^{85}/air tracer gas for 2 minutes at 3 atm (45 psi) after first evacuating the chamber to 6.579×10^{-4} atm (0.5 torr). The tracer gas should be removed to storage within 2 minutes until 2.632×10^{-3} atm (2 torr) of pressure remains in the chamber before the chamber is backfilled with air. The packages should then be removed, transferred and measured at the counting station within 10 minutes. Any package displaying a count rate above 1000 counts/minute is considered to have a gross leak [2.22, 2.23].

Before a slightly modified version of the dry radioisotope gross leak test is performed, the wet radioisotope gross leak test requires that the packages are immersed in hydrocarbon vacuum pump oil and evacuated to at least 1.316×10^{-2} atm (10 torr) for 10 minutes then pressurised with air for an hour at, at least 3 atm (45 psi). The packages should then be removed from the oil and cleaned before being placed in the radioisotope pressurisation. The chamber should be evacuated to 6.579×10^{-4} atm (0.5 torr) then pressurised in Kr^{85}/air tracer gas at a minimum of 3 atm for at least 12 minutes. The tracer gas should be returned to storage within 2 minutes until 2.632×10^{-3} atm (2 torr) pressure exists in the chamber. After backfilling the chamber with air, the packages should be removed, transferred and measured at the counting station within 10 minutes. A count rate above 1000 counts/minute indicates the package concerned has a gross leak [2.22, 2.23].

2.3.3 *Fluorocarbon liquid and vapour gross leak detection*

The preparation procedures of both the liquid and vapour gross leak detection methods are as follows. Packages with internal free volume below 0.1 cm^3 should be placed in a pressure/vacuum chamber and the pressure should be reduced to at least 6.579×10^{-3} atm (5 torr) for 30 minutes. Before the vacuum is released, the packages should be covered in detector fluid of type I (see table 2.6). The packages should then be pressurised according to table 2.7. The packages should be removed from the pressurisation chamber after the pressurisation period and transferred to a holding bath of detector fluid within 20 seconds. The packages should be dried for 2 +/- 1 minutes in air before being transferred for liquid or vapour detection [2.22, 2.23, 2.44].

Property	Type I	Type II	Type III
Boiling point (°C)	50-95	140-200	50-110
Surface tension at +25°C (dynes/cm)		<20	
Density at +25°C (g/ml)	>1.6	>1.6	>1.6
Density at +125°C (g/ml)		>1.5	
Dielectric strength (V/ml)	>300	>300	>300
Residue (Tg/g)	<50	<50	<50
Appearance	Clear, colourless		

Table 2.6: Military standard physical property requirements of perfluorocarbon fluids for gross leak detection [2.22, 2.23]

Pressure psia (minimum)	Minimum pressurisation time (hours)	
	Liquid test	Vapour test
30	23.5	12
45	8	4
60	4	2
75	2	1
90	1	0.5
105	0.5	N/A

Table 2.7: Liquid and vapour fluorocarbon gross test pressurisation conditions [2.22, 2.23]

After pressurisation and drying, the packages should be transferred to and immersed in a bath of type II detector fluid which is maintained at 125+/- 5°C for liquid fluorocarbon gross leak detection. The package should be illuminated and observed through a magnifier for at least 30 seconds against a dull, non-reflective, black background. If two or more bubbles from the same point or a stream of bubbles are observed as in figure 2.17, the package is deemed to have a gross leak [2.22, 2.23].
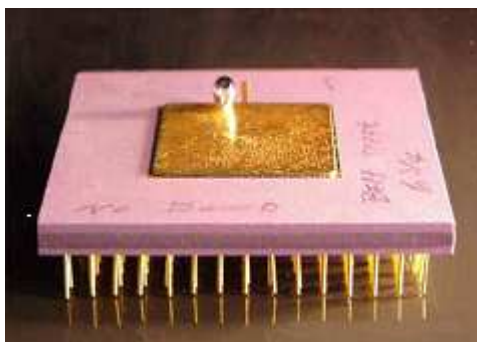
Figure 2.17: Bubbles escaping from a gross leaker [2.49]

In the case of vapour gross leak detection, the packages should be transferred to a fluorocarbon vapour detection system after pressurisation and drying. The system should be kept at a temperature of 125 +/- 5 °C, the 'purge' time should be in accordance with table 2.8 and the test time should be at least 3.5 seconds. The 'purge' time is the time that the package is heated prior to testing. The test time can be reduced to 2.5 seconds if the test chambers are heated to 150 +/- 5 °C. A package is considered to have a gross leak when the detector indicates more than 0.28 mg of type I detector fluid [2.22, 2.23].

Package internal free volume (cm^3)	Purge time at 125 +/- 5 °C (seconds)
≤ 0.01	≤ 5
$\geq 0.01 \leq 0.10$	≤ 9
≥ 0.1	≤ 13

Table 2.8: Fluorocarbon vapour gross leak detection purge time from military standards [2.22, 2.23]

2.3.4 Gross Bubble Test

This test is listed in MIL-STD-750E T.M.1071.8 and should only be applied to a package with an internal free volume greater than 1 cm^3. The test requires immersing the packages in a fluid maintained at 125 +/- 5 °C for at least 1 minute. During the immersion the package should be observed against a black non-reflective surface whilst being illuminated. A package showing a stream of bubbles, two or more bubbles coming from the same point or one or more attached growing bubbles is considered to have a gross leak [2.22, 2.23].

2.3.5 Weight gain - gross leak detection

The packages to be tested should first be cleaned in a solvent at +25°C according to MIL-STD-750E T.M.1071.8. MIL-STD-883H T.M.1014.13 omits this step. Both standards then state that the packages should be baked in an oven at +125 +/- 5 °C for at least an hour and then cooled at room temperature. The weight of each package should be recorded. Packages with an internal free volume less than 0.1 cm^3 should be placed in a pressure/vacuum chamber where the pressure should be reduced to at least 6.579×10^{-3} atm (5 torr) for a minimum of an hour. The packages should then be covered in type III fluid, properties listed in table 2.6, before the vacuum is broken and pressurised to 5.103 atm (75 psia) for 2 hours or 3 atm (45 psia) for 10 hours. Packages with volumes greater than 0.1 cm^3 that did not require the initial vacuum stage should be pressurised at 6.124 atm (90 psia) for at least 2 hours. After release the packages should be transferred to a bath of fluid before being air dried for 2 +/- 1 minutes and individually weighed within 4 minutes of removal from the bath. If the weight of the package has increased by more than 1 mg for packages with an internal free volume less than or equal to 0.01 cm^3 or 2 mg for packages with an internal free volume greater than 0.01 cm^3 should be rejected. A cell categorisation method is explained in the standard for batch testing purposes [2.22, 2.23].

2.3.6 Dye penetrant gross leak test

This gross leak test requires the tested packages to be placed in a pressurisation chamber which should be filled with a dye solution. The chamber is then pressurised to 7.145 atm (105 psia) for 3 hours or 4.083 atm (60 psia) for 10 hours before being removed and washed in a suitable solvent. After air-jet drying the package should be examined using a magnifier and UV source if required. All non-transparent packages will require delidding to allow observation of dye penetration into the package. For this reason, this gross leak test is destructive and usually only used to verify a leak and determine the leak path [2.22, 2.23].

2.3.7 Optical fine/gross leak detection method

The optical fine and gross leak test method may be conducted separately but, as the test methods are so compatible, they are generally performed together to cover as much of

the leak range as possible. The packages to be tested should be sealed in the test chamber and an optical interferometer set to observe the deflection of the package lids. The test chamber is then evacuated and the deflection of the lid is monitored as the external pressure is reduced. The test chamber pressure should be held at a constant vacuum while any deflection of the package lid is observed by the optical interferometer for a test time t_1. The chamber should then be pressurised up to 2 atm of helium gas and held at a constant pressure for a test time t_2. Any package lid deflection should again be monitored by the optical interferometer. Deflection of the lid is dependent on the material properties of the lid material, the thickness and the lid geometry. For this reason, MIL-STD-750E T.M.1071.8, states that this test should not be performed on packages with a lid thickness above 0.025 inches. Table 2.9 shows the lid specification for use of this test set by the military standards [2.22, 2.23, 2.44, 2.50, 2.51].

MIL-STD-883H T.M.1014.13	MIL-STD-750E T.M.1071.8
$\dfrac{R^4}{ET^3} > 3.0 \times 10^{-4}$	$\dfrac{R^4}{ET^3} > 1.0 \times 10^{-3}$
Where, R is the minimum width of the free seal in inches, E is the modulus of elasticity of the lid material in psi and T is the lid thickness in inches.	

Table 2.9: Military standard lid specifications for optical leak detection [2.22, 2.23]

The optical leak detection method's sensitivity is improved as the test chamber pressure is increased during the helium pressurisation stage and as the test time is increased. Both military standards provide equations to determine the leak rate sensitivity of the method as a function of the lid material properties and geometry, the volume of the package cavities, the test time, the test pressure and the measured deflection [2.22, 2.23].

The tested package is considered to have a gross leak if no lid deflection is measured as the test chamber pressure is changed. The package also fails the test if lid deflection is measured when the test chamber pressure is kept at a constant vacuum or at constant helium pressure [2.22, 2.23].

2.3.8 Cumulative helium leak detection (CHLD) method

Cumulative helium leak detection (CHLD) has recently been added to both military standards as an option for fine and gross helium leak detection. MIL-STD-883H T.M.1014.13 also states that this test can be used with other inert tracer gases so long as the mass spectrometer is able to detect the gas concerned. Figure 2.18 shows a schematic of the cumulative helium leak detector for comparison with the standard version in figure 2.13.
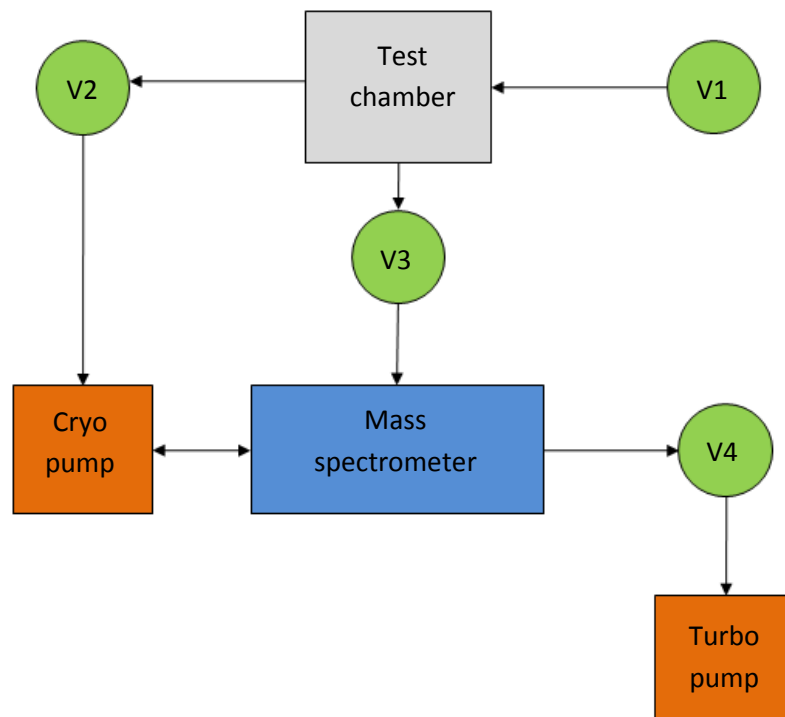
Figure 2.18 Schematic of cumulative helium leak detector [2.25]

The main difference between the two set-ups is the use of the cryo-pump to replace the rough pump and the link between this pump and the mass spectrometer. The cryo-pump is designed to pump out of the test chamber all gases except helium. As the cryo-pump is connected to the mass spectrometer, a sharp peak in the helium signal indicates a gross leak. It is the volume of helium, above background, initially leaking out of the package that indicates a gross leak. A fine leak rate is calculated using CHLD by comparing the rate of change of the helium signal to that of a helium standard leak. Before the test begins, the bombing procedure is identical to the traditional helium leak test method explained in section 2.3.1. To ensure that gross leaks are measured accurately, the dwell time should however be kept to a minimum whilst allowing

enough time for the helium to be absorbed on the package surface prior to release. For optimum test sensitivity, the volume of the chamber should be kept to a practical minimum. The failure criteria of the CHLD test method given in each standard is equivalent to that of the corresponding helium fine leak test [2.22, 2.23, 2.25].

MIL-STD-883H T.M.1014.13 states that the minimum detectable leak rate of the CHLD test method is less than $1x10^{-10}$ atm.cm^3.s^{-1} [2.22]. MIL-STD-750E T.M. 1071.8 states that the minimum detectable leak rate is $3x10^{-13}$ atm.cm^3.s^{-1} [2.23] and the designers of this test method, Pernicka, claim a minimum detectable leak rate of $4x10^{-14}$ atm.cm^3.s^{-1} [2.25]. It is however stated in both standards and in literature from Pernicka that the design of the apparatus can increase or decrease this limit. The variation in the achievable minimum detectable leak rate of this method has sparked controversy in the industry, particularly since the lowest known helium standard leak available has a leak rate of around $5x10^{-10}$ atm.cm^3.s^{-1}. Many users and industry professionals are currently debating whether detection of a leak up to 4 orders of magnitude lower than the standards against which it is measured is accurate, if indeed possible [2.22, 2.23].

2.4 Leak types

The key to finding the most effective way to measure leak rates of packages with small cavity volumes is to understand the types of leak present in such packages. Traditional leak test methods assume the existence of a leak channel present in the package wall or seal which extends from the outside surface of the package to the internal cavity. The mathematical description of the flow mechanisms of gas through leak channels will be explained in section 2.4.1. Near hermetic packaging using polymers has introduced another type of leak caused by permeation. The flow mechanism of a permeation leak is vastly different to that of capillary leak and will be described in section 2.4.2. Permeable packaging materials cannot be used for vacuum packaging and so moisture permeation is the focus of concern for these package types. In contrast, some small cavity devices require packaging capable of maintaining an ultra high vacuum environment for over 20 years. This type of package must use the most hermetic materials and sealing techniques. Once the hermetic sealing technique has been optimised, the leak type likely to be of concern in this type of package is outgassing, either during high temperature packaging or throughout the device lifetime.

Outgassing will be described in section 2.4.3. Figure 2.19 depicts the three leak types described in this section.
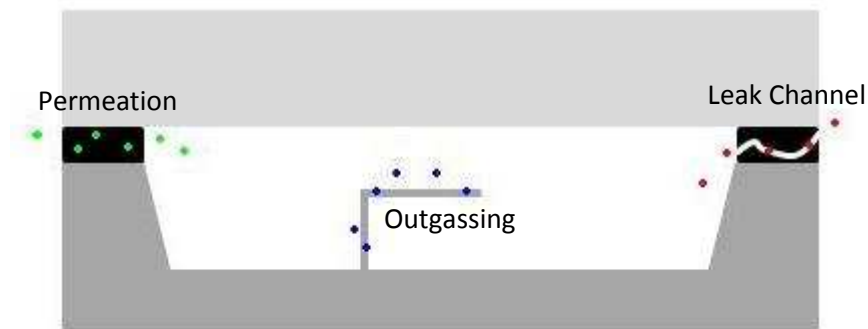
Figure 2.19: Leak types

2.4.1 Leak channels

Leak channels are usually caused by a crack in the package or seal material. Cracks can be caused by stress in the package caused by a mismatch in the materials thermal expansion coefficients. This is particularly applicable when high temperature sealing techniques are employed. Cracks may also be caused by foreign particles such as dust or debris present on the material surface during bonding. The surface roughness of the wafer before bonding can also be an issue as explained in section 2.2.2. Foreign particles or rough surfaces cause incomplete bonding leading to leak channels between the wafers or between a wafer and intermediate seal material. Gas flow through these channels can be molecular, viscous or transitional depending on dimensions of the channel and the gas characteristics. The Knudsen number is used to distinguish between the types of capillary flow [2.52]. This dimensionless number is equal to the ratio of the mean free path of the gas to the characteristic dimension, usually the radius, of the capillary [2.52]. Molecular flow occurs when the Knudsen number is greater than one. In such a case, the flow is dominated by the velocity of the gas particles, which is related to the pressure gradient. The equation for molecular flow using Poiseuille and Knudsen's formulae is given in equation 2.4 [2.52, 2.53, 2.54]

$$Q_m = \frac{2}{3}\pi\frac{r^3}{l}v_m(P_2 - P_1) \qquad (2.4)$$

where Q_m is the molecular leak rate, r is the radius of the leak channel, l is the length of the leak channel, v_m is the mean molecular speed of the gas given in equation 2.5, P_2 is the high pressure and P_1 is the low pressure.

$$v_m = \left(\frac{8R_0T}{\pi M} \right)^{1/2}$$ (2.5)

where R_0 is the universal gas constant, T is the temperature and M is the molecular mass of the gas. Viscous flow occurs when the Knudsen number is less than 0.01. The flow is then dominated by the viscosity of fluid. The viscous flow equation is shown in equation 2.6 [2.52, 2.53, 2.54].

$$Q_v = \frac{\pi r^4}{8\eta l} P_m (P_2 - P_1)$$ (2.6)

where Q_v is the viscous leak rate, η is the viscosity of the gas and P_m is the arithmetic mean of P_1 and P_2. Transitional flow is a combination of viscous and molecular flows which occurs when the Knudsen number is between the limits set for viscous and molecular flow. Equation 2.7 shows transitional flow using Poiseuille and Knudsen's formulae [2.52, 2.53, 2.54].

$$Q_t = Q_v \frac{1 + 2.507(r/mfp)}{1 + 3.095(r/mfp)} Q_m$$ (2.7)

where Q_t is the transitional leak rate and mfp is the mean free path of the gas calculated using equation 2.8.

$$mfp = \frac{k_B T}{\sqrt{2}\pi d^2 P_m}$$ (2.8)

where k_B is Boltzmann's constant and d is the molecular diameter of the gas.

Molecular flow is used by Howl and Mann to describe the helium leak rate of packages. This equation is used to relate the measured helium leak rate to the equivalent standard air leak rate in the flexible method of both MIL-STD-883 T.M.1014.13 and MIL-STD-

750E T.M.1071.8 [2.21, 2.22, 2.23]. Flow of different gases through the same capillary can be related by a simple equation as all capillary flow mechanisms are dependent on the characteristic dimension of the capillary and the size of the gas particles flowing through it. A capillary leak rate of a tracer gas can therefore be converted to capillary leak rate of another gas by Graham's Law, given in equation 2.9 [2.55].

$$L_2 = L_1 \sqrt{\frac{M_1}{M_2}} \tag{2.9}$$

where L_1 is the leak rate of one gas into a package, L_2 is the leak rate of another gas into the same package, M_1 is the molecular weight of the first gas and M_2 is the molecular weight of the second gas.

Lund and Berman published a paper shortly after Howl and Mann in 1966 which described flow through capillaries of any length to radius ratio over a range of pressures [2.56]. They intended their model to be a more general description of flow through capillary leaks [2.56]. In 1975, Davy published a paper in which he simplified the Lund and Berman model [2.57]. Figure 2.20 shows how leak channels with various geometries can be combined as one for the purpose of modelling flow and leak rates. Part (a) and (b) of figure 2.20 show that the most constricted sections of a leak channel can be combined and approximated as a capillary for ease of modelling. In this paper, Davy also describes how two packages with equal helium leak rates may not necessarily have the same leak geometries as depicted in part (c) of figure 2.20 [2.57]. Part (d) shows how a crack can be modelled as an array of capillaries. Davy explains the need for a simplified combinational leak equation to determine the rate at which a pressurized package loses its pressurization, the rate of penetration of water into a package and the maximum permissible dwell time in helium leak detection [2.57]. He considers that the leak rate measured under vacuum conditions may be the same or different to the ambient air leak rate depending on the geometry of the leak channel [2.57]. Lund and Berman firstly described this difference by way of distinguishing between molecular flow and diffusion of one gas through another due to a partial pressure gradient [2.56]. The mathematics of this type of flow differs from that of molecular flow and this is highlighted when using the helium leak test [2.57]. As the test chamber is pumped down to a vacuum during test, the molecular leak rate is always measured whereas the real leak rate may be molecular when the package is sealed in a vacuum or diffusive if

45

stored in ambient air as the package cavity gas flows out and ambient gas flows into the packages due to a partial pressure gradient.
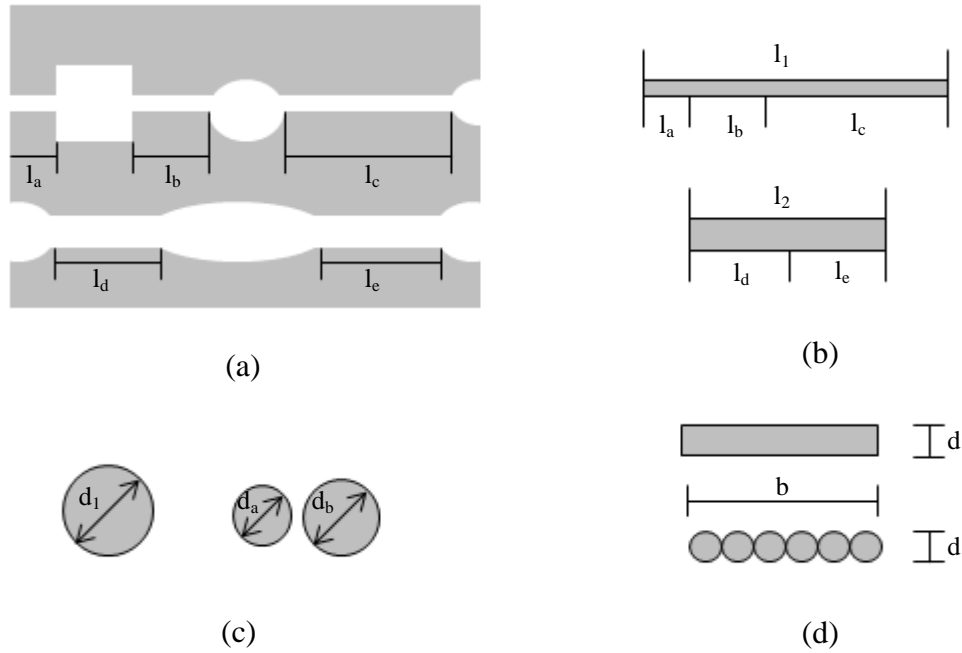
Figure 2.20: Leak schematics: (a) Side view of leaks of varying diameter. Lengths of constricted sections are indicated. (b) Capillaries equivalent to leaks in (a). (c) End view of two capillary leaks of equal leak rate $d_1 < d_a + d_b$. (d) End view of crack of breadth b and height d and an array of N capillaries of diameter d, where N=b/d.
[2.57]

Considering leak rates from a leak geometry point of view highlights the potential limitations of the traditional leak detection methods. These limitations will be explained further in Chapter 3 of this thesis.

2.4.2 Permeation

Traditional packages use non porous materials and hermetic sealing techniques to ensure a seal which is as hermetic as possible. However, new polymer sealed packages are designed to provide a low cost, low stress and low temperature sealing method for less environmentally sensitive devices. These porous materials have an intrinsic leak rate due to the permeation of gases through the bulk package or seal material. For this reason near-hermetic packages are not suitable for sealing vacuum cavities or for packaging devices in an inert gas. Polymers with low moisture permeation properties

46

such as liquid crystal polymer, LCP, benzo-cyclo-butene, BCB and Parylene can however be useful in some applications. For lifetime prediction purposes it is still essential to know the leak rate, particularly of moisture, into these types of packages.

Graham's law is applicable when Knudsen's flow is the dominant gas transport mechanism as is the case for leak rates caused by leak channels [2.55]. In such a case, the square root of the ratio of the gas molecular weights will give a good approximation of the permeation rate of one gas, knowing the permeation rate of the other through the same material. Graham's law is not applicable when any other gas transport mechanism is dominant such as surface diffusion, bulk diffusion or molecular sieving. In such cases, the rate of permeation of gases through packaging materials depends on the porosity of the permeated material, the size of the gas molecules, the weight and mean free path of the gas, and the chemical affinity of the permeating gas with the permeated material [2.56]. As the permeation rate of different gases through the same material cannot be related by Graham's Law, traditional tracer gas leak detection methods cannot be used to determine a leak rate caused by permeation.

Permeation occurs in three steps: sorption onto the material surface described by the solubility, diffusion through the bulk material to the internal cavity caused by a concentration gradient and desorption into the package cavity. Permeation can therefore be described by equation 2.10. Desorption into the internal cavity is very rapid in comparison to the rate of solubility and diffusion therefore desorption is usually assumed to be unity and equation 2.10 is simplified to equation 2.11 [2.57].

$$P = S * D * X \tag{2.10}$$

$$P = S * D \tag{2.11}$$

where P is the permeability coefficient in cm^3 at STP cm/cm^2.s.Pa, S is the solubility in cm^3 at STP/cm^3.Pa, D is the diffusivity is cm^2/s and X is the rate at which fluid desorbs from the package interior. Permeation rate unit conversions are given in Appendix A.

$$F = -D\frac{\partial c}{\partial x} \tag{2.12}$$

$$\frac{\partial c}{\partial t} = D \frac{\partial^2 c}{\partial x^2} \tag{2.13}$$

Diffusion is described well by Fick's first and second laws given in equations 2.12 and 2.13, where F is the amount of substance being transported through unit cross-section per unit time, D is the diffusion constant (diffusivity), c is the water concentration in the material, x is the distance through the package wall towards the internal cavity and t is time. However, it is unclear in the case of MEMS where the volume of the package cavity is comparable in terms of geometrical dimensions and moisture capacity to the package walls, whether one should consider permeability or diffusivity as the dominant mechanism [2.57]. In his paper Tencer describes steady state diffusion using an electrical circuit analogy. By combining equation 2.14, Ohm's Law, and equation 2.15, equation 2.16 is produced [2.57]. Equation 2.16 is the permeation equation equivalent to equation 2.15 where I is the electrical current, V is the voltage, R is the resistance, σ is the conductivity, A is the cross-sectional area, L is the length of the conductor, I_{gas} is the mass flow, P is the permeability coefficient, p is the partial pressure, A_c is the cross-sectional area of the seal with perimeter length l and height h ($A_c=h*l$) and L_s is the seal thickness.

$$I = \frac{V}{R} \tag{2.14}$$

$$I = \sigma V \frac{A}{L} \tag{2.15}$$

$$I_{gas} = Pp \frac{A_c}{L_s} \tag{2.16}$$

P, the permeability coefficient, is analogous to the electrical conductivity and the partial pressure, p, is analogous to the voltage and is the driving force behind permeation of moisture into a package cavity [2.57]. The rate of permeation of water through package materials will reduce over time as the pressure inside the package increases and partial pressure difference decreases. For lifetime modelling this can be represented mathematically although simple calculations can be useful in practical situations where a rapid decrease in the partial pressure differential, hence increase in cavity pressure indicates package failure. Tencer uses a quasi steady-state approximation to arrive at

equation 2.17 which describes the time taken for the diffusing moisture to appear in the internal cavity after the initial partial pressure differential is applied. This time is called the lag time, τ.

$$\tau = \frac{VL_s}{AP} + \frac{L_s^2}{2D} \qquad (2.17)$$

When the cavity volume is large and/or the thickness of the package wall or seal is thin and/or the cross-sectional area is small, the first term of equation 2.17 is dominant and the permeability coefficient is the most significant material property [2.57]. However, for small cavity volumes and thick absorbing walls, the second term of equation 2.17 is dominant and the diffusion coefficient is most significant [2.57].

For typical MEMS and microelectronic packages, the latter case is generally applicable. This means that the permeation rate into packages can be accurately modelled using Fick's Laws of diffusion assuming that moisture diffusion is dominant, leak rates caused by capillaries are insignificant and outgassing is minimal.

Appendix B shows the code of a simplified matlab model to predict the diffusion of moisture through a BCB seal based on a model by Veyrié published in his PhD thesis [2.60]. Figures 2.21- 2.23 show graphs of water concentration in the external ambient, throughout the package wall and in the package cavity, produced using the matlab code in Appendix B. The modelled package had a cavity volume of 1 mm^3 a BCB seal thickness of 500 μm and a cross-sectional area of 0.05 mm^2. The external ambient air has a humidity level of 10,000 ppm which is equivalent to a water concentration in air of 7.934 g.m^{-3} and the package cavity has no water content initially.
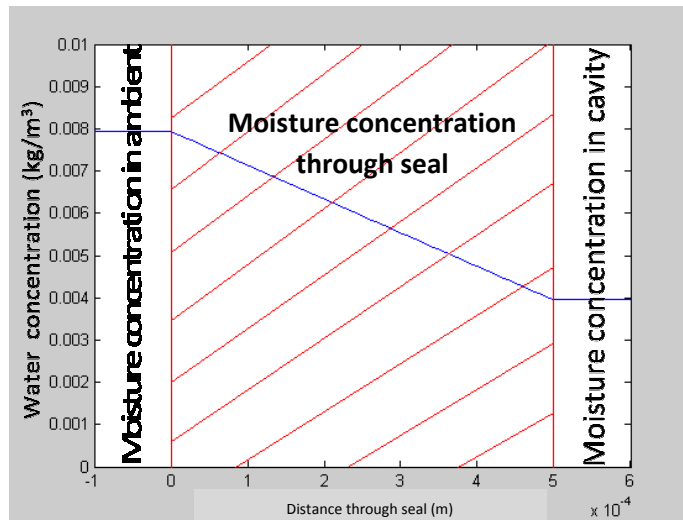
Figure 2.21: Graph of moisture concentration in BCB sealed cavity

500 μm thick seal, 10,000 ppm external ambient water concentration after 18 days

From Figure 2.21 it takes approximately 18 days before this package cavity reaches the critical 5000 ppm water. Figures 2.22 shows that when the same package is exposed to lower external humidity conditions of 5000 ppm or 3.967 g.m^{-3} the package has a lifetime of over 100 days.
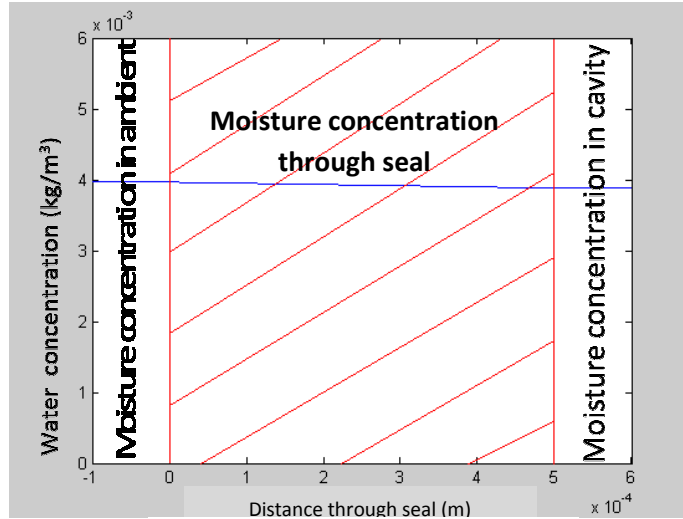
Figure 2.22: Graph of moisture concentration in BCB seal cavity

500 μm thick seal, 5000 ppm external ambient water concentration after 100 days

Depending on the ambient condition in which the package will operate, the device lifetime will vary. Typical humidity levels range from as low as 300 ppm of water in air at the poles to 40,000 ppm in the tropics [2.61]. Figure 2.23 shows a graph of water concentration in the external ambient, through the package seal and in the package

50

cavity. The initial and ambient conditions used for this model are equal to those used in the model which produced figure 2.21. This package however has a seal thickness of 1mm, double that of the first package.
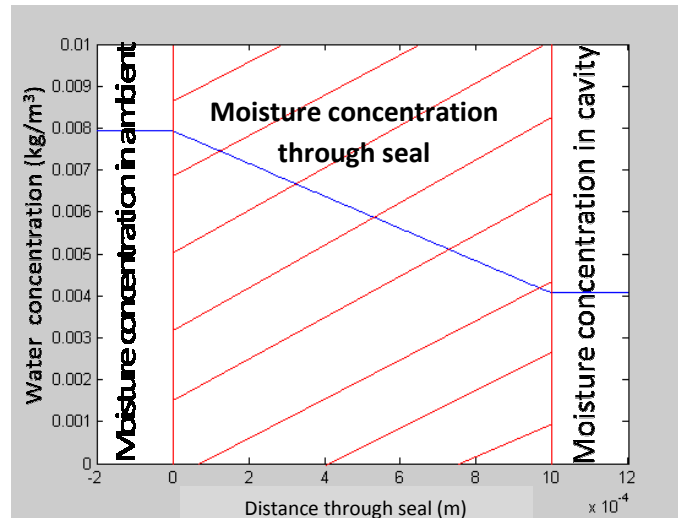
Figure 2.23: Graph of moisture concentration in BCB seal cavity
1000 μm thick seal, 10,000 ppm external ambient water concentration after 38 days

Figure 2.23 shows that the same package exposed to the same conditions will take 20 days longer (38 days in total) for the water concentration within the cavity to reach 5000 ppm when the polymer seal thickness is double. With a thicker seal, a device can have a longer lifetime under the same initial and ambient conditions. This model can be modified to determine the moisture diffusion rate through any material provided the diffusion coefficient of the material is known and the package and seal geometric dimensions are known. This model gives a good approximation of water ingress into polymer sealed packages to allow designers to establish quickly whether or not a polymer seal is suitable for their particular application. For a full understanding of water ingress, the dew point of the cavity should be taken into consideration along with consideration of variable humidity levels in the ambient environment and how this may impact on moisture ingress into the package cavity.

2.4.3 Outgassing

In ultra high vacuum applications when hermetic bonding has been optimized, it is essential to consider the amount of outgassing coming from internal device and package material layers. Outgassing can occur during high temperature bonding processes.

These residual gases are forced out from surface material layers by the elevated temperature and cannot easily be reabsorbed by the materials at lower temperatures so these gases contribute to an increase in cavity pressure. Outgassing can also occur at room temperature throughout the device lifetime as gases are released continuously from the bulk material or surface layers of internal materials. When this type of outgassing exists, the internal cavity pressure will slowly increase over the device lifetime. In the case of ultra high vacuum packaging, outgassing can be the dominant 'leak' source and even relatively small amounts of outgassing can be detrimental to the device performance leading to premature failure. Table 2.10 shows the typical vacuum requirements of several MEMS device types.

MEMS Device Type	Typical cavity vacuum required (atm)
Accelerometer	0.3 – 0.7
Absolute Pressure Sensor	$9.869 \times 10^{-4} – 9.869 \times 10^{-3}$
Resonator	$9.869 \times 10^{-5} – 9.869 \times 10^{-8}$
Gyroscope	$9.869 \times 10^{-5} – 9.869 \times 10^{-8}$
RF Switch	$9.869 \times 10^{-5} – 9.869 \times 10^{-8}$
Microbolometer	$< 9.869 \times 10^{-8}$
Optical MEMS	Moisture free

Table 2.10: Cavity vacuum requirements of typical MEMS [2.62]

As outgassing is caused by release of gases from materials it is important to know the process steps that can result in gases being absorbed into the surface layers and bulk materials used to fabricate and package MEMS. Noble gases, usually argon, are found to outgas from metals which have been sputtered during the MEMS fabrication process [2.62]. For this reason it is recommended, for vacuum packaging application, that metals are evaporated rather than sputtered. Table 2.11 show the gas types found to outgas during common level-0 wafer bonding processes.

Bonding Process	Outgassing during bond
Silicon fusion bonding	H_2, H_2O
Anodic bonding	O_2
Eutectic bonding	Noble gases
Glass frit bonding	CO, C_xH_y

Table 2.11: Outgassing during bonding [2.62]

Outgassing can be reduced by choosing carefully during the design process the best materials and process to minimise gas absorption into the fabrication and packaging

materials. In order to determine the types of gases released from materials, Residual Gas Analysis (RGA) is used. RGA can also be used to determine quantitatively and qualitatively the gas content of a package cavity. The method is destructive, time-consuming, requires expert analysis to achieve accurate results and extremely expensive, yet, can give valuable information about outgassing that no other test method can [2.62]. RGA can be performed in two ways: dynamically, for use with metals, glasses and ceramics when the pressure is low; or statically when the pressure is higher and water vapour is likely to be present [2.62].
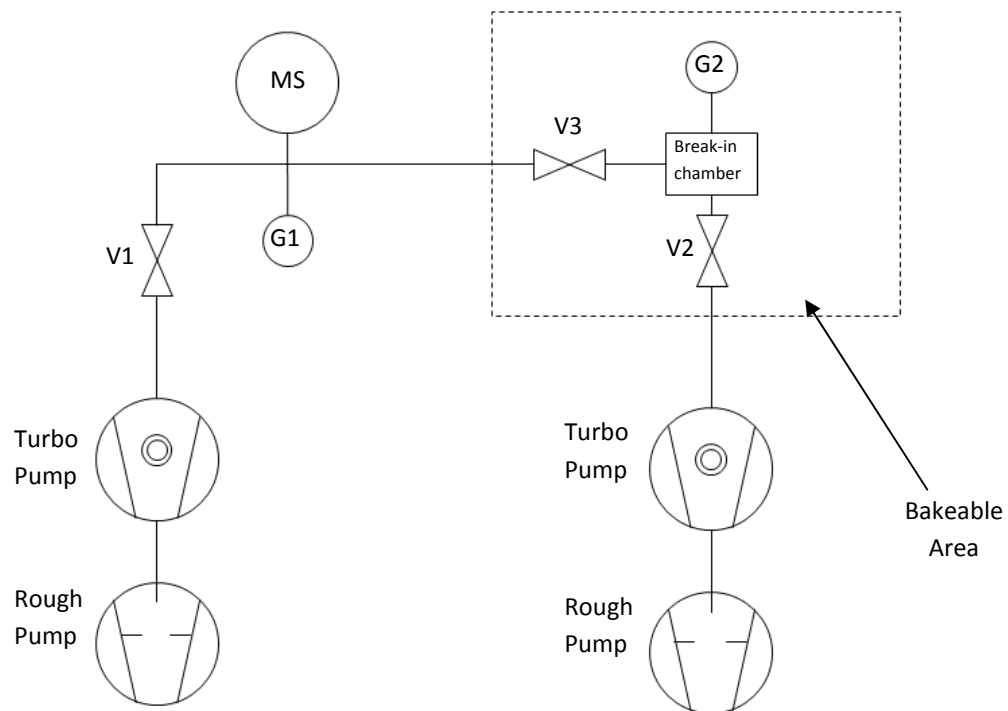
Figure 2.24: RGA schematic [2.62]

RGA is performed using a set-up similar to the one shown in figure 2.24 [2.62]. Firstly, the vacuum system is pumped down by the two turbo pumps to around 10^{-13} atm. Valve, V3, separates the vacuum system into the sample side and the analyser side and is closed to avoid exposing the analyser to air while samples are loaded [2.62]. The mass spectrometer, MS, is a quadruple mass spectrometer to increase sensitivity allowing partial pressures of around 10^{-16} atm to be measured [2.62]. The Bayard-Alpert ionisation gauge, G1, is used to calibrate the mass spectrometer for the gas species of interest [2.62]. After a new sample package is loaded, the sample side should be degassed overnight at 200 °C using a resistance oven indicated in figure 2.24

by the dotted line [2.62]. Valves V1 and V2 are closed before V3 is opened to allow the outgassing from the internal system walls to be measured [2.62]. This value is deducted from the final results [2.62]. The package is then pierced using a needle contained in the break-in chamber. As the volume of the sample and the break-in chamber is known, an absolute pressure measurement can be estimated using the spinning rotor gauge, G2 [2.62]. With V1 and V2 closed, V3 is then opened to allow the gases released from the sample package to the analyzed [2.62]. To protect the analyser this pressure should be less that 10^{-7} atm [2.62]. Spectra are collected for a few minutes and partial pressures of the gas species present are calculated from known calibration factors [2.62]. Further apparatus can be added to the set-up shown in figure 2.24 to allow RGA to be conducted statistically to reduce the pressure released to the analyser when materials such as plastics are analysed and water vapour is present in the outgassing species. In this case an absolute pressure gauge in also incorporated to measure the total pressure evolution over time [2.62].

2.5   Conclusions

From the background information provided in this chapter, it is clear that the leak detection methods currently available for use are not suitable for all MEMS or low cavity volume microelectronic packages. Table 2.12 summarises the test methods available, their minimum detectable rates, the leak types they can accurately detect and the corresponding package types for which they are applicable.

Fine leak test method	Minimum detectable rate (atm.cm^3.s^{-1})	Leak type detected	Applicable package types
Helium fine leak	10^{-11}	Leak channels	Si, metal, ceramics No glass or polymers
Radioisotope fine leak	10^{-12}	Leak channels	Si, metal, ceramics, glass. No polymers
Optical leak detection	10^{-9}	Leak channels, permeation (of tracer gas)	Any material as long as cap thickness and flexibility is appropriate
Cumulative helium leak detection	Unclear $10^{-10} - 10^{-14}$	Leak channels, permeation (of tracer gas)	Si, metal, ceramics No glass or polymers
Residual gas analysis	10^{-16} depending on MS sensitivity	Leak channels, permeation, outgassing	Any materials.

Table 2.12: Summary of existing hermeticity test methods

RGA is the only method that is able to detect all types of leak that may adversely affect MEMS and microelectronic packages. RGA is destructive, expensive and is not applicable to end-of-line testing desired by industry. Table 2.12 shows that no other method is capable of measuring outgassing or permeation other than that of a specific tracer gas. As previously discussed in section 2.4.2, leak rates caused by permeation of one gas cannot be simply mathematically related to that of another gas as is the case for molecular leaks. The optical leak detection and cumulative helium leak detection methods are therefore limited to measuring permeation rates of the test specific tracer gas only. Another leak detection method is required to measure permeation leaks and outgassing. This limitation is reflected in the applicable package types of each test method with most unable to detect leak rates of polymer packages. Due to the small molecular diameter of helium, no method that uses helium as a tracer gas can be used to determine molecular leak rates of glass packages.

Table 2.12 also shows the minimum detectable leak rate of each fine leak test method. Figure 2.8 showed that the maximum permissible leak rate of a typical MEMS package is of the order 10^{-15} atm.cm^3.s^{-1}, only RGA can detect such low leak rates. New test methods capable of measuring leak rates down to 10^{-16} atm.cm^3.s^{-1} are therefore required for MEMS applications.

Some limitations of the traditional leak detection methods available when applied to MEMS and low cavity volume microelectronic packages have been suggested in this chapter. Further details of these limitations are explained in Chapter 3 to clearly identify the rationale for the development of new hermeticity test methods.

2.6   References

[2.1]   CED, '*1947: Invention of the transistor*',
http://www.cedmagic.com/history/transistor-1947.html, (04/08/2010)

[2.2]   Texas Instruments, '*The Chip that Jack Built*', 2008,
http://www.ti.com/corp/docs/kilbyctr/jackbuilt.shtml, (04/08/2010)

[2.3]   Reed Business Info., '*The Hapless Tale of Geoffrey Dummer'*, Electronic Product News, 2005.

[2.4]   C. Lécuyer, '*Making Silicon Valley: Innovation and the Growth of High Tech, 1930-1970',* MIT Press, 2006.

[2.5]   '*First transistor*', 2007, http://www.electronics-lab.com/blog/wp-content/uploads/2007/12/hr-1sttransistor.jpg, (04/08/2010)

[2.6]   A. Orlowski, '*The chip started here*', 2005, http://regmedia.co.uk/2005/06/21/ic_large.jpg, (04/08/2010)

[2.7]   G.E. Moore, '*Cramming more components onto integrated circuits*' Electronics, 38 (8), 1965.

[2.8]   M. Kanellos, '*New Life for Moore's Law*', 2005.   http://news.cnet.com/New-life-for-Moores-Law/2009-1006_3-5672485.html, (04/08/2010)

[2.9]   Intel, '*Moore's Law*', http://www.intel.com/technology/mooreslaw/, (04/08/2010)

[2.10]   M.J. Madou, '*Fundamentals of Microfabrication. The Science of Miniturization*', Second Edition, CRC Press LLC, 2002.

[2.11]   iNEMS, '*History of MEMS technology*', 2006, http://inems.com/MEMS_course_AREA/01_introduction/MEMS_History.htm, (04/08/2010)

[2.12]   Wu, '*A brief MEMS history*', 2009, http://mems.caltech.edu/courses/EE185/00%20MEMS%20Intro.pdf, (04/08/2010).

[2.13]   Ed: G.Q. Zhang and A.J. Roosmalen, '*More Than Moore. Creating High Value Micro/Nanoelectronics Systems*', Springer, New York, 2009.

[2.14]   F.N. Sinnadurai, '*Handbook of Microelectronics Packaging and Technologies'*, Electrochemical Technologies, 1985.

[2.15]   H. Greenhouse, '*Hermeticity of Electronic Packages*', William Andrew publishing, 2000.

[2.16]   A.O. Nier, C.M. Stevens, A. Hustrulid and T.A. Abbott, '*Mass spectrometer for leak detection*', Journal of Applied Physics, 18 (30), pp. 30-33, 1947.

[2.17]   S. Millar, M.P.Y. Desmulliez and W. Yu, '*A review of hermeticity test methods for packages with small cavities (invited paper)*', Proceedings IMAPS - CPMT Poland 2009, Gliwice, Pszczyna, Poland, 2009.

[2.18]   G. Neff and J. Neff, '*Leak testing electronics devices in production quantities*', IsoVac Engineering, 1986.

[2.19]   N. Sinnadurai, '*Plastic packages survive where hermetic packages fail*', Microelectronics Reliability, 36 (7/8), pp 1001-1018, 1996.

[2.20] K. Zapfe, '*Leak detection*', Deutsches Elektronen-Synchrotron DESY, Hamburg, Germany, 2007.

[2.21] D.A. Howl and C.A. Mann, '*The Back-Pressurization Technique of Leak Testing*', Vacuum, vol.15, pp. 347-352, 1965.

[2.22] MIL-STD-883H T.M. 1014.13, '*Seal*', United States of America Department of Defence, Test method standards, Microcircuits, pp. 81-99, 2010.

[2.23] MIL-STD-750E T.M.1071.8, '*Hermetic seal*', United States of America Department of Defence, Test Method Standard, Test Methods for Semiconductor Devices, pp. 100-116, 2006.

[2.24] J. Newman, '*Optical leak testing of hermetic optoelectronic devices*', Norcom Systems Inc., 2001,

[2.25] J. Pernicka, '*The cumulative helium leak detector*', Pernicka Corporation, 2005.

[2.26] A.R. Mirza, '*Silicon wafer bonding for MEMS manufacturing*,' MEMS Technology, 1999.

[2.27] Fraunhofer, '*MEMS Packaging*',
http://www.enas.fraunhofer.de/EN/abteilungen/avt/forschungsschwerpunkte/MEMSPackaging/index.jsp, (03/08/2010)

[2.28] J.M. Bustillo, R.T. Howe and R.S. Muller, '*Surface micromachining for microelectromechanical systems*', Proceedings of the IEEE, 86 (8), 1998.

[2.29] W.A. Rogers, R.S. Buritz and D. Alpert, '*Diffusion coefficient, solubility and permeability for helium in glass*', Journla of Applied Physics, 25 (7), pp. 868-875, 1954.

[2.30] V.O. Altemose, '*Helium Diffusion through Glass*', Journal of Applied Physics, 32 (7), pp. 1309-1316, 1961.

[2.31] K.M. Striny, '*Assembly techniques and packaging of VSLI Devices*,' in VSLI Technology, Ed: S.M. Sze, McGraw-Hill, New York, 1988.

[2.32] J. Noworolski, E. Klassen, J. Logan, K. Petersen and N.I. Maluf, '*Fabrication of SOI wafers with buried cavities using silicon fusion bonding and electrochemical etchback*', Sensors and Actuators A, 54, pp. 709-713, 1996.

[2.33] N. Lorenz, S. Millar and D. Hand, '*Localised laser joining of micro-devices for hermetic packaging using a glass frit intermediate layer*', Proceedings of the 5th International WLT-Conference on Lasers in Manufacturing, Munich, (2009).

[2.34] F. Niklaus, '*Adhesive wafer bonding*', Journal of Applied Physics, 99 (3), 2006.

[2.35] N. Kingsley, S.K. Bhattacharya and J. Papapolymerou, '*Moisture lifetime testing of RF MEMS switches packaged in liquid crystal polymer*', IEEE Transactions on Components and Packaging Technologies, 31 (2), pp. 345-350, 2008.

[2.36] K-I. Kim, J-M. Kim, G-C. Hwang, C-W. Baek and Y-K. Kim, '*Packaging for RF MEMS devices using LTCC sunstrate and BCB adhesive layer*', Journal of Micromechanics and Microengineering, 16, pp. 150-156, 2006.

[2.37] M.J. Chen, A-V. H. Pham, N.A. Evers, C. Kapusta, J. Iannotti, W. Kornrumpf, J.J. Maciel and N. Karabudak, '*Design and development of a packagae using LCP for RF/Microwave MEMS switches*', IEEE Transactions on Microwave Theory and Techniques, 54 (11), pp. 4009-4015, 2006.

[2.38] A. Jourdain, P. De Moor, S. Pamidighantam and H.A.C. Tilmans, '*Investigation of the hermeticity of BCB-sealed cavities for housing (RF-)MEMS devices*', IEEE International Conference, Las Vegas, USA, 2002.

[2.39] A. Jourdain, P. De Moor, K. Baert, I. De Wolf and H.A.C. Tilmans, '*Mechanical and electrical characterisation of BCB as a bond and seal material for cavities housing (RF-)MEMS devices*', Journal of Micromechanics and Micrengineering, 15, pp. S89-96, 2005.

[2.40] H. Zhang, Q. Zhang, D. Pinjala, X. Liu and P-K. Chan, '*Development and characterisation of large silicon microchannel heat sink packages for thermal management of high power microelectronics modules*', IEEE Electronic Components and Technology Conference, pp. 1018-1022, 2006.

[2.41] T. Velten, H.H. Ruf, D. Barrow, N. Aspragathos, P. Lazarou, E. Jung, C. K. Malek, M. Richter, J. Kruckow and M. Wackerle, '*Packaging of bio-MEMS: strategies, technologies and applications*', IEEE Transactions on Advanced Packaging, 28 (4), pp. 533-546, 2005.

[2.42] P-J. Chen, D.C. Rodger, R. Agrawal, S. Saati, E. Meng, R. Varma, M.S. Humayun and Y-C. Tai, '*Implantable micromechanical parylene-based pressure sensors for unpowered intraocular pressure sensing*' Journal of Micromechanics and Microengineering, 17, pp. 1931-1938, 2007.

[2.43] I. De Wolf, A. Jourdain, P. De Moor, H.A.C. Tilmans and L. Marchand, '*Hermeticity Testing and Failure analysis of MEMS Packages*', 14th International Symposium on the Physical and Failure Analysis of Integrated Circuits, pp. 147-154, 2007.

[2.44] S. Millar and M.P.Y. Desmulliez, '*MEMS ultra low leak detection methods: a review*', Sensor Review, 29 (4), pp. 339-344, 2009.

[2.45] A. Goswami and B. Han, '*On Ultra-Fine Leak Detection of Hermetic Wafer Level Packages*', IEEE Transactions on Advanced Packaging, 31(1), pp. 14-21, 2008.

[2.46] Laco Technologies, '*Leak test bombing chambers*', http://lacotech.com/cgi-bin/in1.pl?inview=B2-38&id=178&show=887#products, (03/08/2010).

[2.47] STMicroelectronics, *'Disposable Insulin Nanopump from Debiotech and STMicroelectronics Marks Major Breakthrough in Diabetes Treatment'* 2007.

[2.48] F. Bardin, S. Kloss, C. Wang, A.J. Moore, A. Jourdain and I. De Wolf, '*Laser binding of glass to silicon using polymer for microsystems packaging*', Journal of Micoelectromechanical Systems, 16(3), pp. 571-580.

[2.49] T. Green, '*A practical guide to TM 1014 (seal)'* TJ Green Associates LLC, 2010.

[2.50] G. Elger, L. Shiv, N. Kikac, F. Muller, R. Liebe, M. Grigat, and M. Heschel, '*Optical leak detection for wafer level hermeticity testing',* IEEE Semiconductor International Electronics Manufacturing Technology Symposium, 2004.

[2.51]   J. Newman and S. Thayler, '*Optical leak testing of Hermetic Semiconductor, MEMS and optoelectronics devices*', Norcom Systems Inc, 2002.

[2.52] M. Knudsen, '*The kinetic theory of gases*', Methuen & Co. Ltd, London, 1934.

[2.53] Y.Tao and A.P. Malshe, '*Theoretical investigation on hermeticity testing of MEMS packages based on MIL-STD-883E*', Microelectronics Reliability, 45, pp. 559-566, 2005.

[2.54] S. Dushman and J.M. Lafferty, '*Scientific foundations of vacuum technique*', Second Edition, New York: John Wiley & Sons, 1962.

[2.55] A. Ruckstuhl, '*Thomas Graham's study of the diffusion of gases*', Journal of Chemical Education, 1951, pp 594-596.

[2.56] L.M. Lund and A.S. Berman, *'Flow and self diffusion of gases in capillaries, part I & part II'*, Journal of applied physics, 37(6), pp.2496-2508, (1966).

[2.57] J. Davy, *'Model calculations for the maximum allowable leak rates of hermetic packages'*, Journal of vacuum science and technology, 12(1), pp. 423-429, 1975.

[2.58] D. Fain, '*Development of inorganic membranes for gas separation*', http://www.netl.doe.gov/publications/proceedings/02/materials/fain.PDF, (03/08/2010).

[2.59] M. Tencer, '*Moisture ingress into nonhermetic enclosures and Packages. A quasi-steady state model for diffusion and attenuation of ambient humidity variations*', Proceedings of the 44th Electronic Components & Technology Conference, pp. 196-209, 1994.

[2.60] D.Veyrié, '*Approche alternative de l'évaluation de l'herméticité des micro cavitiés – application au packages des MEMS*', PhD Thesis, Université Bordeaux 1, 2007.

[2.61] E. Uherek, '*Dimensions: Water, Moisture, Air*', *Water Vapour – A Greenhouse Gas*, http://www.espere.net/Unitedkingdom/water/uk_dimensions.html, (28/07/2010).

[2.62] M. Moraja, '*Hermetic Packaging Design of MEMS*', FSRM Courses in Microtec and Nanotec, 2010.

Chapter 3

Limitations of the hermeticity test method and industry standards

Chapters 1 and 2 have detailed various limitations of traditional hermeticity test methods for microelectronics and MEMS packages with low cavity volume. These limitations are explained and quantified in this chapter. Each fine leak and combinational leak test method is examined. The minimum detectable leak rate of the gross leak test methods is considered to be around 1×10^{-4} atm.cm^3.s^{-1} and so each fine leak test requires a maximum detectable leak rate which exceeds this in order to avoid a gap in the range of leak rate that can be detected. Combinational testing, a single test method that detects both fine and gross leaks, is considered advantageous in industry as test time is reduced and most methods are non-destructive meaning that 100% hermeticity screening is possible.

The theory in this chapter is essential to determine the precise limitations of the helium leak test when applied to low cavity volume packages and vacuum packaged MEMS. The Howl-Mann equation is used to derive a novel expression which can be used to determine the minimum cavity volume package which can be successfully helium leak tested in conjunction with an appropriate gross test. This expression is particularly useful since it allows users to determine the most appropriate test parameters for packages with volumes that approach the minimum. It can also be used to prove whether or not the helium leak test is an appropriate fine leak test method for a particular package. For vacuum packaged MEMS, an expression is derived from the Howl-Mann equation which can be used to determine the lowest equivalent air leak rate that can be measured using the helium leak test method for a particular package. This expression allows users to exploit test parameters to ensure the minimum possible leak rate is measurable, which is of particular importance to vacuum packaged devices.

3.1   Limitations of the helium fine leak test method

The limitations of the helium fine leak test used in conjunction with the gross bubble test can be explained and quantified by examining the Howl-Mann equation, reproduced

in equation 3.1 [3.1]. This equation yields the measured helium leak rate, R, as a function of the true leak rate, L. P_b is the bomb time, P_0 is the atmospheric pressure, M_A is the molecular weight of air, M_{He} is the molecular weight of helium, t_b is the bomb time, V is volume and t_d is the dwell time. The definitions of these times have been given in Chapter 2 although for clarity the measured helium leak rate, R, is the rate at which helium, which has previously been pressurised into the package, leaks out of the package under test conditions. The true leak rate also referred to as the equivalent standard leak rate, L, is the rate at which air would leak into a package with a measured helium leak rate equal to R, under standard conditions of temperature and pressure.

$$
R = \underbrace{\frac{LP_b}{P_0}\left(\frac{M_A}{M_{He}}\right)^{1/2}}_{(a)}\ \underbrace{\left(1 - \exp^{\frac{-Lt_b\left(\frac{M_A}{M_{He}}\right)^{1/2}}{VP_0}}\right)}_{(b)}\ \overbrace{\exp^{\frac{-Lt_d\left(\frac{M_A}{M_{He}}\right)^{1/2}}{VP_0}}}^{(c)}
\tag{3.1}
$$

The Howl-Mann equation can be explained in simple terms by considering the equation in three parts as shown in equation 3.1. Part (a) converts the true air leak rate or equivalent air leak rate to a helium leak rate given bomb pressure, P_b. Part (b) gives the amount of helium leaking into the package during bomb time, tb, given the true air leak rate, L, converted to a helium leak rate using the ratio in molecular weights. Part (c) gives the amount of helium leaking out of the package during the dwell time, t_d, given the true air leak rate, L, converted to a helium leak rate using the ratio in molecular weights. Overall the Howl-Mann equation is used to convert a known air leak rate to a helium leak rate at a known bomb pressure, P_b, taking into consideration the amount of helium leaking into the package during the bomb time, t_b, and the amount of helium which leaks out of the package during the dwell time, t_d. The true air leak rate of the package, L, appears in each of the three parts of the Howl-Mann equation with the measured helium leak rate as the subject making the re-arrangement of the equation to obtain L as the subject complex. For this reason it is common practise to set the reject true air leak rate or equivalent standards air leak rate for a specific package, insert this along with the test parameters into the Howl-Mann equation and obtain a reject helium leak rate, R. However, for the purposes of determining the limits of the helium leak test method it is essential to consider the Howl-Mann in two parts; helium leaking into the package during the bomb time and helium leaking out during the dwell time.

3.1.1 Volume Limitations

Figure 3.1 shows variations of the measured leak rate as a function of the true leak rate for cavity volumes ranging from 10^{-5} cm^3 to 10 cm^3. For these plots, the normal conditions of use are P_b=5 atm, t_b=6 hours, t_d=10 minutes and P_0=1 atm. For each measured leak rate there are two possible true leak rates defined here as L_{upper} and L_{lower}. The minimum true leak rate detectable using a gross bubble test is indicated by a vertical line in figure 3.1.
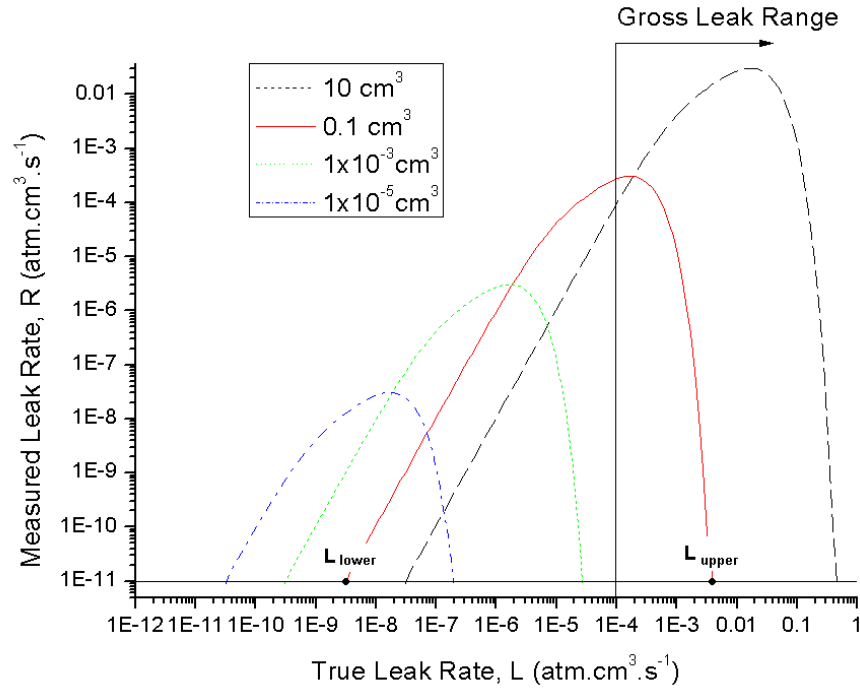
Figure 3.1: Measured helium leak rate given as a function of the true helium leak rate for different cavity volumes. The maximum sensitivity of most helium leak detectors, 10^{-11} atm.cm^3.s^{-1} is given as a horizontal line in the figure. As an example, L_{lower} and L_{upper} have been indicated in the case of a cavity of volume of 0.1 cm^3.

The purpose of the gross leak test is to rule-out or confirm the relevance of the upper true leak rate, L_{upper}. During the fluorocarbon gross leak test, the absence or presence of bubbles escaping from the test sample indicates whether or not a gross leak is present. If no bubbles are observed, the measured leak rate is reflecting the lower value of the true leak rate, L_{lower}; if bubbles are detected, a gross leak is present and the measured leak rate is reflecting the upper value of the true leak rate, L_{upper}. In the latter

63

case, the helium present inside the package after bombing escapes through a gross leak channel very quickly during the dwell time so when the package is tested, either a very low helium leak rate is measured or the leak rate is negligible. As the volume of the cavity is reduced, the upper leak rate drops below the minimum detectable leak rate of the gross test invalidating the traditional test methods. There is no possibility in this case to know whether the measured leak has been caused by the lower true leak rate or upper true leak rate and so the helium leak test method in combination with a gross leak test method is invalid.

In order to determine the limits of validity of the helium leak test method, it would be advantageous to derive analytically the upper limit of the true leak rate at the detection limit of the leak detector which is typically 10^{-11} atm.cm^3.s^{-1} helium. As L_{upper} decreases with cavity volume, it would be desirable to attempt to raise this limit by optimising the test variables using an analytical expression for L_{upper}. If L_{upper} can be increased beyond the minimum detectable leak rate of the gross test, the helium fine leak test method could still be validated for a defined minimum cavity volume. In the region where L_{upper} lies, the true leak rate is large and for small cavity volumes the value within the brackets in equation 3.1 tends to unity such that:

$$R = \frac{LP_b}{P_0}\left(\frac{M_A}{M_{He}}\right)^{1/2}\exp^{\frac{-Lt_d\left(\frac{M_A}{M_{He}}\right)^{1/2}}{VP_0}} \tag{3.2}$$

Equation 3.2 can be re-arranged to be of the form $z=f(y)=ye^y$ as shown in equation 3.3.

$$z = \frac{Rt_d}{VP_b} = \frac{Lt_d}{VP_0}\left(\frac{M_A}{M_{He}}\right)^{1/2}\exp^{\frac{-Lt_d\left(\frac{MA}{M_{He}}\right)^{1/2}}{VP_0}} \tag{3.3}$$

with

$$y = \frac{Lt_d}{VP_0}\sqrt{\frac{M_A}{M_{He}}} \tag{3.4}$$

The inverse function of z, allows the determination of y or L as a function of R. This can be achieved using the Lambert-W function [3.2]. Using this function,

$$L_{upper} = \frac{-W(z)VP_0}{t_d \left(\dfrac{M_A}{M_{He}}\right)^{1/2}} \tag{3.5}$$

Where $z = (Rt_d/VP_b)$, in the equation above, is the argument of the Lambert-W function. For sufficiently small z, the following asymptotic formula can be used to obtain an approximation for $W(z)$ [3.2].

$$W(z) = \ln z - \ln \ln z + \sum_{k=0}^{\infty} \sum_{m=0}^{\infty} c_{km} \left(\ln \ln z\right)^{m+1} \left(\ln z\right)^{-k-m-1} \tag{3.6}$$

Figure 3.2 shows a comparison of the L_{upper} versus cavity volume calculated using equation 3.7 and that derived from equation 3.1.
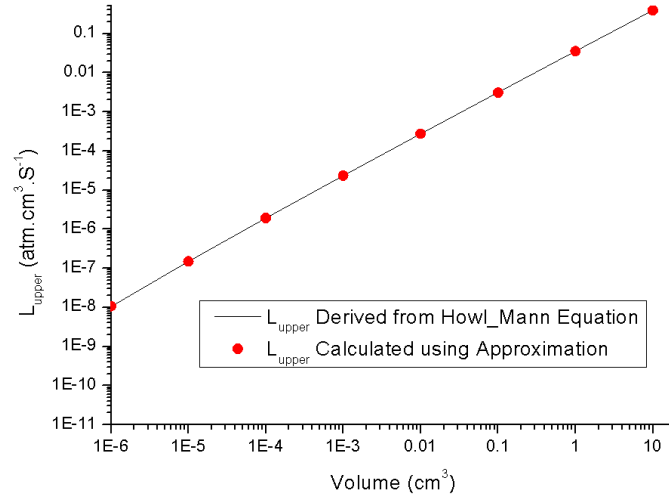
Figure 3.2: L_{upper} as a function of cavity volume $R=1\times10^{-10}$ atm.cm^3.s^{-1}, $P_b=5$ atm, $t_b=1$ hour, $t_d = 10$ minutes

For all practical purposes and under normal test conditions, the first two terms of this approximation are sufficient and provides a goodness of fit of value above 0.99 between the closed form expression of L_{upper} given by equation 3.7, and its numerical derivation using equation 3.1. This approximation shows that L_{upper} can be strongly influenced by the volume of the cavity, V, and the dwell time, t_d such that:

$$L_{upper} = \frac{-[\ln z - \ln \ln z]VP_0}{t_d \left(\dfrac{M_A}{M_{He}}\right)^{1/2}}$$

(3.7)

From equation 3.5, for any cavity volume, the highest value of L_{upper} is given for the lowest practical value of the dwell time. Although the argument of the Lambert-W function contains the dwell time and bomb pressure, this function depends only weakly on these variables and is dominated by the limit of the measured leak rate, R, and the cavity volume. It can therefore be surmised, as shown in figure 3.3, that the upper limit is inversely proportional to the dwell time. Practically, the dwell time cannot be reduced indefinitely. A minimum dwell time of around 3 minutes is recommended for practical purposes [3.3].
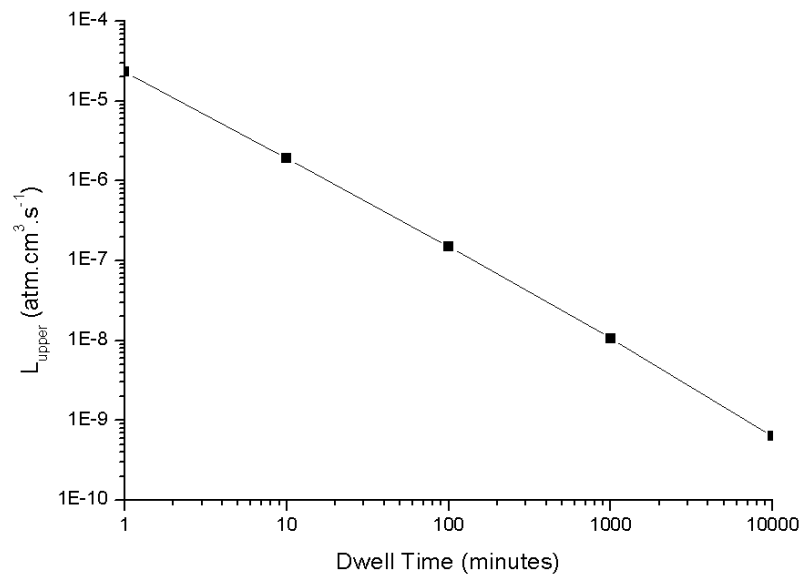
Figure 3.3: L_{upper} as a function of the dwell time for $R=1\times10^{-11}$ atm.cm^3.s^{-1}, $P_b=5$ atm, $t_b= 6$ hours, $V = 1x10^{-4}$ cm^3

Figure 3.4 shows the relationship between the cavity volume and upper true leak rate measurable using the helium leak test for a dwell time of 3 minutes, the practical limit, and 1 hour, as specified by the standards when all other variables are kept constant. From this figure, the helium leak test can be used accurately in conjunction with a gross leak test that can measure leak rates above 1×10^{-4} atm.cm^3.s^{-1} for packages with internal cavity volumes of 2.6×10^{-3} cm^3 or greater when the dwell time is kept to the practical minimum of three minutes.

For industrial applications, batches of packages are usually checked for hermeticity. In such cases, it may be necessary to allow a dwell time longer than 3 minutes in order to bomb and test as many packages as possible in a single test run but it is still essential to ensure enough helium remains inside the cavity to achieve an accurate measurement. For a dwell time of one hour, packages with internal cavity volumes of 0.052 cm^3 or greater can be tested accurately.
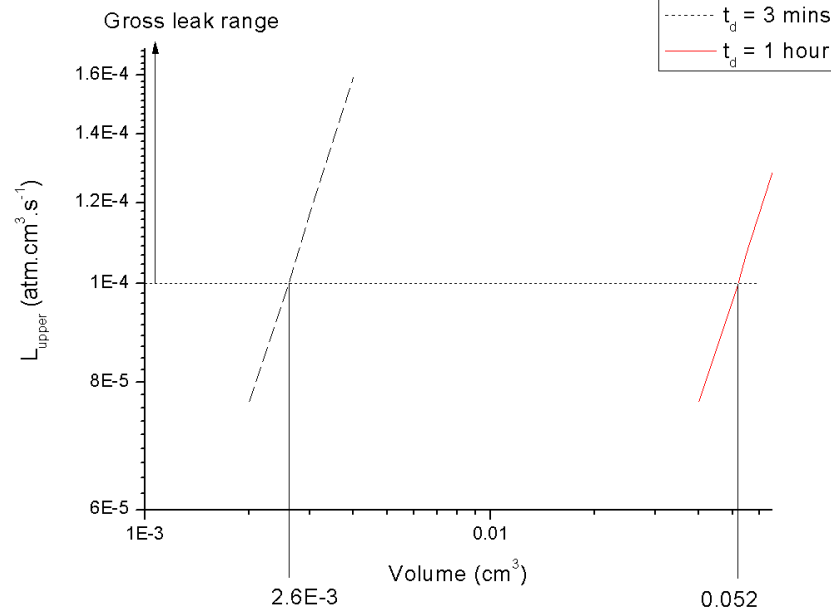
Figure 3.4: L_{upper} as a function of volume for $R=1\times10^{-11}$ atm.cm^3.s^{-1}, $P_b=5$ atm, $t_b= 6$ hours.

3.1.2 Minimum detectable leak rate

The lowest measurable leak rate of most helium leak detectors is dictated by the sensitivity of the mass spectrometer used. The lowest true leak rate, L_{lower}, however depends on the bomb pressure, bomb time and sample cavity volume. The analytical dependence of these variables on L_{lower} can be obtained by reducing the Howl-Mann equation such that:

$$R = \frac{LP_b}{P_0}\left(\frac{M_A}{M_{He}}\right)^{1/2}\left(1-\exp^{\frac{-Lt_b\left(\frac{M_A}{M_{He}}\right)^{1/2}}{VP_0}}\right) \qquad (3.8)$$

In the region of interest, the exponential term in the brackets can be approximated using a Maclaurin expansion and the equation re-arranged to give L_{lower} in terms of the measured leak rate.

$$L_{lower} = P_0 \sqrt{\frac{RV}{P_b t_b} \left(\frac{M_{He}}{M_A} \right)^{1/2}} \qquad (3.9)$$

A reduction in the volume of the cavity decreases the true minimum leak rate. The same trend is observed if the bomb time or the bomb pressure is increased. Practically, the bomb pressure and time cannot be increased indefinitely. As the bomb pressure is increased, the likelihood of the sample package experiencing a 'one-way leak' is increased. A 'one-way leak' occurs when the bomb pressure induces a leak channel that under normal operating conditions would not be present. The helium then enters the package during the bombing process and upon release the induced leak channel closes, trapping the helium inside the package. Since the helium test relies on measuring the helium leaking out of the cavity after bombing, it is impossible to determine when a one-way leak has occurred using this method. It has become common practise to keep the bomb pressure between 3 and 10 atm, 5.103 atm (75 psi) is recommended in the military standards.

The bomb time can be increased depending on the time available for test. Figure 3.5 shows the dependence of L_{lower} on the bomb time for a measurable minimum leak rate of 10^{-11} atm.cm^3.s^{-1}, a minimum cavity volume of 2.6×10^{-3} cm^3 and bombing pressure of 5.103 atm. Increasing bomb time above 12 hours has a minimal effect in reducing the minimum true leak rate. Using these test parameters with the minimum cavity volume defined in the previous section as 2.6×10^{-3} atm.cm^3.s^{-1}, the minimum detectable leak rate of the helium leak test method is 1.28×10^{-10} atm.cm^3.s^{-1}. This minimum leak rate guarantees that the ambient environment of a 0.1 mm^3 cavity package sealed in 9.87×10^{-5} atm is kept within 10% of its initial pressure for less than 4 minutes. Leak rates of the order 10^{-16} atm.cm^3.s^{-1} are required for low volume, vacuum packaging of typical MEMS. The fine leak test is therefore clearly inadequate for the measurement of the hermeticity of devices with low cavity volumes.
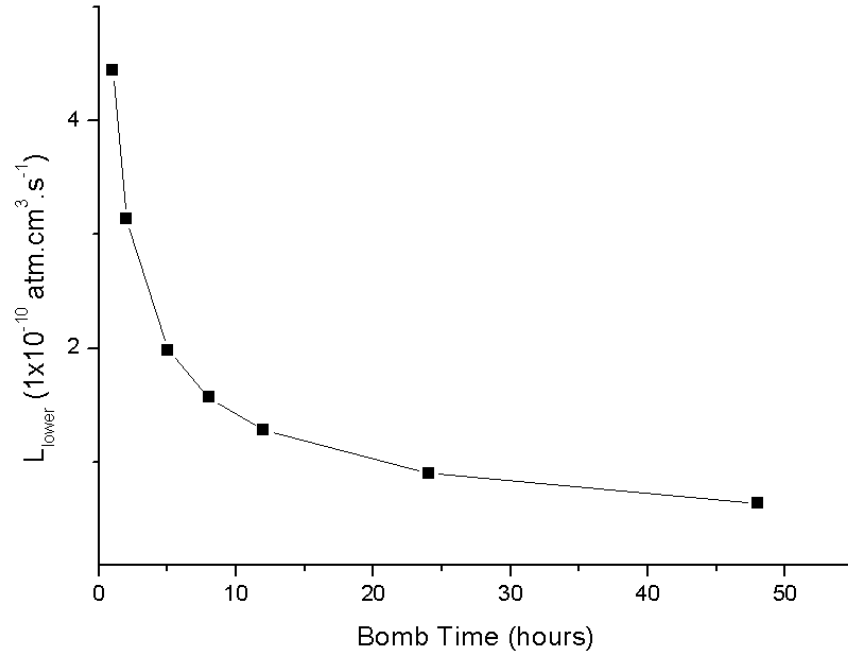
Figure 3.5: L_{lower} as a function of the bomb time for $R=1\times10^{-11}$ atm.cm³.s⁻¹, $P_b=5.103$ atm and $V=2.6\times10^{-3}$ cm³

3.1.3 Limitations of the packaging material

As most packages are stored in an ambient air environment, air leak rates are normally used to compare the hermeticity properties of packaging materials and bonding techniques. A true helium leak rate is converted to a true air leak rate by Graham's Law using the molecular weights of air, M_A, and helium, M_{He}, as shown in equation 3.10. This expression is incorporated into the Howl-Mann equation to give a helium reject leak rate, R, for the test parameters used and the true air leak rate, L, which the package under test must not exceed according to the military standards.

$$L_{Air} = L_{He}\sqrt{\frac{M_{He}}{M_{Air}}} \qquad (3.10)$$

To achieve a value for the air leak rate from a helium leak rate, an average value of the atomic weight of air, 28.7g, is used. This gives an accurate value when the leak rate is caused by a leak channel present in the package wall or seal.

69

In the MEMS manufacturing industry, glass is often used as a package material to allow optical access to the device. Other packaging materials, in particular polymer seals, are increasingly being used to replace traditional metallic packages. These materials offer advantages such as lower bonding temperatures and pressures which allow sensitive structures to be submitted to less thermo-mechanical stress during packaging. As some of these materials are porous and therefore not hermetic, the package has an intrinsic leak rate caused by diffusion through the package walls even in the absence of leak channels. For some MEMS applications hermeticity is not essential and the benefits these materials bring to the manufacturing process outweigh the problems associated with contamination. However, it is still necessary to know the leak rate of the packages to assist in the lifetime predictions of the device.

As explained in Chapter 2, during the bombing process of the helium leak test, helium will permeate slowly through the package material into the cavity. This permeation is achieved by sorption onto the surface, then diffusion through the bulk material followed by desorption into the cavity [3.4]. When the package is transferred to the mass spectrometer and the chamber is evacuated, the reverse process occurs. Over time the helium that permeated into the cavity during bombing will permeate out and be detected by the mass spectrometer. The mathematical descriptions of a permeation leak and a leak caused by fluid travelling through a leak channel are very different as explained in section 2.4.2. The traditional helium leak test cannot differentiate between helium coming through a leak channel and desorbed helium from a package material surface. Moreover, the Howl-Mann equation is applicable only to molecular leaks [3.1]. Therefore, should the measured leak rate be caused by permeation, the conversion from a measured leak rate to a true leak rate using the Howl-Mann equation is incorrect.

For package materials such as glass and polymers, the tracer gas may not have permeated through the bulk materials into the package cavity at all, yet a leak rate is measured due only to helium which has sorbed into the surface of the materials. To prove this limitation, the following experiment was conducted. Firstly we must consider that a certain amount of time will pass between the dwell time ending, i.e. the sample being placed in the mass spectrometer and the test chamber being evacuated before a reliable measured leak rate can be read. This time was defined by Goswami et al. as *the zero time* [3.5]. The zero signal defined by Goswami et al. shows the amount of time required to evacuate the test chamber and achieve a steady minimum leak rate when the

test chamber is empty [3.5]. Figure 3.6 shows a graph of measured leak rate over time. The zero signal of the experimental set-up is represented by the solid black line. To test the amount of helium sorbed into package materials leaking out during hermeticity measurement, two test samples were fabricated. A 10.1x10.1x1.2 mm borosilicate glass chip, and a 6.2 mm diameter, 15 μm thick BCB ring on silicon were made with no cavities present so only bulk material was tested. These samples were bombed separately in helium at 4 atm for 4 hours and transferred to the helium leak detector. Figure 3.6 shows that the helium leaking out of the glass chip and BCB ring are orders of magnitude higher than the minimum leak rate of the set-up after 28 seconds when the zero signal was stabilised. When conducting the helium leak test, the first reading given by the leak detector after initialisation, zero signal stabilisation, is taken as the measured leak rate. The measured leak rate of the glass chip and BCB ring are therefore, 8×10^{-8} atm.cm^3.s^{-1} and 9×10^{-6} atm.cm^3.s^{-1}, respectively, although neither sample contains a cavity into which helium could have leaked. Any helium sorption into silicon is insignificant when the zero signal method is applied [3.5], therefore the measured helium leak rate of the second sample is due to sorption of helium into the BCB ring and not the silicon substrate.

This experiment shows that helium is leaking out of the glass and polymer material. Erroneous leak rates will therefore be measured and it is possible that suitably hermetic packages are rejected. The military standards now indicate that a wait time is necessary if permeable materials are present in the sample packaging or device. This wait time is additional to the dwell time necessary to test. Therefore the minimum cavity volume of package for which the full leak range is covered by the traditional helium fine leak test used in conjunction with a gross leak test, is increased. As industry moves towards lower cavity volumes and new packaging materials, this issue becomes increasingly problematic and impacts on common package types which are manufactured in high volumes. The need for new hermeticity test methods will become more apparent when this limitation is realised and understood.
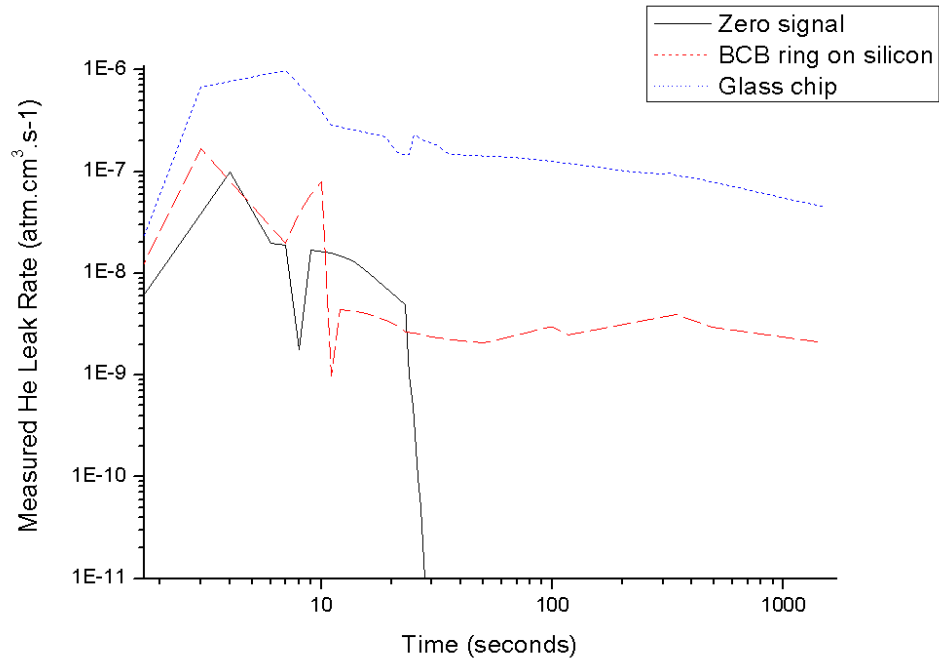
Figure 3.6: Leak rate over time showing zero signal and significant helium leaking from glass chip and BCB ring

For these reasons, it is not possible to achieve accurate leak rates of permeable packages using the traditional helium leak test. To measure leak rates caused by leak channels in permeable packaging materials, tracer gases which do not permeate through the material must be used. In the case of glass, nitrogen can be used as a replacement for helium. For polymer materials, another type of test must be found as most gases will permeate through polymers at different rates depending on the porosity of the permeated material, the size of the gas molecules, the weight and mean free path of the gas, and the chemical affinity of the gas with the permeated material. *In-situ* test structures could provide a solution to the testing issues associated with permeable packaging. However, if the package concerned is not hermetic and permeation rates are dominant, the determination of the permeation constants for typical gases through packaging materials could allow package leak rates to be modelled successfully.

3.2 Limitations of the radioisotope fine leak test

The radioisotope leak test has been available for use in industry since its first use in 1959 [3.6]. The test method has not been as widely accepted by industry as the helium fine leak test. The main reasons which have been proposed for this are the capital cost

and the safety consideration of using radioisotope tracers. The initial cost of the test equipment and the cost to set it up according to the regulations for hermeticity testing are very large [3.6]. This test however is reported to be more accurate and less time consuming than the helium leak test. Many more packages can be tested using this method than the helium leak detection method as this test is done in atmospheric conditions reducing thereby the overall test cost per package [3.7].

3.2.1 Radioisotope usage, disposal and licensing

A documented drawback of the radioisotope fine leak test is associated with the use of a radioactive tracer gas [3.3]. However, Krypton-85 decays by low energy beta and gamma ray emission, both of which are comparatively safe forms of emission [3.6]. The quantities of Krypton-85 required for the test are also so low that the operator is exposed to only a fraction of the US government maximum exposure limits. Nevertheless, industrial users of the radioisotope fine leak test must have a license and operators must be fully trained in handling radioisotopes. The user must also ensure safe disposal of Kr-85 according to the U.S. Nuclear Regulatory Commission guidelines or UK and EU guidelines and licensing. In the UK, the National Radiological Protection Board (NRPB) advises the government on radiation safety, and controls are enforced through Acts of Parliament, regulations and licences.

Another possible limitation is the potential for failures caused by tracer gas interference with small device geometries [3.3] and beta radiation induced soft errors [3.7]. These failures have been disputed by supporters of the test method who state that only devices whose packages failed the radioisotope fine leak test were ever adversely affected by the radioisotope tracer gas.

3.2.2 Volume limitations

This method has been used successfully in industry for high volume applications as detection is easier over a longer period of time than with helium. However, the gas used in the radioisotope fine leak test escapes from a gross leak before it can be measured as in the helium test. For this reason a gross leak test must also be conducted. A radioisotope gross leak test using pressurised liquid instead of gas is also described in the military standards [3.8]. As with the helium leak test there will be a limit on the

cavity volume although lower volume packages can be tested as the test is conducted in atmospheric conditions. No significant surface absorption of Kr-85 is observed in tests involving ceramic packages. A wait time is therefore not necessary to allow tracer gas to desorb from the package material and the time between release from tracer gas pressurisation chamber and measurement can be reduced. The reduction of this wait time means that lower cavity volume packages can be tested. Unfortunately this is not the case for all packaging and fabrication materials. Some groups are working on the method to ensure that the tracer gas stays inside the package to allow gross and fine leaks to be measured. One method uses coconut charcoal as a getter material to hold the tracer gas inside the package for a longer time [3.9]. Methods like this can be useful to characterise package types but these methods are not ideal for 100% end-of-line screening because of the added material which must be incorporated in the package and the length of time required to detect a low leak rate.

3.2.3 *Minimum detectable leak rate*

The minimum detectable leak rate of the radioisotope leak test is 10^{-12} atm.cm^3.s^{-1} [3.6, 3.7, 3.10] due to the counting efficiency of the detection equipment used. This is slightly less than the minimum detectable leak rate of the helium leak test as shown in section 3.1.2 but not sufficiently low for MEMS.

3.3   Limitations of the optical leak test method

The optical leak test method requires calibration to ensure that the deflection of each cap with different material properties and dimensions is known before testing. This method can be complex and time consuming although wafer level testing on hundreds of samples at once can be conducted after calibration of the fine and gross leak test. The method is also capable of distinguishing between a leak rate caused by flow through a leak channel and a permeation leak and could therefore be used to measure permeation leaks into polymer sealed packages. In theory, if used without a tracer gas, this method could detect outgassing throughout device lifetime too although in practise the method is not sensitive enough to measure the typically low pressure increase caused by outgassing.

3.3.1 Minimum detectable leak rate

Generally, the method is able to detect leak rates down to 10^{-10} atm.cm^3.s^{-1} and so the method should not be regarded as a viable replacement for the helium fine leak test for packages with small cavity volume held at high vacuum [3.10, 3.11]. The sensitivity of this test depends not only on the lid material stiffness, thickness and test duration but also on the sensitivity of the optical interferometer used. Making the lid material thinner, generally makes the test method more sensitive and allows for a lower minimum detectable leak rate to be measured but thin caps are not ideal for mechanical protection purposes and so the package would require further packaging levels. Although further packaging need not be hermetic, it must be optically transparent if optical leak detection is to be used to monitor hermeticity at later stages.

3.3.2 Package cap materials and dimensions

The optical fine/gross leak test relies on the package lid being flexible enough to deflect according to pressure difference between the inside and the outside of the package. It is therefore possible to make a package with a thicker cap material with a larger surface area to allow deflection and increase sensitivity. This increase of sensitivity is however to be traded off against the increase in the size of the package needed to allow adequate deflection.

Every package which has to be hermetically tested using the optical leak detection method must be calibrated before use. Different cap materials or thickness of material will change the amount which the cap will deflect due to pressure change. Different cap surface areas and geometries will also influence the pressure deflection properties of a cap. Packages with different cavity volumes with various ambient cavity pressures must also be considered before leak rates are calculated. For example, the cap of a large cavity volume package will deflect by the same amount as that of a low cavity volume package if the cap material and geometry are the same and the pressure inside the cavities is equal. However, the leak rate of the packages will be different due to the different cavity volumes. For this reason the cap deflection technique can detect lower leak rates when the package has a lower cavity volume, particularly when the cavity is shallow and the cap area is large. For this reason the optical leak test may be more

applicable to CMOS fabricated packages than typical MEMS packages which tend to be more three dimensional.

3.4 Limitations of the cumulative helium leak detection method

Another variation of the helium leak test, the cumulative helium leak detection (CHLD), is described in the military standards. This technique requires the device to be either packaged in a helium environment or bombed with the tracer gas. The presence of a cryo-pump in the CHLD test permits the measurement of the helium leaking out during the initialisation step, when the package is placed in the detector chamber which is being pumped down to around 1×10^{-5} atm. It is therefore reportedly possible to measure gross leaks using the CHLD method. Unlike the traditional method, the leak rate is determined from the slope of the helium count which is a function of time.   For this reason it is actually possible to measure the leak rate of the package even if the tracer gas has leaked out and the internal pressure of the package is in equilibrium with the ambient environment [3.12]. The 5 ppm of helium present in ambient air is apparently enough to allow the detection of a gross leak. The maximum detectable leak rate is therefore reported to be up to 1 atm.cm^3.s^{-1} [3.12]. No matter how low the volume of the cavity is, one should always be able to detect the presence of a gross leak in a vacuum or inert gas filled package using the CHLD method although this will not be a quantitative measurement.

3.4.1 Limitations due to the package material

Helium is used as the tracer gas of choice in CHLD although the mass spectrometer can be tuned to another tracer gas. If helium is used, problems will arise with surface sorption in glass, some ceramics and polymers. However, as the helium count is measured over time, it is possible to distinguish between a capillary leak and a leak caused by surface sorption or permeation.   In the case of a capillary leak the measured signal is linear.   A large offset will be seen in the case of a gross leaker. A leak caused by permeation or surface sorption can be identified by an exponential looking curve; the manufacturers of the cumulative helium leak detector refer to these leaks as 'virtual leaks'. The various types of signal typical of the CHLD method are shown in figure 3.7.
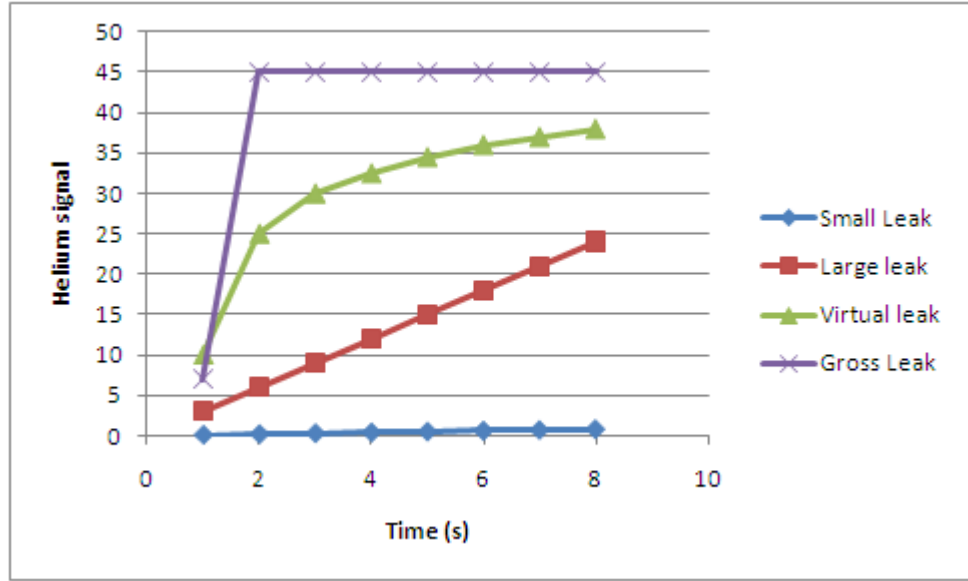
Figure 3.7: Helium signal versus time for molecular capillary leaks, gross leaks and virtual leak [3.12]

Although this method is able to distinguish between leaks caused by permeation and leak channels, it is not possible to quantify the permeation leak as this will be dependent on tracer gas interaction with the permeable material. This cannot be easily mathematically converted to the permeation rate of other gases as is the case for leak rates through capillaries.

3.4.2 Minimum detectable leak rate

This method can detect leak rates as low as 5×10^{-10} atm.cm^3.s^{-1} according to MIL-STD-883H T.M. 1014.13, 3×10^{-13} atm.cm^3.s^{-1} according to MIL-STD-750E T.M. 1071.8 and 4×10^{-14} atm.cm^3.s^{-1} according to the manufacturers [3.8, 3.12, 3.13]. Although the minimum detectable leak rate of this method is up to four orders of magnitude greater than the traditional helium leak method, it is still not stringent enough for many low volume vacuum package applications. The measurement of the minimum leak rate is also unclear as such low calibrated leaks are not commercially available. Some further independent testing and qualification of this method would be beneficial to understand more fully the advantages and limitations of this test method.

3.5 *Residual gas analysis*

Residual gas analysis, RGA, is capable of measuring leak rate down to 10^{-16} atm.cm^3.s^{-1} although this method is extremely expensive and destructive.   RGA is very powerful although it requires thorough knowledge and understanding of leak types and material properties to achieve accurate analysis and results.   Due to this, the lack of equipment availability in Europe, the time taken and energy required to pump the system down before test, this leak detection method is very expensive.   For these reasons, RGA tends only to be used as a failure analysis or research and development tool with regards to hermeticity testing and cannot be considered as an end-of-line test method.

3.6 Summary of the limitations of the existing hermeticity test methods

The most commonly used hermeticity test method, the helium fine leak test, has been examined theoretically to establish the absolute limits of the test method.   The practical considerations of the test have been taken into consideration in this theoretical approach to achieve the most realistic limitations. Literature detailing the advantages and disadvantages of the other hermeticity test methods available in the military standards has been considered to establish the applicability of these methods to low cavity volume microelectronics and MEMS packages. A summary of the limitations of currently available hermeticity test methods is given in table 3.1.

Test Method	Detectable range limitations	Practical limitations	Leak types detected	Suitable package materials	Unsuitable package materials
Helium fine leak	Volume limitation: $> 2.6 \times 10^{-3}$ cm^3 Min. detectable leak rate: 1.28×10^{-10} atm.cm^3.s^{-1}	Increased dwell time required when surface sorption present causing larger volume limit	Leak channels: molecular leaks	Silicon Metals Ceramics	Polymers Glass Epoxies
Radioisotope fine leak	Min. detectable leak rate: 10^{-12} atm.cm^3.s^{-1}	Licensing, handling and disposal of radioisotopes	Leak channels: Molecular and viscous (combinational test)	Silicon Metals Ceramics Glass	Polymers Epoxies
Optical leak detection	Min. detectable leak rate: 10^{-10} atm.cm^3.s^{-1}	Calibration of every package type required	Leak channels Permeation (of tracer gas)	Any material as long as cap thickness and flexibility is appropriate	Rigid cap materials.
Cumulative helium leak detection	Min. detectable leak rate unclear: $10^{-10} - 10^{-14}$ atm.cm^3.s^{-1}	Calibrating system to ensure lowest possible detection limit	Leak channels	Silicon Metals Ceramics	Polymers Glass Epoxies
Residual gas analysis	10^{-16} depending on MS sensitivity	Destructive and very expensive	Leak channels Permeation Outgassing	Any material	n/a

Table 3.1: Traditional test method limitations

3.7 Hermeticity testing required by industry

By surveying the different leak test methods available for use in industry and academia it is clear that these test methods are not always suitable for application to low cavity volume microelectronics and MEMS packages. The practicalities of the methods lead to further limitations which mean some package types cannot be accurately hermetically tested according to the military standards. Table 3.1 outlines these limitations and highlights the package types for which traditional leak detection techniques do not apply. This section aims to show that further test methods are required by industry and academia by means of a literature review.

A market survey was also conducted to assess whether or not industry are currently developing packages which traditional hermeticity test methods cannot accurately

assess and if this is a future concern. This market survey was conducted to determine the feasibility of the project from the perspective of the sponsoring company, MCS Ltd. Before the project was accepted, the company required to know whether hermeticity testing was important to industry, if the current test limitations were well-known and if manufacturers were willing to sub-contract the hermeticity testing work. The hermeticity testing market survey is available in Appendix C and the results of this survey are summarised in section 3.7.2.

3.7.1 Literature review

The limitations of the existing hermeticity test methods have been well documented in the literature. Sinnadurai shows, for example, that the minimum detectable leak rate of the traditional helium leak test is not low enough to ensure less than 5000 ppm ingress of moisture into a typical package [3.14]. Other research groups aiming to find packaging solutions for newly developed sensitive devices requiring ultra high vacuum cavities have also documented the inadequacy of the available hermeticity test methods in terms of minimum detectable leak rate for their applications [3.15, 3.16]. Some researchers reporting new detection methods have also highlighted the need for a lower detection limit [3.17]. Moraja and Amiotti explain this limitation by showing that a typical package with a leak rate equal to the minimum detection limit of traditional hermeticity test methods has a short lifetime. This paper explains how getters can be used to solve this problem [3.18]. Several papers have highlighted the minimum detectable leak rate limitation of the traditional leak test methods and have shown the requirement for leak rates of the order of 10^{-15}-10^{-16} atm.cm^3.s^{-1} for many applications [3.10, 3.14, 3.15, 3.16, 3.17, 3.19, 3.20]. In industry the traditional tests are conducted on packages with volumes below the minimum stated in section 3.1.1 as the military standards state that they can be used on packages with volumes below 0.01cm^3. Unfortunately, many manufacturers are required by the end users of their products to meet military standards so these tests are followed blindly to meet specification. As seen earlier in this chapter, the limitations of the test methods and the conditions set-out by the military standards mean that many packages will falsely pass the traditional leak tests.

Before the addition of the optical leak detection method to the military standards, many researchers explained the requirements of industry to find a test method capable of

covering the full leak range [3.11, 3.21]. As explained in section 3.1.1, a volume limitation is apparent due to a gap in the detectable leak range of the fine and gross leak test methods. Jourdain et al. and De Wolf et al. explained the use of the through hole helium leak detection method to eliminate this gap [3.3, 3.21]. This test method is useful for package prototyping but is destructive and the minimum detectable leak rate is not as low as that of the traditional helium leak test. Nese et al. and Veyrié et al. also present Fourier transform infra-red spectroscopy, FTIR, using a tracer gas as a method which covers the gap in the detectable range [3.22, 3.23]. More details of this test method can be found in Chapter 4 of this thesis. All authors highlight in their papers the requirement in industry for a new hermeticity test method capable of detecting the full leak range of low cavity volume packages.

There are many papers in literature describing the use of the traditional leak test methods to characterise the hermeticity of new packaging materials. As discussed in section 3.1.3, any porous materials cannot be accurately tested using these methods although, often due to a lack in alternatives, researchers are forced to use the tests. Many have adopted the through-hole helium leak test as an alternative since at least this test method only detects helium which has passed through the package seal or walls into the cavity and not helium which has been absorbed into package wall materials [3.19, 3.24]. This test method however is not ideal for this purpose and other researchers have proposed the use of FTIR and evaluation by gas diffusion to solve this testing issue [3.23, 3.25]. The concern in industry is that testing these packages to military standards using traditional methods will produce false negative results whereby packages which are in fact hermetic enough for the application are rejected.

As with all test methods, it is understood that industry requires a quick, inexpensive, non-destructive, 100% hermeticity screening method that is able to cover the full leak range down to and below that required for the most stringent applications. The test must also be repeatable, reliable, applicable to a range of packaging materials and simple to conduct.

3.7.2 Market survey results

These requirements are by no means easy to meet, so, before this project was undertaken it was necessary to conduct a market survey to establish which test criteria

were most important to industry. Engineering Doctorate students are required to work closely with industrial sponsors and the work conducted should be industrially relevant. To ensure this project followed this fundamental guideline, the market survey described here was necessary. The results are discussed in this thesis to highlight the importance of the subject matter in the MEMS community in the UK and Europe. The main purpose of this market survey was to establish how manufacturers of MEMS and small cavity microelectronic products test the hermeticity of their packages. We also wanted to find out if they were aware of the traditional test methods limitations and if they manufactured products that are affected by these limitations. It was also important to know whether or not these companies would consider using an external contractor to test their products. From the response of the market survey participants, MCS Ltd could gauge the size of potential market for hermeticity testing of low cavity volume packages allowing a sound business decision regarding whether or not the project was viable.

The market survey, which can be found in Appendix C, was produced in October 2007 and the results were compiled five months later in March 2008. Using MISEC's updated small and medium enterprise (SME) contacts list, 21 relevant companies were successfully emailed regarding the hermeticity testing market survey. After follow up calls, three completed surveys (Qinetiq, GE Aviation and Raytheon) were received and two telephone surveys were conducted. Amphotonix and CST use a packaging contractor (Optocap) or their customers test their own packages. Optocap were contacted on several occasions but a completed survey was never received. The market survey therefore had a 16% response rate which exceeds the average 10% expected. Interest in the survey and project were also expressed by two companies who were not manufacturing packages at the time the survey was conducted but intended to in the near future (Semefab and Wolfson Microelectronics).

A small description and a link to the market survey were published in the January edition of the Patent DfMM Newsletter and correspondence from Fraunhofer ISIT was received. They have developed the Neon-Ultra Fine Leak test for wafer level hermeticity testing measuring leaks as small as 1×10^{-14} atm.cm^3.s^{-1}. This test method involves measuring the Q-factor of devices before and after neon gas bombing and is therefore applicable only to resonating devices. This test method will be further discussed in Chapter 5. Fraunhofer ISIT expressed interest in the project. Another survey questionnaire was returned from Selmic, a Finnish company who specialise in

manufacturing microelectronics and micromodules. They use advanced packaging techniques and were keen to understand the limits of helium testing for small package volumes. Interest was also expressed by GE Industrial Sensing who are involved in advanced measurements and sensor-based technology.

The results from the survey are shown in table 3.2:

Survey question	Answers
Do you manufacture products with or work with cavity volumes less than 10mm³?	Only GE Aviation and Selmic currently work with package cavity volumes less than 10mm³ but the others anticipate working with volumes this small in the foreseeable future.
Do you test the products in-house?	GE Aviation test 50% and Fraunhofer ISIT and Raytheon test 100% of their products in-house. QinetiQ test 100% of their products but some are tested in house using the Q-factor techniques and the others are fine leak tested at GE Aviation. Selmic do all their testing in-house and perform hermeticity tests on 2% of their packages.
Would you be interested in knowing the leak rate of the packages?	All companied were interested in knowing the leak rate of devices.
Is the minimum detectable leak rate of the order of $6x10^{-18}$ atm.cm³.s⁻¹?	Only Qinetiq could say their test measures below $6x10^{-18}$ atm.cm³.s⁻¹.
Do you use the Helium Fine Leak Test? Do you follow MIL-STD-883 Method 1014?	All companies who use the helium leak test and follow the MIL-STD-883 Method 1014 with Raytheon also using BS9400 Met 1.2.6.14.1 if the tests were contractual. Frauhofer ISIT use Neon and Q-factor monitoring.
What pressure and dwell time do you use?	GE Aviation: Pressure = 2bar, Dwell = 1 hour Raytheon: Pressure = 30psig (seam seal) and 45psig (epoxy seal), Dwell = 2-4 hours (seam seal) and 5 hrs 20min (epoxy seal) Qinetiq: Unsure as fine leak testing conducted at GE Aviation Fraunhofer ISIT (Neon): Pressure = 3bar, Dwell = 12hrs Selmic: No values given
Are you aware of the helium leak test's limitations with respect to cavities of volumes less than 10mm³?	Qinetiq, Fraunhofer ISIT and GE Aviation were aware of the problems but Raytheon and Selmic were not.
Would you like to receive more information about the limitations?	All companies would apart from Fraunhofer ISIT.

Survey question	Answers
Would you be interested in a method applicable to MEMS, optoelectronics and advanced microelectronics?	All companies are interested.
Would you be interested in further information regarding failure analysis and reliability of MEMS?	All companies would like further information.
What industry publications do you read?	MNT News, Advanced Packaging, Surface Mount Technology, Solid State Technology Microelectronics, Semiconductor, Electronics, Compound Semiconductor, NPL newsletter, CALCE newsletter, IEEE Journals
What trade shows do you attend?	Productronica, Laser, Hannover Messe, Sensor, SMT Hybrid, Electronica

Table 3.2: Market survey results

From the above collation of results it was concluded that low cavity volume packages are currently being manufactured and industry predicts that cavity volumes are likely to drop further in the near future. Leak detection is essential in industry with 80% of participants using the helium fine leak test to check the hermeticity of their packages. Half of these companies were unaware of the limitations of the helium leak test. From this survey it was concluded that there was significant interest in hermeticity testing and substantial evidence to prove that existing methods were being incorrectly used to test new generation packages. For these reasons, MCS Ltd decided to continue with the project. It was decided a white paper explaining the limits of the traditional test methods should be written and made available on the MCS Ltd website. This white paper can be found in Appendix D.

3.8   Conclusions

A novel expression has been derived in this chapter which allows the applicability of the helium leak test method to measure the leak rate of low cavity volume packages depending on the specific test parameters used. The helium leak test method is proven to be effective when used in conjunction with a suitable gross leak test to measure the leak rate of packages with a cavity volume greater than 2.6 mm^3 when a dwell time of 3

minutes is used and greater than 0.052 cm^3 when a dwell time of one hour is required. Given these volume limitations, the minimum leak rate which can be measured using helium leak detection is 1.28×10^{-10} atm.cm^3.s^{-1}. These expressions can be used to establish whether or not the helium leak test method is appropriate for the package type concerned. With typical MEMS cavity volumes of less than 1mm^3 and vacuum packaged MEMS requiring leak rates below 10^{-16} atm.cm^3.s^{-1} it is clear that the helium leak test is not suitable for many MEMS applications and another test technique is required.

This chapter has also summarised the advantages and limitations of the other fine leak test methods described in the standards. No test technique is currently able to meet the hermeticity requirements of typical MEMS and so new test techniques are required. A market survey is presented in this chapter which shows that not all manufacturers of MEMS are aware of the helium leak test limitations. All companies who took part in survey were interested in new hermeticity testing techniques, making this project of interest to MCS Ltd.

3.9 References

[3.1] D.A. Howl and C.A. Mann, '*The Back-Pressurization Technique of Leak Testing*', Vacuum, vol.15, pp. 347-352, 1965.

[3.2] R.M. Corless, G.H. Gonnet, D.E.G. Hare, D.J. Jeffrey and D.E. Knuth, '*On the Lambert W function*' Advanced Computational Mathematics, 5, pp 329-359, 1996.

[3.3] I. De Wolf, A. Jourdain, P. De Moor, H.A.C. Tilmans and L. March and, '*Hermeticity Testing and Failure analysis of MEMS Packages*', 14th International Symposium on the Physical and Failure Analysis of Integrated Circuits, pp. 147-154, 2007.

[3.4] K. Schjølberg-Henriksen, E. Poppe, S. Moe, P. Storås, M.M.V. Taklo, D.T. Wang and H. Jakobsen, '*Anodic bonding of glass to aluminium*', Microsystems Technology, 12, pp. 441-449, 2006.

[3.5] A. Goswami and B. Han, '*On ultra-fine leak detection of hermetic wafer level packages*' IEEE transactions of Advanced Packaging, 31(1), pp. 14-21, 2008.

[3.6] G. Neff and J. Neff, '*Leak testing electronics devices in production quantities*', IsoVac Engineering, 1986.

[3.7]   M. L. Minges, *'Electronic Material Handbook: Packaging'*, Volume 1, ASM International Handbook, 1989, pp. 930.

[3.8]   MIL-STD-883H T.M. 1014.13, *'Seal'*, United States of America Department of Defence, Test method standards, Microcircuits, pp. 81-99, 2010.

[3.9]   K. Rink, *'Fundamental considerations concerning the detection of gross leaks in bridge-wire initiators'*, Int. J. Vehicle Safety, 1(4), pp 253-266, 2006.

[3.10] W. Reinert, *'Solutions addressing deficiencies in evaluating hermeticity of MEMS packages and in predicting product lifetimes'*, Hermetic MEMS Packaging Workshop, San Francisco, 2009.

[3.11] G. Elger, L. Shiv, N. Kikac, F. Muller, R. Liebe, M. Grigat, and M. Heschel, *'Optical leak detection for wafer level hermeticity testing',* IEEE Semiconductor International Electronics Manufacturing Technology Symposium, 2004.

[3.12] J. Pernicka, *'The cumulative helium leak detector'*, Pernicka Corporation, 2005.

[3.13] MIL-STD-750E T.M.1071.8, *'Hermetic seal'*, United States of America Department of Defence, Test Method Standard, Test Methods for Semiconductor Devices, pp. 100-116, 2006.

[3.14] N. Sinnadurai, *'Plastic packages survive where hermetic packages fail'*, Microelectronics Reliability, 36 (7/8), pp 1001-1018, 1996.

[3.15] K. Birkelund, P. Gravesen, S. Shiryaev, P. Rasmussen and M. Rasmussen, *'High pressure silicon sensor with low cost packaging'*, Sensors and Actuators A, 92, pp. 16-22, 2001.

[3.16] P.J. van der Wel, J. Stulemeijer, J.A. Bielen, T.A. den Dekker, M.A.J. van der Gils and R.J. Havens, *'Hermeticity testing of capacitive RF MEMS switches'*, IEEE 46th Annual International Reliability Pysics Symposium, Phoenix, pp. 691-92, 2008.

[3.17] F. Gueissaz, *'Ultra low leak detection method for MEMS devices'*, 18th IEEE International Conference on MEMS, Miami Beach, Florida, USA, 2005.

[3.18] M. Moraja and M. Amiotti, *'Getters films at wafer level for wafer bonded MEMS'*, Proceedings of Design, Test, Integration and Packaging, DTIP, Cannes-Mandelieu, pp. 346-349, 2003.

[3.19] A. Jourdain, P. De Moor, S. Pamidighantam and H.A.C. Tilmans, *'Investigation of the hermeticity of BCB-sealed cavities for housing (RF-)MEMS devices'*, IEEE International Conference, Las Vegas, USA, 2002.

[3.20] Y. Tao and A.P. Malshe, *'Theoretical investigation on hermeticity testing of MEMS packages based on MIL-STD-883E'*, Microelectronics Reliability, 45, pp. 559-566, 2005.

[3.21] J. Newman and S. Thayler, '*Optical leak testing of Hermetic Semiconductor, MEMS and optoelectronics devices*', Norcom Systems Inc, 2002.

[3.22] M. Nese, R.W. Bernstein, I.R. Johansen and R Spooran, *'New method for testing hermeticity of silicon sensor structures'*, Sensors and Actuators A, 53, pp. 349-352, 1996.

[3.23] D. Veyrié, D. Lellouchi, J.L. Roux, F. Pressecq, A. Tetelin and C. Pellet, '*FTIR spectroscopy for the hermeticity assessment of micro-cavities*', Microelectronics Reliability, 45(9-11), pp. 1764-1769, 2005.

[3.24] F. Bardin, S. Kloss, C. Wang, A.J. Moore, A. Jourdain, I. De Wolf and D.P. Hand, '*Laser Bonding of glass to silicon using polymer for microsystems packaging*', Journal of Microelectromechanical Systems, 16(3), pp. 571-580, 2007.

[3.25] C. Jang, A. Goswami and B. Han, '*Hermeticity evaluation of polymer-sealed MEMS packages by gas diffusion analysis'*, Journal of Microelectromechanical Systems, 18(3), pp. 557-587, 2009.

Chapter 4

Fourier Transform Infra-red Spectroscopy and Raman spectroscopy techniques

4.1   FTIR spectroscopy

Fourier Transform Infra-red Spectroscopy, FTIR, is an optical technique used to determine the molecular composition of a sample from its infra-red absorption or transmission spectrum.   In FTIR spectroscopy, a beam of light containing many different frequencies is shone firstly through a modified Michelson interferometer and then into the sample [4.1].   In the Michelson interferometer the broadband light from the source is passed through a collimator onto a beam splitter where 50% of the light is reflected onto the fixed mirror and 50% is transmitted onto the moving mirror.   The light is reflected back to the beam splitter and 50% of the light reflected from each mirror passes into the sample compartment as shown in figure 4.1.
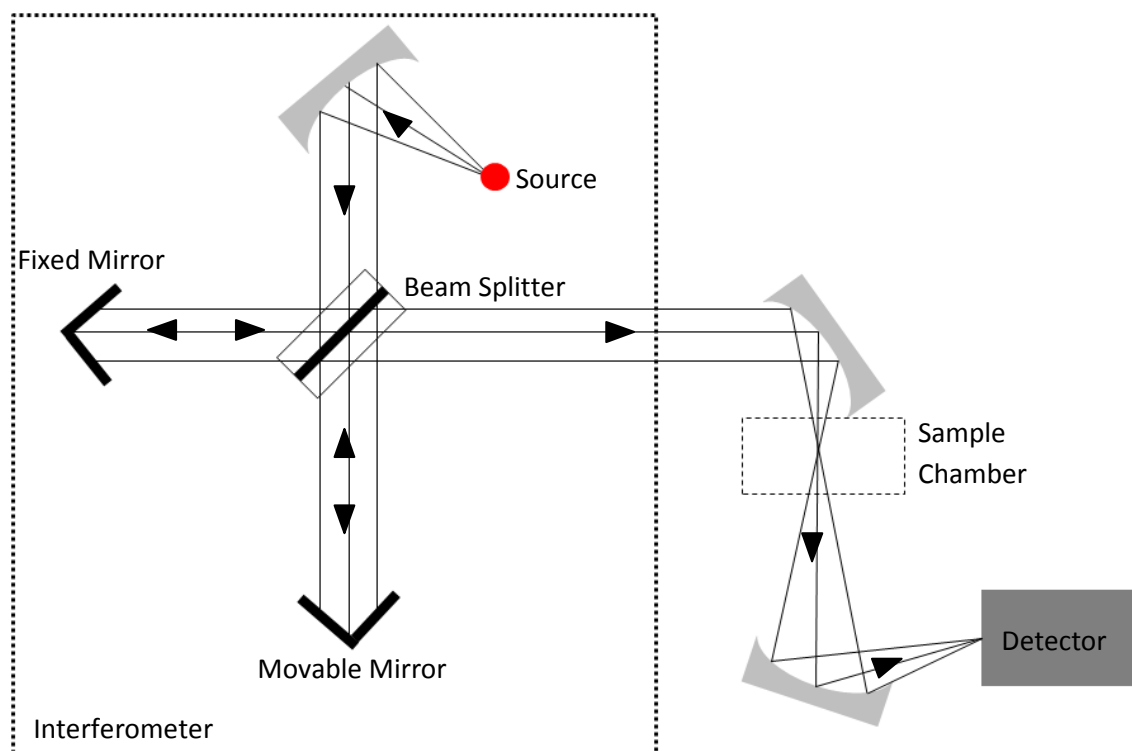
Figure 4.1:   Schematic of the adapted Michelson interferometer for FTIR.

The difference in the path length of the light coming from the fixed mirror and the moving mirror is dependent on the position of the moving mirror. Some wavelengths will experience constructive interference as a result and will pass into the sample compartment whereas other wavelengths will be blocked by destructive interference. In such a configuration only a selected set of wavelengths can pass into the sample compartment. By moving the mirror, a second set of wavelengths pass through the sample to the detector and a collection of data points are obtained. The resultant interferogram shows the amount of light absorbed or transmitted as a function of the movable position of the mirror. The Fast Fourier Transform of the data collected gives the results in a more desirable form such as percentage of light being absorbed or percentage of transmission for each wavelength.

The resultant FTIR spectrum can be compared to known results allowing thereby the determination of the chemical composition of the sample under examination.

4.1.1 *Application to hermeticity*

The application of the FTIR method for the determination of hermeticity in low cavity volume packages requires the bombing of samples in an appropriate tracer gas for several hours depending on the minimum leak rate, which is required to be detected. To obtain a background spectrum before test, the sample is firstly analysed using the FTIR spectrometer before being bombed in a tracer gas. After bombing, the package is transferred as quickly as possible to the spectrometer where the amount of tracer gas held within the package cavity will be measured using the FTIR spectrometer in transmission mode. This is in contrast to the helium leak test whereby the tracer gas leaking out of the package is measured. Since only the tracer gas left within the package is measured using FTIR, the results will not be effected by sorption of tracer gas in material layers since only tracer gas which has leaked into the cavity will be measured. The FTIR measurement is taken in ambient conditions unlike the helium leak test where the sample chamber must be pumped down to a vacuum before the measurement is recorded. Therefore, the amount of tracer gas lost during the dwell time will be reduced and so the minimum cavity volume package which can be accurately hermeticity tested using the FTIR method should be lower than is the case using the helium leak test.

The FTIR spectrum obtained shows an absorption peak, which is characteristic of the tracer gas used. Once the initial background spectrum has been removed, the quantity of gas held within the cavity can be calculated using the Beer Lambert Law, equation 4.1.

$$-\log(transmission) = \frac{lA}{RT} P_p \qquad (4.1)$$

where l is the depth of the cavity, A is the molar absorption coefficient of the tracer gas, R is the universal gas constant, T is the temperature and P_p is the partial pressure of the tracer gas.

Assuming only molecular flow through a capillary and knowing the bombing time and pressure, the leak rate of the package can be determined using the Howl-Mann equation, introduced initially in Chapter 2 and reproduced for convenience in equation 4.2

$$R = \frac{LP_b}{P_0}\left(\frac{M_A}{M}\right)^{1/2}\left(1 - \exp^{\frac{-Lt_b\left(\frac{M_A}{M}\right)^{1/2}}{VP_0}}\right)\exp^{\frac{-Lt_d\left(\frac{M_A}{M}\right)^{1/2}}{VP_0}} \qquad (4.2)$$

Where R is the *measured* leak rate in atm.cm^3.s^{-1} helium, L is the *equivalent standard* leak rate in atm.cm^3.s^{-1} air, P_b is the bomb pressure in atm, P_0 is the atmospheric pressure in atm, M_A is the molecular weight of air in grams (28.7g), M is the molecular weight of tracer gas in grams, t_b is the bomb time in seconds, V is the package cavity volume in cm^3 and t_d is the dwell time in seconds. The distinction between the *measured* and *equivalent standard* leak rates was made in Chapter 2 with reference to the helium fine leak test. For clarity, the *equivalent standard* leak rate is the leak rate of a package with a *measured* leak rate, R, under standard conditions, i.e. dry air at 25°C leaking into a package with a high pressure side at 1 atm and a low pressure side no greater than 1 mmHg or 1.3158×10^{-3} atm. The measured partial pressure, P_p, can be used to find the measured leak rate, R, using equation 4.3.

$$R = \frac{P_p P_0 V}{P_b t_b} \qquad (4.3)$$

The dwell time is equal to the time elapsed since the bombing cycle was completed and the standard equivalent leak rate can then be calculated using the Howl-Mann equation, equation 4.2. For confirmation, a second FTIR spectrum can be obtained after several minutes and the new transmission rate used to calculate the partial pressure, P_p, of tracer gas left inside the cavity, R and L are then recalculated using equations 4.3 and 4.2, respectively.

Fourier Transform Infra-red spectroscopy was first used to measure the hermeticity of silicon sensor structure by researchers at SINTEF, Norway, and a paper detailing the test method was published in 1995 [4.2]. In their paper, Nese et al. explained that the minimum detectable leak rate of the helium leak detection method was not low enough to ensure their sensor package would remain hermetic over the device lifetime. They proposed using FTIR spectroscopy with a nitrous oxide tracer gas as the absorption peak of such a gas lies within the range of wavelengths at which the silicon package is transparent. N_2O is also non-toxic and has a particle size comparable to that of nitrogen and air. Nese et al. characterised the method by using commercially available gas sensors to control the N_2O and N_2 seeding gas atmosphere in which the packages were epoxy sealed. The paper reported that, due to internal reflection issues, the internal cavity pressure detection limit for the FTIR method was 1 mbar [4.2].

The FTIR method can be up to 3 orders of magnitude more sensitive, i.e. the minimum detectable leak rate is up to 3 orders of magnitude lower, than the traditional helium leak test method. This corresponds to a minimum detectable leak rate of the order 10^{-13} atm.cm^3.s^{-1}. Using FTIR, the minimum detectable leak rate is dependant only on the experimental parameters as the tracer gas accumulated inside the packages is measured. By increasing the bomb time or pressure, the method is therefore more sensitive. Minimising the internal reflection within the cavity can also improve the sensitivity and result in a lower detection limit [4.2].

This work was continued by Veyrié et al. from the University of Bordeaux who used the FTIR method to assess the hermeticity of Benzo-Cyclo-Butene (BCB) sealed silicon packages [4.3]. Veyrié et al. used the Beer-Lambert Law to determine the partial pressure of the N_2O tracer gas within the package after the sample has been bombed.

The Howl-Mann equation was used to determine the leak rate of the package and converted to an equivalent standard leak rate.

4.1.2 *Theoretical limitations*

In Chapter 2, section 2.4, the mathematics of the different leak types possible in a microelectronic or MEMS package was described. It was explained that a leak rate caused by permeation through packaging materials is significantly different to one caused by molecular flow through a capillary leak. Therefore it is not possible to determine an equivalent air or water leak rate of a polymer sealed package from a measured N_2O leak rate caused by permeation through packaging materials measured using FTIR. The determination of the *measured* leak rate of a permeable package is accurate however with the FTIR method, unlike the helium leak test method. What is measured is the tracer gas which has leaked into the cavity and not the gas leaking out, as is the case with the helium leak test method. In other words, the FTIR method is not affected by false negative readings due to surface sorption. This test can therefore be used to assess the hermeticity of polymer sealed packages but conversion of the nitrous oxide measured leak rate to an air or water equivalent leak rate is complex and is, as yet, not possible. For a particular package, it is possible to calibrate the FTIR hermeticity test method using pressure and humidity sensors within the package to assess the air or water leak rate, which corresponds to the measured N_2O leak rate. As permeation rates depend not only on the size of the permeating molecule and spaces between the molecules of the polymer material but on also the chemical affinity between the gas molecules and the polymer, recalibration of the system will be necessary if a change in the package geometry or in the material is made.

FTIR can be used successfully to determine the *equivalent standard* leak rate of packages containing silicon or glass when the leak is caused by molecular flow through a capillary leak or crack. Nitrous oxide, being a larger molecule, cannot diffuse through glass like helium, hydrogen or neon. Any nitrous oxide measured inside the cavity will therefore be due to micro-cracks in the package material or seal. These can be approximated to one capillary and assuming a molecular flow, Graham's Law is valid and the Howl-Mann equation can be used to calculate the equivalent standard leak rate of any gas from the N_2O measured leak rate.

The minimum detectable leak rate of the FTIR hermeticity test method depends on the parameters of the test, in particular the bomb time and pressure [4.2]. This is true also of the radioisotope test method as with both of these tests, the tracer gas inside the package cavity is measured and not the gas leaking out. Unlike the helium leak detection method, the minimum detectable leak rate of both these methods is not limited by the sensitivity of the detector used [4.2]. However, the bombing pressure and time cannot be increased indefinitely and so the FTIR method will have a limit for general industrial applications. The main advantage of the FTIR method over the radioisotope leak detection method is that the tracer gas is non-toxic and no special licenses are required for handling and disposal.

The minimum detectable *measured* leak rate, R_{min}, is given by:

$$R_{\min} = \frac{P_{p\min} P_0 V}{P_b t_b}$$

(4.4)

where P_{pmin} is the minimum partial pressure detectable using the FTIR spectrometer, P_0 is the ambient pressure, 1 atm, V is the cavity volume of the package, P_b is the bombing pressure and t_b is the bombing time. The minimum *measured* detectable leak rate of the FTIR method is 9.139×10^{-12} atm.cm^3.s^{-1} N$_2$O when the minimum measurable change in partial pressure is assumed to be equal to that achieved by Nese et al., 1 mbar (9.87×10^{-4} atm), $P_0 = 1$ atm, $V = 1 \times 10^{-3}$ cm^3, $P_b = 5$ atm and $t_b = 6$ hours.

As the Howl-Mann equation is used to convert the *measured* FTIR leak rate to the *equivalent standard* leak rate, two leak rates are possible from any one measured leak rate and so a gross leak test is required as with the helium leak detection method. As the cavity volume of the sample being tested is reduced so too is the minimum detectable leak rate and the upper possible equivalent standard leak rate. When testing low cavity volume packages, it is possible that the upper leak rate drops below the minimum detectable leak rate of the gross leak test method and so a gap in the detectable range develops just as is the case when the helium leak test method is used. This gap stems from the finite dwell time necessary to transfer the package from the bomb chamber to the FTIR system for detection. The advantage the FTIR hermeticity testing method over the helium leak test method is that spectra can be collected quickly in atmospheric conditions. Since it is not necessary to pump the external environment

down to a vacuum and the tracer gas left inside the package cavity is quantified, the FTIR method has a lower volume limitation. If molecular flow through a capillary leak is assumed to be the only leak type present in the package under test, the minimum acceptable volume for accurate FTIR hermeticity testing can be calculated. The same equation used for the helium leak test volume limitation calculation, equation 3.7, reproduced here and amended to reflect FTIR hermeticity testing, equation 4.5, can be used.

$$L_{upper} = \frac{-\left[\ln z - \ln \ln z\right] VP_0}{t_d \left(\dfrac{M_A}{M_{N_2O}}\right)^{1/2}} \qquad (4.5)$$

where $z = Rt_d/VP_b$ is described in Chapter 3. In the case of FTIR hermeticity testing, R is not however the minimum detectable leak rate given by the sensitivity of the measurement equipment. R is replaced by R_{min}, equation 4.4, which is the minimum detectable leak rate of the FTIR test given by the experimental parameters, such that:

$$z = \frac{R_{min} t_d}{VP_b} = \frac{P_{pmin} P_0 t_d}{P_b^2 t_b} \qquad (4.6)$$

with P_{pmin}, V, P_0 and t_d as previously defined; M_A is the molecular weight of air and M_{N_2O} is the molecular weight of the nitrous oxide tracer gas. Using equation 4.5, the minimum cavity volume of package for which FTIR testing can be calculated over the full leak rate range if a gross leak rate test is used subsequently. Figure 4.2 shows the results of this calculation when the parameters are kept consistent with typical values used in the calculation of the helium leak test method. The bomb time, t_b, is 6 hours, the bomb pressure, P_b, is 5 atm and the dwell times, t_b, used are three minutes and one hour. The only change in the input parameters is the minimum detectable leak rate, R, in the case of helium leak testing and R_{min} in the case of FTIR leak testing. In helium leak testing R is fixed by the limits of the mass spectrometer, in FTIR, the leak testing R_{min} is dependent on the input parameters. In figure 4.2 the input parameters to calculate R_{min}, shown in equation 4.3, are P_{pmin} = 1 mbar (9.87x10^-4 atm), P_0 = 1atm, P_b = 5atm, t_b=6 hours. In the case of FTIR testing, the minimum detectable leak rate reduces as the cavity volume of the packages decreases. Assuming a dwell time of 3

minutes, figure 4.2 shows that, the minimum cavity volume for which the FTIR leak test is valid is 7.36×10^{-4} cm^3 compared to 2.6×10^{-3} cm^3 for the helium leak test. This minimum value can be further lowered by changing the input parameters or by improving the signal to noise ratio resulting from internal reflections within the package being tested [4.2]. Lowering this parameter lowers the minimum cavity volume of package whose leak rate can be determined by the FTIR leak test used in conjunction with a suitable gross test, without the development of a gap in the detectable range. Increasing the bomb pressure and bomb time will have the same effect.
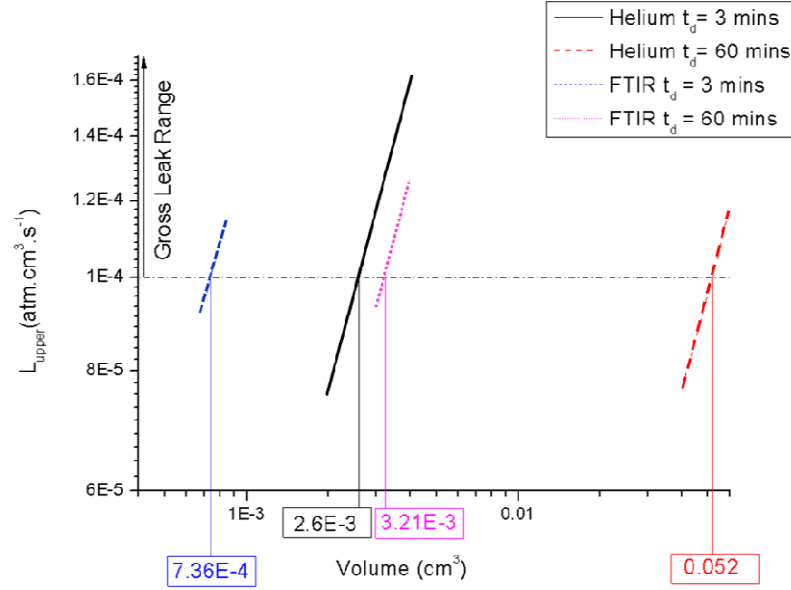
Figure 4.2: L_{upper} as a function of volume for $P_{pmin}=9.87 \times 10^{-4}$ atm, $P_b=5$ atm, $t_b= 6$ hours. For comparison, L_{upper} for the fine helium leak test is indicated.

The *equivalent standard* minimum detectable leak rate is calculated using the approximation described in chapter 3 in equation 3.9, reproduced here and amended to reflect FTIR hermeticity testing, equation 4.7.

$$L_{lower} = P_0 \sqrt{\frac{R_{min}V}{P_b t_b}} \left(\frac{M_{N_2O}}{M_A} \right)^{1/2} \qquad (4.7)$$

Substituting equation 4.4 into 4.7 gives:

$$L_{lower} = P_0 \sqrt{\frac{P_{pmin}V^2 P_0}{P_b^2 t_b^2}} \left(\frac{M_{N_2O}}{M_A} \right)^{1/2} \qquad (4.8)$$

95

Equation 4.8 shows that L_{lower} is reduced when the P_b and t_b are increased.

4.1.3 Practical considerations

As with the helium leak test, the input parameters of the FTIR leak test method cannot be increased or decreased indefinitely to decrease the minimum measureable cavity volume or reduce the minimum detectable leak rate, respectively. Practically, reducing the dwell time much below 3 minutes is challenging although it is not necessary to draw a vacuum in a chamber to test using FTIR as is the case for helium leak detection. For special cases it may be possible to reduce the dwell time to around 60 seconds and decrease therefore the minimum volume for which the FTIR leak test is valid to 2.46×10^{-4} cm^3 assuming the other test parameters are equivalent to those used to produce figure 4.2. This however would not be a viable method of test in industry where all packages must be hermeticity tested and batch testing is preferred. Conducting the FTIR test method with a dwell time of only a minute would mean that packages would have to be bombed individually resulting in inefficient testing.

Decreasing the cavity volume of the package being tested and the minimum partial pressure, which can be detected using the FTIR spectrometer, would reduce the minimum detectable leak rate. The minimum detectable partial pressure of nitrous oxide which can be detected is dependent on; (a) the package dimensions; (b) the internal layers present responsible for internal reflections which reduce the sensitivity of the detection method; (c) the transparency of the package material to the probing light and; (d) the specifications of the spectrometer used.

As with the helium leak test method, the bomb time cannot be increased indefinitely as 'one-way leaks' will be introduced by the stress induced on the packaging while exposed to such high pressures. Although with the FTIR method it is possible to observe when a 'one-way leak' has occurred, the test is not effective when they are present. A 'one-way leak' can be detected when the tracer gas is measured in the package cavity after exposure but the intensity of the transmission peak corresponding to the tracer gas partial pressure does not decrease with time. This means that a leak path has been created under the high pressure conditions of the bombing cycle which has closed afterwards. "One way" leaks are avoided in the helium leak test by keeping

the bomb pressure below 5 atm. As the bombing cycle of the FTIR test method is equivalent to the helium leak test method, the maximum bomb pressure used in the following calculations will be 5 atm. Assuming the detectable partial pressure limit found by Nese et al, 9.87×10^{-4} atm, and taking the minimum cavity volume when a dwell time of three minutes is used, 7.36×10^{-4} cm^3 and a bomb pressure of 5 atm, figure 4.3 shows the effect of increasing the bomb time on the equivalent minimum detectable leak rate of the FTIR method. Figure 4.3 shows that increasing the bomb time beyond 12 hours has a minimal effect in lowering the minimum *equivalent standard* leak rate.
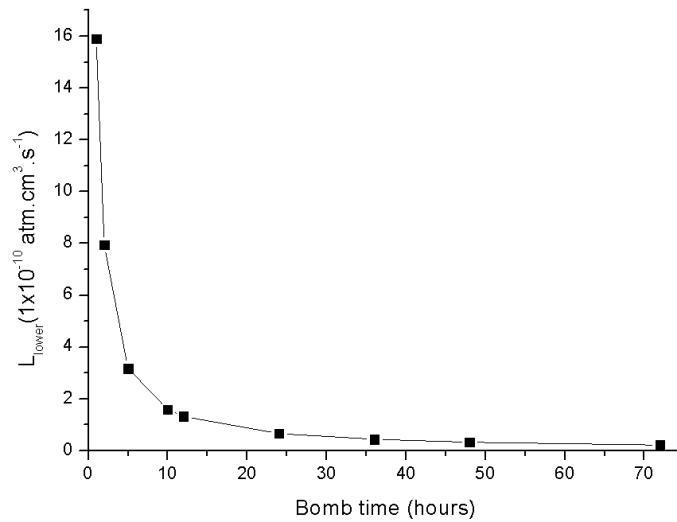
Figure 4.3: L_{lower} as a function of the bomb time for $P_{pmin}=9.87\times10^{-4}$ atm, $P_b=5.103$ atm and $V=7.36\times10^{-4}$ cm^3

This FTIR method is only valid when the leak type being measured is molecular; packages containing permeable materials cannot therefore be tested accurately in this way using the FTIR test method. However, qualitative tests can be performed on permeable materials since the pressure of gas inside the cavity is measured. No matter whether a qualitative test is sufficient or the leak is molecular and the Howl-Mann equation is applicable, the package material must be transparent to the wavelength of the probing light.

The absorption peak of nitrous oxide tracer gas is suitable for use with infra-red light, which is transparent to silicon. The FTIR spectrometer may be used in both transmission and reflectance modes. In transmission mode, both the top cap and the lower substrate must be transparent to the probing light. If a suitably reflective surface is available within the package, reflectance mode can be used, however, highly

reflective materials in the infra-red are not commonly found in MEMS and microelectronic packages. It is also possible to use a probing light with an alternative wavelength to allow transmission through a particular package although a tracer gas with a suitable absorption peak must be identified.

In the case of FTIR leak testing using infrared light and nitrous oxide tracer gas, it may not be possible to measure the leak rate of Micro-Opto-Electo-Mechanical Systems (MOEMS) depending on the size and type of glass used to create an optical window. Many types of glass are strong infrared absorbers and hence the probing light cannot be transmitted through the optical window. This may also be the case for metal and ceramic packages.

The test packages used in experiments conducted at the sponsor Company, MCS Ltd, have a silicon substrate and cap and were fabricated by Mr. Norbert Lorenz and Mr. Martin Smith, of Prof. Duncan Hand's Applied Optics and Photonics group at Heriot-Watt University, figure 4.4. The samples comprised of a triple stack layer of silicon with the centre layer containing a 5 mm diameter hole to create a cavity. The lower and upper silicon layers were bonded to the centre layer with BCB using a direct laser bonding method to minimise heating effects in the centre of the package where the microsystem is most often located [4.4]. The volume of the packages is 9.82×10^{-3} cm^3 and the packages were bombed for 24 hours. The FTIR spectrometer used is a Thermo Nicolet IN10 FT-IR, figure 4.5.

(a)   *(b)*
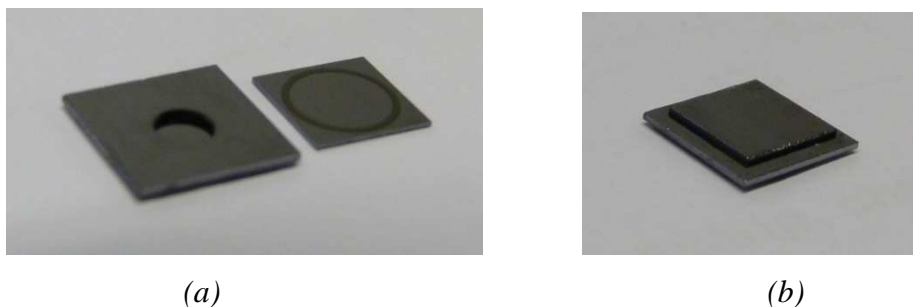
Figure 4.4: FTIR test packages: (a) LHS: Silicon substrate BCB sealed to centre silicon layer with 5mm diameter hole to create the package cavity, RHS: silicon cap with BCB seal ring. (b) Sealed silicon sample for FTIR testing.

Figure 4.5: Thermo Nicolet IN10 FT-IR

Some initial tests showed that the FTIR spectrometer used was able to detect the tracer gas, which had leaked into the packages during bombing as shown in figure 4.6. As these packages were sealed with BCB, a permeable material, no quantification of the *equivalent standard* leak rate was possible although using the Beer Lambert law, equation 4.1, re-arranged and written back here as equation 4.9; it is possible to estimate a *measured* nitrous oxide leak rate using the interferogam shown in figure 4.6.

$$P_p = -\frac{RT}{lA}\log(transmission) \qquad (4.9)$$
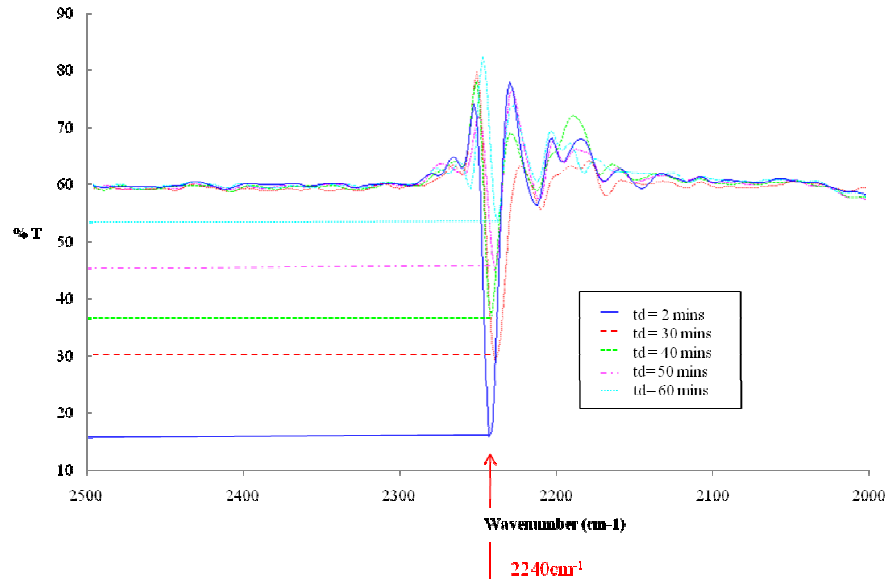
Figure 4.6: Initial FTIR spectrum showing N_2O absorption peaks

As silicon is transparent over the wavelength range considered here, 4 to 5 μm, 60 % of the incident light is transmitted through the package until, at 4.46 μm, the absorption peaks of the nitrous oxide tracer gas are observed. The nitrous oxide partial pressure is calculated using the following parameters. *l*, the depth of the cavity is equal to 500μm, *A*, the molar absorption coefficient of nitrous oxide is 250 L.mol^{-1}cm^{-1} [4.3], *R*, the universal gas constant is 8.3145, *T*, temperature is 293K and *transmission* is taken from the absorption peaks in figure 4.6. These percentages are normalised to the percentage of transmission through the package and the pressure inside the cavity is calculated using the Beer Lambert Law, equation 4.9, at each dwell time. The difference in partial pressure over the 58 minutes test time is calculated to be 0.01056 atm. Since the package contains a polymer seal material, it is inappropriate to use the molecular leak equation, equation 4.3, to calculate the permeation leak. Instead the permeation leak is calculated using the literal definition of leak rates, change in partial pressure multiplied by cavity volume divided by the change in time. The measured nitrous oxide leak rate under the bomb test conditions of the test package calculated using the literal definition of leak rate, under standard conditions of pressure and temperature, is 2.98×10^{-8} atm.cm^3.s^{-1}. Figure 4.7 shows a plot of the change in nitrous oxide partial pressure in the package cavity over time.
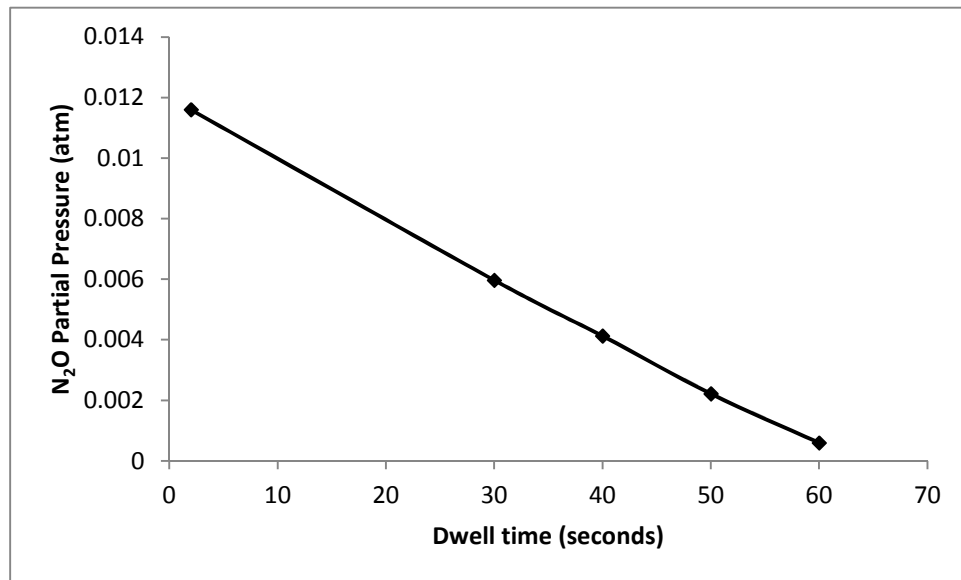
Figure 4.7: Measured N₂O partial pressure over time.

Figure 4.7 shows a linear change in pressure over time so it is likely that the dominant leak measured here is in fact a molecular leak caused perhaps by an imperfection leading to a crack in the BCB seal. Permeation leaks tend show a change in pressure over time which is slow at first, increasing over time as the gas sorbs onto the permeable package material and diffuses through to the external environment resembling an exponential curve. As this leak rate is likely to be caused by a molecular leak, determination of the *equivalent* leak rate would be correct for this example. Using equation 4.3 and considering the bomb pressure and bomb time, the measured nitrous oxide leak rate independent of the test conditions is 4.395×10^{-10} atm.cm^3.s^{-1}. The upper and lower *equivalent* leak rate calculated using equations 4.5 and 4.7 respectively are 1.6×10^{-3} atm.cm^3.s^{-1} and 4.08×10^{-9} atm.cm^3.s^{-1}, respectively. If the upper leak rate calculated here was apparent then the tracer gas inside the package would leak out completely within a second. Since we know from the FTIR interferogram that this is not the case, the test package must have a leak rate equal to the lower equivalent leak rate.

The FTIR spectrometer used was available through MCS Ltd and was not delivered to the company until November 2010. As this was out with the project completion date, further tests to establish the accuracy and sensitivity of this method were not possible. However, using an in-situ test structure within a test package cavity, it would be possible to determine the accuracy and sensitivity of the FTIR set-up at MCS Ltd for leak detection applications.

101

4.1.4   Summary

In summary the FTIR leak test can be used to measure the molecular leak rates of lower cavity volume of MEMS and microelectronics packages than is possible using the helium leak test method. A gross leak test is still required and a volume limitation is apparent and must be considered when applying this test method with a dwell time of more than one hour to packages below 3.12×10^{-3} cm^3, an order of magnitude lower than the minimum volume which can be accurately testing using the helium leak test.

The minimum detectable leak rate of this test method when applied to measure molecular leak rates depends on the test parameters used. The lower the cavity volume and detectable partial pressure of tracer gas, the lower the detectable leak rate. The higher the bomb time and bomb pressure, the lower the detectable leak rate, however, the bomb pressure cannot be increased indefinitely as 'one way' leaks will occur. The lower limit of the FTIR method does not only depend on the sensitivity of the detection equipment as is the case for the helium leak detection method.

This test can be used to determine whether or not a package containing permeable materials is leaking but the mathematics involved to convert the nitrous oxide measured leak rate to an equivalent standard air leak rate is complex. It is not as yet possible to convert the permeation rate of one gas type through a package material to another as the rate is not dependent only on the molecular weight and size of the permeating particles but also on their chemical affinity with the material through which it is permeating.

4.2   Raman Spectroscopy

Raman spectroscopy is an optical technique, which uses a monochromatic light source to interact with phonons and other molecular vibrations of an unknown molecule. The light source used is usually a laser source and can be in the visible, ultraviolet or infrared range. The incident light interacts with the phonons or molecule vibrations and excites the molecule from the ground state to a virtual energy state. Upon relaxation, a photon is released which shifts the energy of the excitation photon [4.5]. The energy difference between the incident light and the scattered light corresponds to the unique

energy difference between the vibrational modes of the molecule. After passing through the sample, the light is collected by a lens and passed through a monochromator which filters the wavelengths close to the incident light, usually caused by Rayleigh scattering and the rest passes through to the detector. Raman spectra can be produced from the detector results and are expressed in wavenumbers, cm^{-1}. The peaks in Raman shift can be compared to known samples and the molecules present can be identified. As with FTIR, the Beer Lambert Law, equation 4.1, can theoretically be used to relate the intensity of the peaks to the concentration of molecules present and hence the pressure of the foreign gas can be determined.

4.2.1 Application to the hermeticity test

Weber et al. used Raman spectroscopy to determine the hermeticity of hermetically sealed micromachined accelerometers packaged in silicon with a Pyrex window [4.6]. The device was packaged in an inert gas atmosphere. For inertial devices such as accelerometers, Q-factor testing is often used to monitor hermeticity. However, when devices are packaged in an inert atmosphere, partial pressure gradients mean that contaminants can leak into the package as the inert gas leaks out without a change in the overall pressure; as a result the Q-factor might not be changing. Weber et al. recognised this limitation and used Raman spectroscopy to detect contaminant gases. The contaminant gas of interest in their study was air or more accurately the oxygen present in air [4.6]. Degradation occurs slowly in the presence of oxygen and reliability of the device is then compromised, hence the need to package the device in inert gas.

4.2.2 Theoretical limitations

The minimum detectable leak rate of the Raman spectroscopy method is directly related to the number of counts, corresponding to a calibrated number of photoelectrons, which can be successfully resolved. Raman scattering is weak and one of the biggest challenges for Weber et al. was to determine the strength of the oxygen signal from the noisy background. This was essential to be able to use the technique as a quantitative test method. Weber et al used complex line shape analysis described fully in their paper to determine the leak rate of their packages with the least uncertainty [4.6]. Weber et al used the ratio of the oxygen and nitrogen peaks to determine whether the packages concerned have large or small leak rates by comparing this ratio to the ratio apparent in

air. The experiment was successful in indicating gross and fine leaks but the errors involved and the difficulty in extracting the oxygen signal from such a noisy background meant that it was not possible to determine a meaningful quantitative leak rate of the packages.

Weber et al. concluded that this method was currently not useful as an end-of-line test method because of the long integration time required to collect the data with a sufficient signal to noise ratio [4.6]. However, this technique is able to determine, without the need for sample preparation, whether or not the internal cavity environment has changed since packaging. Although the method is time consuming and the signal to noise ratio too small to derive accurate figures of leak rate, it may be very useful as a failure analysis technique. One of the most challenging problems when conducting failure analysis is to ensure that the analysis itself does not perturb the original condition of the device. As this is a non-destructive, non-invasive method of determining whether the internal cavity environment has changed, it can be used to assess before any package preparation, whether a failure could have been environmentally induced. As the method does not use a tracer gas, it is able to detect leaks caused by any type of capillary leak (molecular, transitional or viscous), permeation leaks and, depending on the signal to noise ratio, outgassing. This could be a powerful addition to the portfolio of test methods currently available for hermeticity testing.

4.2.3 Practical considerations

A practical limitation of using Raman spectroscopy to determine the leak rate of packages is the time taken to conduct the test. In order to achieve a signal to noise ratio that is large enough to ensure that the weak Raman scattering can be extracted from the background, the time to acquire the Raman spectra is increased. Weber et al. reported that this would be a problem that would limit the use of Raman spectroscopy as an end-of-line testing method unless the confocal rejection could be improved by using a higher power laser [4.6].

Another way to decrease the time to test would be to use a tracer gas and a sample bombing procedure as used in the FTIR hermeticity test method and the helium fine leak test method. However, if this procedure were employed, the advantages of the

Raman spectroscopy method would be compromised: a volume limitation would become apparent due to the time elapsed between bombing and testing; the test could not be applied quantitatively to packages containing permeable materials as is the case for the FTIR hermeticity test method and outgassing could not be detected.

When considering the use of Raman spectroscopy the package must have a transparent cap and a reflective lower surface. If visible light is used, the cap material could be glass and the substrate silicon, which makes this technique ideal for many MEMS packages including MOEMS, which are often packaged in inert gas to minimise fogging of optical components. Raman spectroscopy can also be conducted using ultra-violet and infra-red incident light.

During testing it is necessary for the interface between the microscope and the probe-head to be purged with argon to eliminate the background oxygen and nitrogen in air from the measured spectra. During planning of this project it was decided that the experiments of Weber et al. should be conducted using a Raman spectrometer available at Heriot-Watt University and shown in figure 4.8. It was thought that the Renishaw inVia Raman Microscope with high sensitivity and ultra low noise CCD detector may allow the oxygen signal to be extracted with less uncertainty from the background making this method quantitative. It would then be possible to determine the minimum leak rate of the Raman spectroscopy method. This could be added to the portfolio of hermeticity test methods for MEMS and low cavity volume microelectronic packages. The result would also be indicative of whether or not the method could be used as a non-destructive technique to determine the level of outgassing from the internal device and packaging materials.

Figure 4.8: Renishaw inVia Raman Microscope

Initial experiments were conducted on sample packages fabricated by Mr. Norbert Lorenz and Mr. Martin Smith. The samples have a lower silicon substrate with a borosilicate glass cap bonded using BCB with a diameter of 13 mm and thickness of 16 µm. The height of the BCB seal creates the package cavity, figure 4.9. During these experiments it became clear that the working distance was not large enough to allow the probing light to be focussed through the cap material into the sample cavity. The cost of purchasing a lens, which would allow us to use the available Raman microscope for this purpose was prohibitive and the experiment could not be completed. Lenses with greater working distances could be borrowed from the Physics department of Heriot-Watt University but, due to the metric fittings of the Renishaw Raman microscope, an adaptor was required. The addition of this adapter and lens to the Raman microscope meant there was insufficient space for the test sample to be inserted between the lens and microscope stage.
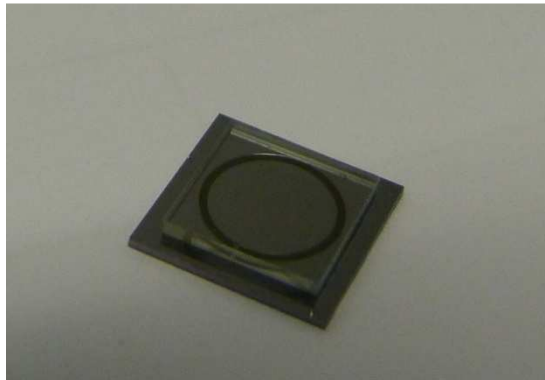
Figure 4.9: Samples intended for testing using Raman spectroscopy

4.2.4 Summary

Raman spectroscopy cannot currently be used as a hermeticity test method to determine the leak rate of low cavity volume packages as the weak Raman scattering from contaminant gases is lost in the background noise. With better confocal rejection it may be possible to use this technique. The Raman spectrometers available today have higher specification detectors and higher power lasers and so it may now be possible to use this technique to conduct quantitative tests. Due to project funding limitations this investigation could not be conducted and reported in this thesis.

It is possible to use tracer gas sample bombing with Raman spectroscopy but doing so brings the volume, minimum detection and leak type limitations, which are applicable to the FTIR hermeticity test. The unique advantages of the Raman spectroscopy technique are then lost.

Raman spectroscopy without the use of a tracer gas can be used to determine whether a package initially filled with an inert gas or vacuum has a gross or fine leak. The packages to be tested using Raman spectroscopy should have a transparent cap and reflective lower surface according to the wavelength of probing light used. It is possible to use ultra-violet, visible or infra-red light. Because this method does not use a tracer gas, any type of leak can be detected including capillary leaks, permeation and potentially outgassing, depending on the signal to noise ratio and the extent of the outgassing.

This technique is not suited to end-of-line testing due to the long test time required but is ideal for use as a failure analysis method. Raman spectroscopy could be used to indicate device failure due to changes in environmental conditions non-destructively and with no need for device preparation. Currently the only way to determine the internal gas composition of a failed package cavity is to conduct residual gas analysis which, however effective, completely destroys the package meaning no further tests can be conducted. Raman spectroscopy is also considerably cheaper than RGA.

4.3   Conclusions

FTIR hermeticity testing and Raman spectroscopy have been investigated in this chapter and their advantages and limitations have been described in detail. Table 4.1 is carried forward from Chapter 2. The results of the newly characterised FTIR and Raman test methods have been added and are highlighted in blue. This table should be used as a living document and updated as the current test methods are improved and new test methods are discovered.

Test Method	Detectable range limitations	Practical limitations	Leak types detected	Suitable package materials	Unsuitable package materials
Helium fine leak	Volume limitation: > 2.6×10^{-3} cm^3 Min. detectable leak rate: 1.28×10^{-10} atm.cm^3.s^{-1}	Increased dwell time required when surface sorption present causing larger volume limit	Leak channels: molecular leaks	Silicon Metals Ceramics	Polymers Glass Epoxies
Radioisotope fine leak	Min. detectable leak rate: 10^{-12} atm.cm^3.s^{-1}	Licensing, handling and disposal of radioisotopes	Leak channels: Molecular and viscous (combinational test)	Silicon Metals Ceramics Glass	Polymers Epoxies
Optical leak detection	Min. detectable leak rate: 10^{-10} atm.cm^3.s^{-1}	Calibration of every package type required	Leak channels Permeation (of tracer gas)	Any material as long as cap thickness and flexibility is appropriate	Rigid cap materials.
Cumulative helium leak detection	Min. detectable leak rate unclear: $10^{-10} - 10^{-14}$ atm.cm^3.s^{-1}	Calibrating system to ensure lowest possible detection limit	Leak channels	Silicon Metals Ceramics	Polymers Glass Epoxies
Residual gas analysis	10^{-16} depending on MS sensitivity	Destructive and very expensive	Leak channels Permeation Outgassing	Any material	n/a
FTIR leak detection	Volume limitation: > 7.36×10^{-4} cm^3 Min. detectable leak rate: depends on sample and experimental parameters, typically, 10^{-13} atm.cm^3.s^{-1}	Min. detectable leak rate and volume limitations dependent on min. partial pressure measurement which is sample dependent and must be calibrated	Leak channel: molecular leak (Howl-Mann method) Permeation – rate cannot be converted to equivalent standard leak	Silicon Some glass	IR absorbing glass Polymers Ceramics Epoxies Non IR transparent metals (for N$_2$O tracer gas Howl-Mann method)
Raman spectroscopy	n/a distinction between fine and gross only	Slow test procedure can be improved by increased signal to noise ratio.	Leak channels Permeation Outgassing	Glass Silicon IR/visible or UV transparent polymers and epoxies	Ceramics IR/visible or UV non-transparent polymers and epoxies

Table 4.1: Summary of hermeticity test methods

4.4   References

[4.1]   P. Griffiths, and J.A. de Hasseth, '*Fourier Transform Infrared Spectroscopy*' 2nd ed., John Wiley & Sons Inc., Hoboken, New Jersey, 2007.

[4.2]   M. Nese, R.W. Bernstein, I.R. Johansen and R Spooran, *'New method for testing hermeticity of silicon sensor structures'*, Sensors and Actuators A, 53, pp. 349-352, 1996

[4.3]   D. Veyrié, D. Lellouchi, J.L. Roux, F. Pressecq, A. Tetelin and C. Pellet, '*FTIR spectroscopy for the hermeticity assessment of micro-cavities*', Microelectronics Reliability, 45(9-11), pp. 1764-1769, 2005.

[4.4]   Lorenz, N., Millar, S. and Hand, D., "Localised laser joining of micro-devices for hermetic packaging using a glass frit intermediate layer", *Proceedings of the 5th International WLT-Conference on Lasers in Manufacturing*, Munich, (2009).

[4.5]   D.J. Gardiner, '*Practical Raman spectroscopy'* (1st ed.), Springer- Verlag, 1989.

[4.6]   W.H. Weber, M. Zanini-Fisher, and M.J. Pelletier, *'Using Raman Microscopy to Detect Leaks in Micromechanical Silicon Structures'*, Society for Applied Spectroscopy, 51(1), pp. 123-129, 1997.

Chapter 5

Piezoresistive cap deflection technique

for in-situ hermeticity testing

5.1   Current in-situ sensors in hermeticity testing

In-situ test structures have been proposed as an alternative to traditional external testing as such devices have the potential to detect ultra low leak rate, in a non-destructive manner.

Copper test patterns have been demonstrated for the determination of the hermeticity of MEMS packages [5.1].   This method involves the measurement of the optical transmission of copper test thin films over time. As the copper oxidises, the optical transmission coefficient changes and the oxidation rate can be determined. As the oxidation rate is proportional to the amount of oxygen available in the ambient environment, this method was used to measure the hermeticity of MEMS packages. Infrared light is used to determine the optical transmission of thin copper layers deposited within the package cavity; like the FTIR method, silicon capped packages are suitable [5.1]. The test samples were exposed to 1% oxygen and 99% argon and the temperature of the package was raised to between 125°C and 150°C to promote oxidation [5.1]. Depending on the amount of deposited copper within the cavity, the test gas pressure can be increased to allow sufficient oxygen to leak into the package to show oxidation [5.1]. The method is able to detect a leak rate of 4.935×10^{-16} atm.cm^3.s^{-1} although several days of test time are necessary to observe this leak rate at increased pressure [5.1]. The test is also limited to packages with infrared transparent packaging and requires optical equipment for detection purposes. This test method could not be used over the device lifetime since the leaking gas must be oxygen and, once oxidised by the initial test, the copper test pattern cannot be used again. In-situ test structures that do not rely on optical measurement and can be used throughout the device lifetime as failure analysis tools would be advantageous.

Q-factor testing has been used to determine the pressure, hence the leak rate of packages by many research groups and as a commercial end-of-line test. The damping of any

resonating structure can be characterised by its Q-factor, a dimensionless parameter which describes the damping experienced by an oscillating structure. A high Q-factor indicates that the resonator experiences low damping. The Q-factor of MEMS resonating structures is highly dependent on the cavity environment in which it is packaged. Most resonant MEMS structures are packaged in vacuum to ensure a high Q-factor and optimum performance. These devices are the most sensitive to package leakage; as the cavity pressure increases, damping is increased and the device performance is altered. As resonant structures are often sensors, a change in performance means a change in sensing output, which can have a detrimental effect to the end application.

The Q-factor of the device is measured before packaging over a range of ambient pressures. After packaging in vacuum or inert gas depending on the application, the Q-factor is measured again to confirm the present cavity pressure. This measurement step can be useful to highlight packaging problems including outgassing from packaging and device material layers into the cavity. The Q-factor of the device can be extracted by applying an AC or DC voltage to bring the device into resonance and amplifying. The Q-factor can be determined from the measure of the dielectric loss or the conductance using an impedance analyser or a LCR meter [5.2]. Van der Wel et al. of NXP Semiconductors used this technique successfully to determine the reliability of an RF capacitive switch sealed in a nitrogen atmosphere using gold-tin bonding [5.2]. The Q-factor test is capable of measuring leak rates of the order 10^{-14} atm.cm^3.s^{-1} [5.3]. The method is non-destructive and can be used at anytime throughout the device lifetime to determine the internal cavity pressure and hence leak rate. This technique would require acceleration using a bombing technique or other stress test if it were to be used as an end-of-line test method.

The ultra-low neon leak detection method uses neon or argon as a bombing gas in order to accelerate the Q-factor test method for end-of-line testing. The Q-factor of the resonant device before and after bombing is measured using the ring-down method, which involves the measurement of the half-amplitude decay time of the damped sinusoidal wave [5.4]. The optimum bomb pressure is 3.948 atm and a bomb time of between 10 and 100 hours [5.4]. Leak rates as low as 9.86×10^{-17} atm.cm^3.s^{-1} can be detected using this method.

The test is not linked by cavity volume but requires the MEMS structure itself to be resonant. This is not always the case and the Q-factor test is not generally applicable to microelectronics. As the cavity volumes reduce year on year in the MEMS industry, the problems seen in MEMS hermeticity testing are becoming more pressing. The test method can be very sensitive but a significant amount of calibration is necessary and the measurement of Q-factor is not as straightforward as desirable.

The most desirable method of test for high volume manufacturing is Known Good Die testing (KGD) whereby all die are tested using automated electrical testing to determine known good die at various stages of fabrication and particularly after 0-level packaging, before wafer cutting. For this to be possible, in-situ test structures, which can give an electrical response to changing ambient pressure, are required. These test structures should be as accurate and sensitive as possible to enable the detection of ultra-low leak rates. The test structures themselves must have a very small footprint to ensure minimum chip real estate is required. The test structure fabrication steps should also be in keeping with the fabrication steps required to produce the device itself to minimise the cost of manufacture.

Deflecting membranes have been used as pressure sensors for many applications. They have also been used as a way of monitoring hermeticity as described in section 2.3.7 of this thesis. The main issue with this test method is the fact that the package cap itself must be used as the test structure and deflection of this cap is measured optically. For optimal sensitivity the cap should be as thin as possible to allow maximum deflection for detection of small pressure changes. Suitably thin package caps are not mechanically strong enough to serve as outer packaging and so secondary packaging is required and must be transparent to allow optical access to the deflecting cap. This chapter provides a novel way to determine electrically the deflection of the membrane, which is related to the pressure inside the package.

5.2   Theory of the piezoresistive cap deflection test structure

This in-situ test structure uses four piezoresistors on a silicon membrane connected on chip in a Wheatstone bridge configuration to monitor electrically the change in membrane deflection caused by a pressure change within the package. As the

measurement is electrical, the secondary packaging of the chip need not be transparent as is the case in the optical measurement of the silicon cap deflection. Another advantage is that KGD testing can be performed on all packages before and after secondary packaging. To determine a leak rate using this test structure, the wafers should be bombed in an inert tracer gas as described in section 2.3.7 and the cap deflection measured electrically. Electrical measurement is also advantageous as it is quick and does not rely on optical equipment, which can be costly and requires calibration. After test, the chips can be non-hermetically packaged again using a mechanically strong material in ambient conditions as shown in figure 5.1. To ensure this process has not affected the hermeticity of the 0-level silicon capped package, the electrical test can be performed again. Any change in cap deflection from the previous test in atmospheric conditions indicates package failure.
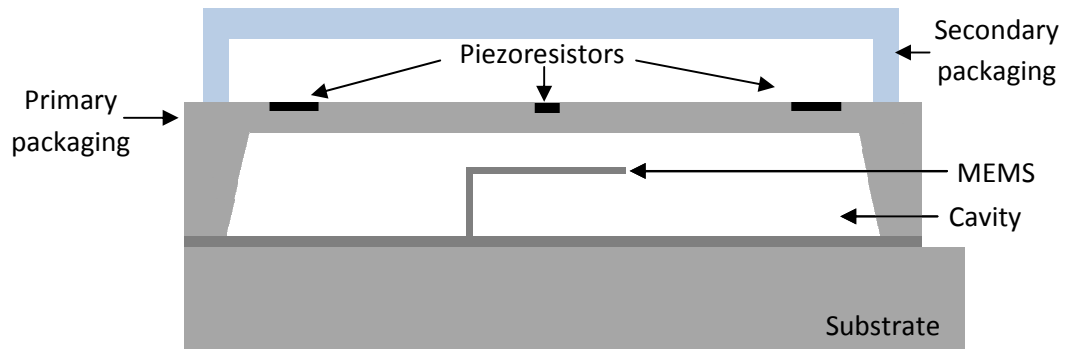
Figure 5.1: Primary and secondary MEMS packaging using piezoresistive cap deflection for hermeticity evaluation.

The theory of pressure sensors based on piezoresistors connected in a Wheatstone bridge configuration on a square flexible membrane has been researched considerably. Several papers have shown good correlation between numerical calculations and simulated results [5.1, 5.2]. To understand the relationship between the pressure change and the deflection of the membranes, the equations derived by Pang et al. and Elgamel were used [5.5, 5.6] although it was found that some mathematical errors were made in these articles. The corrected equations are provided here and a note has been sent to the editors of the journals in which the errors were found. Two cap deflection structures with different membrane thicknesses and membrane areas were designed. The piezoresistors are orientated along the <110> crystallographic direction for maximum sensitivity. The thicknesses, h, of the thin and thick membranes are 3.1 µm and 23.1 µm, respectively. The lengths, L, of the square membrane of the thin and thick test

structures were 398.4 µm and 1468.4 µm, respectively. Assuming that the deflection of the membrane is small compared to the thickness of the membrane, as is the case for both the thin and thick membranes described here, the Airy's stress function, F, is given by equations 5.1 and 5.2. Equation 5.2 does not account for any contribution of the thermal moment of the membrane thickness due to the thermal mismatch between the silicon and dielectric layer [5.5, 5.6].

$$\frac{\partial^4 F}{\partial x^4} + 2\frac{\partial^4 F}{\partial x^2 \partial y^2} + \frac{\partial^4 F}{\partial y^4} = E\left[\left(\frac{\partial^2 w}{\partial x \partial y}\right)^2\right] - \frac{\partial^2 w}{\partial x^2}\frac{\partial^2 w}{\partial y^2}$$
(5.1)

$$\frac{\partial^4 w}{\partial x^4} + 2\frac{\partial^2 w}{\partial x^2 \partial y^2} + \frac{\partial^4 x}{\partial y^4} = \frac{12(1-v^2)}{Eh^3} \times \left[P_a + h\left(\frac{\partial^2 F}{\partial x^2}\frac{\partial^2 w}{\partial y^2} - 2\frac{\partial^2 F}{\partial x \partial y}\frac{\partial^2 w}{\partial x \partial y} + \frac{\partial^2 w}{\partial x^2}\frac{\partial^2 F}{\partial y^2}\right)\right]$$
(5.2)

Where E is Young's modulus, v is Poisson's ratio, w is the deflection of the membrane, P_a is the applied pressure, and L and h are the previously defined membrane dimensions. Pang et al. and Elgamel show that for square membranes under the boundary conditions $w=0$, $\partial w/\partial x=0$ at $x=+/-L/2$ and $w=0$, $\partial w/\partial y=0$ at $y=+/- L/2$, the diaphragm deflection, w, is given by equation 5.3 [5.5, 5.6]. This equation is an approximation of the true expression which is an infinite series of cosine terms whose second and further terms have negligible contribution to $w(x, y)$.

$$w(x, y) = hf\cos^2\left(\frac{\pi x}{L}\right)\cos^2\left(\frac{\pi y}{L}\right)$$
(5.3)

Where f, is a function dependant on E, v, P_a, L and h. In the following equations f will be defined as $f(P_a)$ to emphasise this functions dependence on pressure. Substituting equation 5.3 into equation 5.1 gives:

$$\frac{\partial^4 F}{\partial x^4} + 2\frac{\partial^4 F}{\partial x^2 \partial y^2} + \frac{\partial^4 F}{\partial y^4} = \frac{-\pi^4 h^2 E}{2L^4}[f(P_a)]^2 \times \begin{bmatrix} \cos\left(\dfrac{2\pi x}{L}\right) + \cos\left(\dfrac{2\pi y}{L}\right) + \cos\left(\dfrac{4\pi x}{L}\right) \\[2mm] + \cos\left(\dfrac{4\pi y}{L}\right) + 2\cos\left(\dfrac{2\pi x}{L}\right)\cos\left(\dfrac{2\pi y}{L}\right) + \\[2mm] \cos\left(\dfrac{4\pi x}{L}\right)\cos\left(\dfrac{2\pi y}{L}\right) + \cos\left(\dfrac{2\pi x}{L}\right)\cos\left(\dfrac{4\pi y}{L}\right) \end{bmatrix}$$

(5.4)

The solution to equation 5.4, equation 5.5, satisfies the boundary conditions $q=0$, $\partial^2 F/\partial x\partial y=0$ at $x=+/-L/2$ and $p=0$, $\partial^2 F/\partial x\partial y=0$ at $y=+/-L/2$ where q and p are the mid-plane displacements of a diaphragm with built in edges in the x and y directions respectively are applied.

$$F(x,y) = -\frac{Eh^2}{32}[f(P_a)]^2 \begin{bmatrix} \dfrac{3\pi^2}{12L^2\left(1-v^2\right)}(x^2+y^2) - \cos\left(\dfrac{2\pi x}{L}\right) - \cos\left(\dfrac{2\pi y}{L}\right) \\[3mm] -\dfrac{1}{2}\cos\left(\dfrac{2\pi y}{L}\right) - \dfrac{1}{16}\cos\left(\dfrac{4\pi x}{L}\right) - \dfrac{1}{16}\cos\left(\dfrac{4\pi y}{L}\right) \\[3mm] -\dfrac{1}{25}\cos\left(\dfrac{4\pi x}{L}\right)\cos\left(\dfrac{2\pi y}{L}\right) - \dfrac{1}{25}\cos\left(\dfrac{2\pi x}{L}\right)\cos\left(\dfrac{4\pi y}{L}\right) \end{bmatrix}$$

(5.5)

Substituting equations 5.3 and 5.5 into equation 5.2 yields an error function from the approximation of $w(x,y)$ described previously, given by [5.5, 5.6]:

$$e(x,y) = \frac{\partial^4 w}{\partial x^4} + 2\frac{\partial^4 w}{\partial x^2 \partial y^2} + \frac{\partial^4 w}{\partial y^4} - \frac{12(1-v^2)}{Eh^3}$$
$$\times \left[P_a + h\left(\frac{\partial^2 F}{\partial x^2}\frac{\partial^2 w}{\partial y^2} - 2\frac{\partial^2 F}{\partial x\partial y}\frac{\partial^2 w}{\partial x\partial y} + \frac{\partial^2 w}{\partial x^2}\frac{\partial^2 F}{\partial y^2}\right) \right]$$

(5.6)

To minimise the error function, the Ritz-Galerkin method is employed which requires [5.5, 5.6]:

$$\iint e(x,y)w(x,y)dxdy = 0$$

(5.7)

115

Equations 5.3 and 5.7 can be rewritten as equation 5.8:

$$\frac{-3\pi^4 h^2 (1-v^2)}{L^2} \left[\frac{3}{128(1-v^2)} + \frac{533}{3200} \right] \left[f(P_a) \right]^3 + \frac{2\pi^4 h^2}{L^2} \left[f(P_a) \right] - \frac{3(1-v^2)L^2}{Eh^2} P_a = 0 \quad (5.8)$$

This expression can be used to determine $f(P_a)$. Setting $E = 1.68 \times 10^{11}$ Nm^{-1}, $v = 0.066$, h and L are the parameters for the thin and thick membranes, equation 5.8 becomes equation 5.9 and 5.10, respectively.

$$-0.335 \left[f(P_a) \right]^3 + 1.180 \left[f(P_a) \right] - 2.936 \times 10^{-5} P_a = 0 \quad (5.9)$$

$$-1.369 \left[f(P_a) \right]^3 + 4.821 \left[f(P_a) \right] - 7.184 \times 10^{-6} P_a = 0 \quad (5.10)$$

Equations 5.9 and 5.10 have only one real root, which is dependent on the input parameters P_a, E, v, L and h. Membrane deflection can be calculated by equation 5.3, where, x and y are the position on the membrane at which the deflection is calculated [5.5]. When $x = y = 0$, the deflection is calculated at the centre of the membrane. Figure 5.2 shows a plot of the thin and thick membrane deflection at the centre of the membrane as a function of applied pressure.
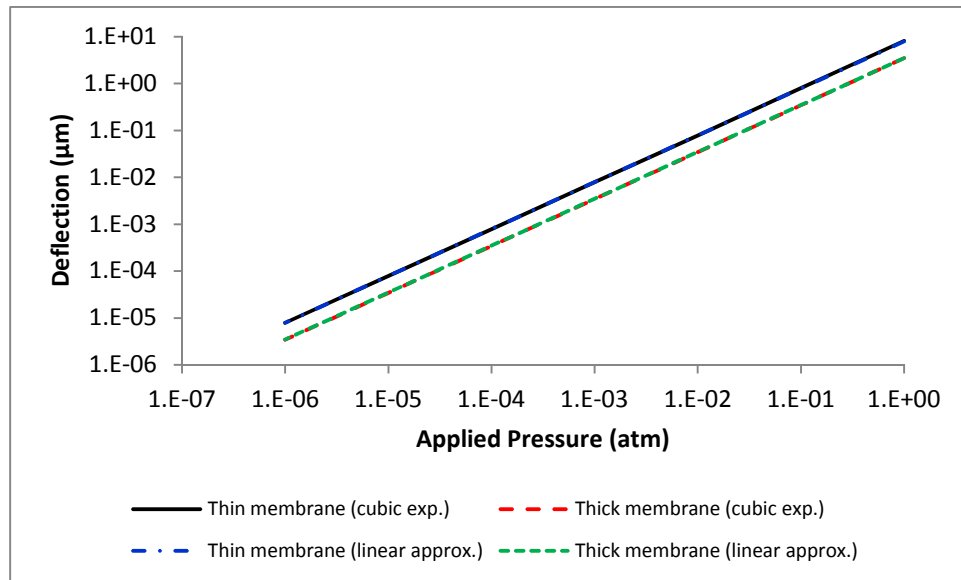
Figure 5.2: Theoretical deflection of the designed thin and thick membranes as a function of applied pressure.

116

Figure 5.2 also shows the theoretical deflection of the designed thin and thick membranes using a linear approximation with an R^2 value of 0.998 and 0.999 respectively. The cubic terms in equations 5.9 and 5.10 have a negligible impact on the deflection of the thin and thick membranes so that equation 5.8 can be simplified to:

$$\frac{2\pi^4 h^2}{L^2}[f(P_a)] - \frac{3(1-\nu^2)L^2}{Eh^2}P_a = 0 \tag{5.11}$$

The linear approximations for the thin and thick membranes, equations 5.12 and 5.13, can be used to determine the deflection of the membrane.

$$w_{thin} = 2.488 \times 10^{-5} hP_a \tag{5.12}$$

$$w_{thick} = 1.490 \times 10^{-6} hP_a \tag{5.13}$$

To calculate the expected change in resistance and hence the change in output voltage of the test structure when the applied pressure is varied, we normalise the dimensions of the membrane as defined in figure 5.3.
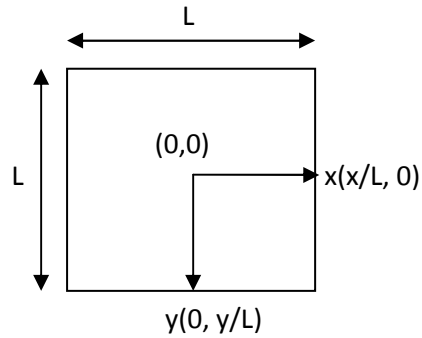
Figure 5.3: Normalised dimensions of the membrane.

The piezoresistors of the thin and thick test structures were positioned due to the design rules of the fabrication process at (L/4, 0) and (L/8, 0) respectively as shown in figure 5.4. The theoretical deflections of the membranes in these positions are therefore given by equation 5.14 and 5.15, respectively using equation 5.3.
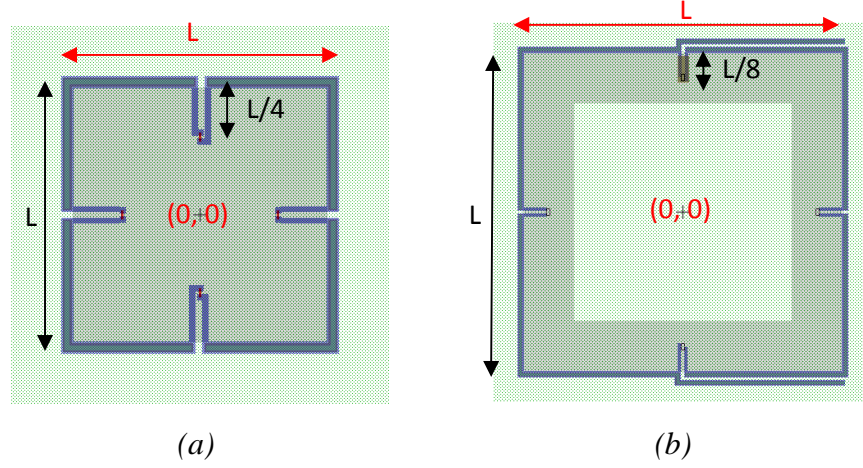
Figure 5.4: Piezoresistors position on (a) thin and (b) thick membrane.

$$w_{thin} = 0.5h\big[f(P_a)\big] \tag{5.14}$$

$$w_{thick} = 0.85h\big[f(P_a)\big] \tag{5.15}$$

In the case of the designed cap deflection test structures, the pressure is applied to one side of the membrane where the holes in the bottom glass provide access to the structure. The other side of the membrane is sealed under vacuum conditions and so, in atmospheric conditions, the membrane deflects inwards towards the top glass. The membrane will therefore be in equilibrium, i.e. the bridge voltage will equal zero, when the applied pressure is equal to the pressure contained in the cavity sealed by the top glass. In this case, the applied pressure should be plotted as differential pressure, and the output voltage will change polarity when the deflection of the cap goes through zero. Figure 5.5 shows the theoretical deflection of the thin and thick membranes at the positions of the piezoresistors when the cavity pressure is assumed to be 0.049 atm as stated by the manufacturers.
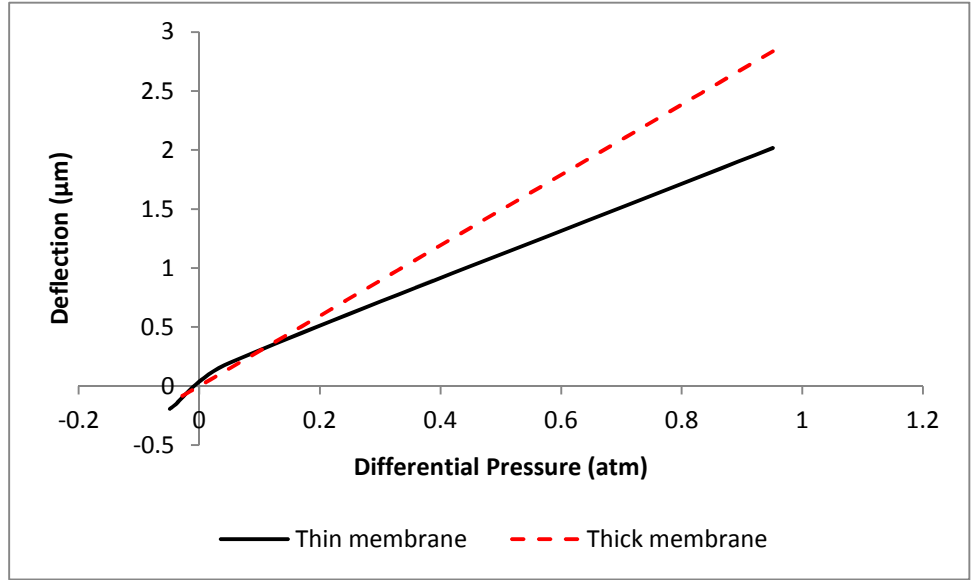
Figure 5.5: Theoretical deflection of the designed thin and thick membranes in the location of the piezoresistors as a function of differential pressure.

Following Pang et al., assuming a supply voltage, V_{ref}, and a differential output voltage ΔV, the dimensionless output voltage of the bridge is given by:

$$\frac{\Delta V}{V_{ref}} = \frac{1}{2}\pi_{44}s \qquad (5.16)$$

where $\pi_{44} = 2\pi_{//}$ and $\pi_{//}$ is the longitudinal piezoresistive coefficient and s is the effective mechanical stress of the membrane, given by:

$$s = \frac{Eh}{1-v^2}\frac{\partial^2 w}{\partial y^2}(1-v) \qquad (5.17)$$

Differentiating equation 5.1 with respect to y twice and substituting into equation 5.17 gives:

$$s = \frac{2Eh}{1-v^2}\left(\frac{\pi}{L}\right)^2 h[f(P_a)]\ \cos^2\left(\frac{\pi x}{L}\right)\cos\left(\frac{2\pi y}{L}\right)(1-v) \qquad (5.18)$$

Substituting into equation 5.18 the corresponding input parameters for the thin and thick membranes and assuming the piezoresistors are positioned as shown in figure 5.4, the output voltage can be calculated by then substituting equation 5.18 into equation 5.16.

Figure 5.6 shows the theoretical output voltage of the thin and thick membranes as the applied pressure was varied; resulting in a change in differential pressure.
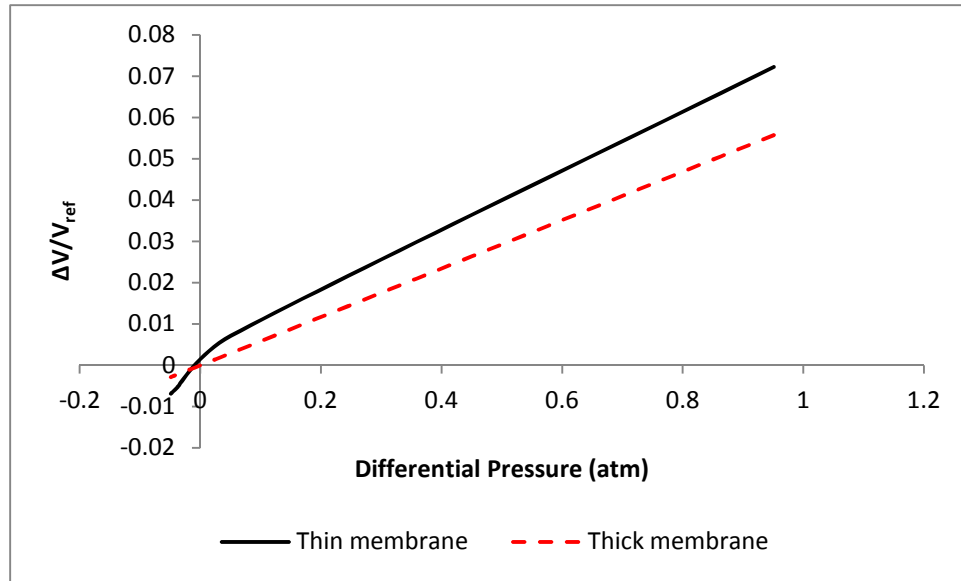
Figure 5.6: Theoretical output voltage of the thin and thick membranes as a function of differential pressure.

Figure 5.6 shows that the cap deflection test structures should work well when the differential pressure is between 0 atm and 1 atm. The sensitivity of the cap deflection test structures, S_{CD}, can be calculated by [5.5]:

$$S_{CD} = \frac{1}{V_{ref}}\frac{\partial V_{out}}{\partial P_d} \qquad (5.19)$$

Where V_{out} is the output voltage recorded over the differential pressure range. The theoretical calculations predict that the sensitivity of both the thin and thick membranes in this pressure range will be 72.2 mV/V.atm and 58.6 mV/V.atm, respectively. Considering that it is possible to accurately measure changes in voltage down to μV, the change in pressure detectable using the cap deflection test structure is of the order 10^{-6} atm. Considering a standard package with a volume of 1×10^{-5} cm^3, leak rates of the order 10^{-14} atm.cm^3.s^{-1} could be detected in ambient condition within an hour. Using a bombing technique as described in section 2.3.7, the test could be accelerated to make it possible to detect even lower leak rates.

The theoretical sensitivity of the thick membrane was calculated to be less than that of the thin membrane, which was expected since the ratio of membrane thickness to length indicated that the thin membrane would be more sensitive.

5.3   Design and fabrication process

The piezoresistive cap deflection structure designed to give an electrical response to changing ambient pressure was fabricated using the Multi Project Wafer (MPW) foundry process, MultiMEMS, from the Infineon Technologies SensoNor AS. The MultiMEMS foundry process is suitable for piezoresistive detection and thermal excitation [5.3]. SensoNor's established processes include sensitive surface piezoresistors; precise control of diaphragm thicknesses using an electrochemical etch-stop; release etching using reactive ion etching; an epitaxial layer for thin diaphragms and beams; and sealed or vented cavities [5.3]. These characteristics make the MultiMEMS process an ideal foundry process for the fabrication of in-situ test structures for hermeticity testing. The manufacturing techniques are based on bulk silicon and borosilicate glass micromachining and hence the structure designed here is suited to similar manufacturing processes, which are commonplace in the MEMS industry.   The devices are fabricated on a silicon wafer which is enclosed by borosilicate glass forming a 6 mm x 6 mm x 1.45 mm glass/silicon/glass triple layer package as shown in figure 5.7 (a). In order to calibrate the in-situ test structures effectively, four holes in the bottom glass layer of the chips were made to allow access to the package cavity, figure 5.7 (b).

(a)   *(b)*
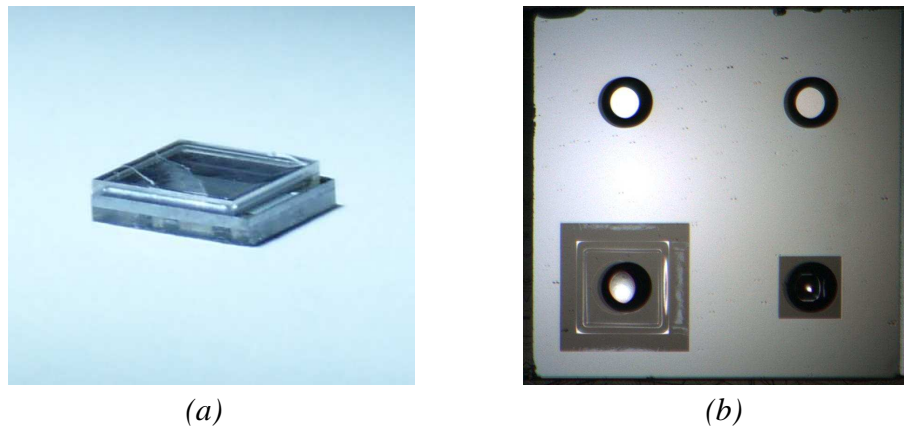
Figure 5.7: (a) Glass/silicon/glass MEMS die manufactured by MultiMEMS. (b) Holes in bottom glass.

The design rules of the MultiMEMS process gave dimensional limits for both thin, 3.1 µm, and thick, 23.1 µm, square membranes. The thin membrane has maximum tolerable dimensions of 430 µm and the thick membrane has maximum tolerable dimensions of 3480 µm. To test the sensitivity and range of each membrane thickness, two membranes, one thick and the other thin were designed on each chip. The design of the cap deflection in-situ test structure is shown in figures 5.8 and 5.9.
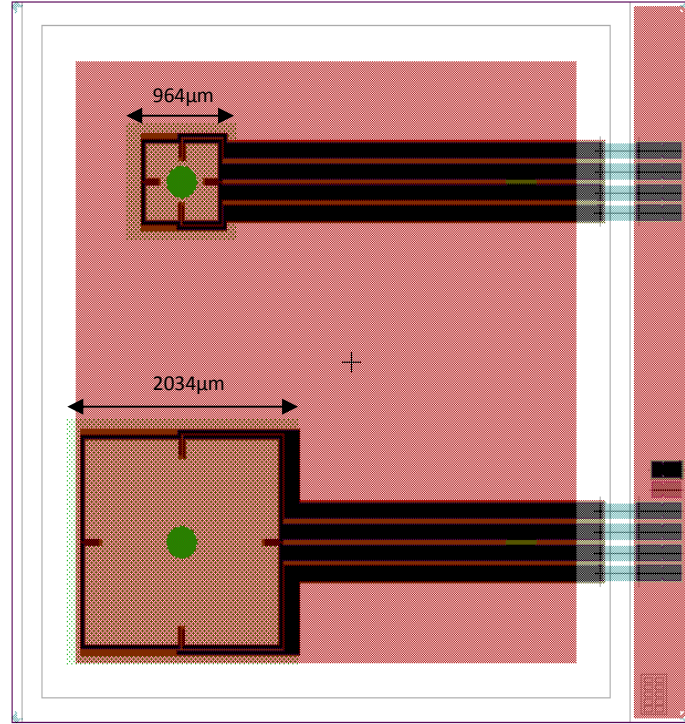
Figure 5.8: Design of cap deflection test structures. The thin membrane structure is shown at the top. The thick membrane structure is shown at the bottom.
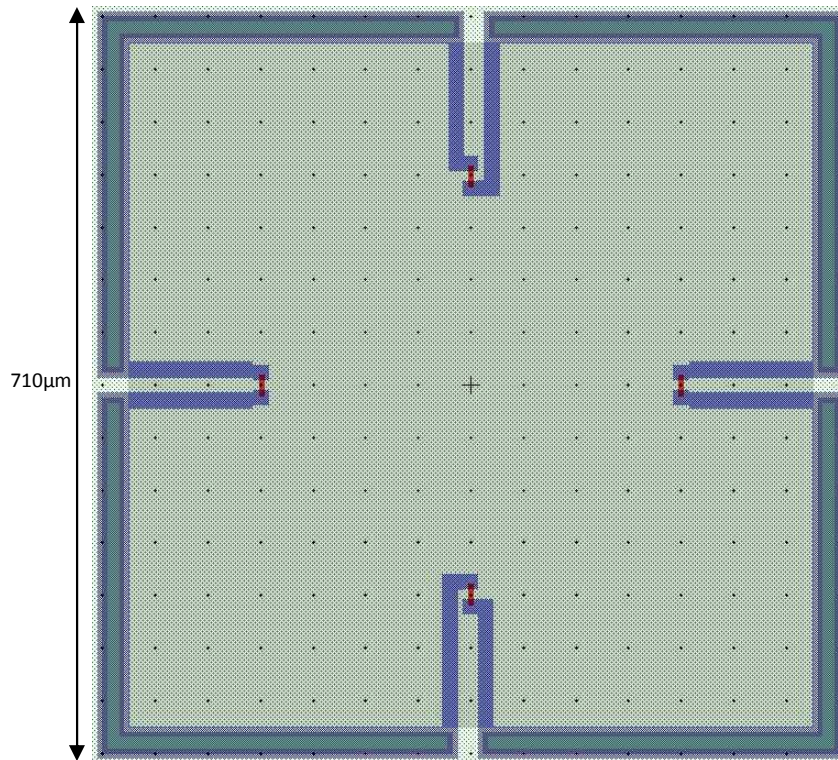
Figure 5.9: Piezoresistor orientation.

The piezoresistors are connected in a Wheatstone bridge configuration by conduction lines made up of surface conductor, buried conductor, metal conductor and contact hole. The membranes themselves are formed by backside etching.

The first mask to be defined was the N-well mask. The N-well region is generally used as a substrate for buried conductor and resistors. In this design, the region was used as a substrate for the conductor lines and to create a thick membrane. The N-well was formed by surface implantation with silicon oxide as the mask layer combined with diffusion and re-oxidation processes. As it has straight polarity a positive image was transferred to the oxide layer and so the region to be free of N-well was drawn. In the thin membrane design, an N-well mask was therefore drawn over the area to be backside etched so that the etching process would occur anisotropically through the silicon substrate to the epitaxial layer. The N-well was required to define the thick membrane and is required for electrical connection to the piezoresistors in both designs so no N-well mask was necessary in the design of the thick membrane.

123

Figure 5.10: Mask layout of conduction lines from piezoresistors on the cap deflection membrane to chip bond pads.

The p-type buried conductor mask was then defined to create electrical connections from the piezoresistors to the chip bond pads. Buried conductor was necessary to make the electrical connection from inside the anodically sealed cavity to the bond pads out with this cavity. Figure 5.10 shows the buried conductor mask as the light blue regions making connections from the conduction lines to the bond pads. The buried conductor layer was formed by surface implantation using photoresist as the mask, followed by a diffusion process. The buried conductor mask had negative polarity and so the mask was drawn in regions where the buried conductor was to be implanted.

The surface conductor mask was then defined again to complete the electrical connection from the piezoresistors to the bond pads. Surface conductors are formed inside the epitaxial layer by implantation through the thin oxide using photoresist as a mask followed by a diffusion process. The surface conductor mask had negative polarity so was drawn only where the surface conductor was to be implanted. The surface conductor mask is drawn along the same conduction lines as the buried conductor and represented in figure 5.10 by the purple region. As all the masks are stacked along the conduction lines within the cavity area, the buried conductor, surface

conductor and metal conductor masks have the same dimensions and are all represented by the purple region.

The piezoresistors were surface resistors orientated along the <110> crystallographic direction and connected at either end to surface conductor regions as shown in figure 5.8. The surface resistor was formed inside the epitaxial layer by implantation through the thin oxide using photoresist as the mask followed by a diffusion process. The surface resistor mask had negative polarity so was drawn only where the surface resistors were required, represented by the red regions in figure 5.9.

Contact holes were then defined to allow electrical contact from the silicon through the thin oxide to the metal conductor, which was to be deposited on top of the surface conductors. The contact holes were opened using a wet etch process with a photoresist mask. The mask had negative polarity so was drawn only where the thin oxide was to be etched and represented by the black region in figure 5.10.

The metal conductors were sputtered and then patterned using a wet etch process and photoresist mask. The mask had positive polarity so the metal conductor mask was drawn only where the metal should not be etched, i.e. along the conduction lines connecting the piezoresitors to the bond pads. The metal conductor mask is represented by the purple region in figure 5.10.

The backside etch mask was defined to create the thin and thick membranes. The backside etch was done using wet anisotropic bulk silicon etching and an electrochemical etch stop technique. The two bond pads not connected to conduction lines by the buried conductors in figure 5.10 were used to perform the electrochemical etch stop technique. The {111} crystallographic plane was etched most slowly and these planes are inclined at 54.74° with respect to the {100} plane, the nominal surface plane as shown in figure 5.11. Therefore the mask had to be designed with care to ensure that the final membrane size was correct. The backside etch mask had negative polarity so the region to be etched was defined.
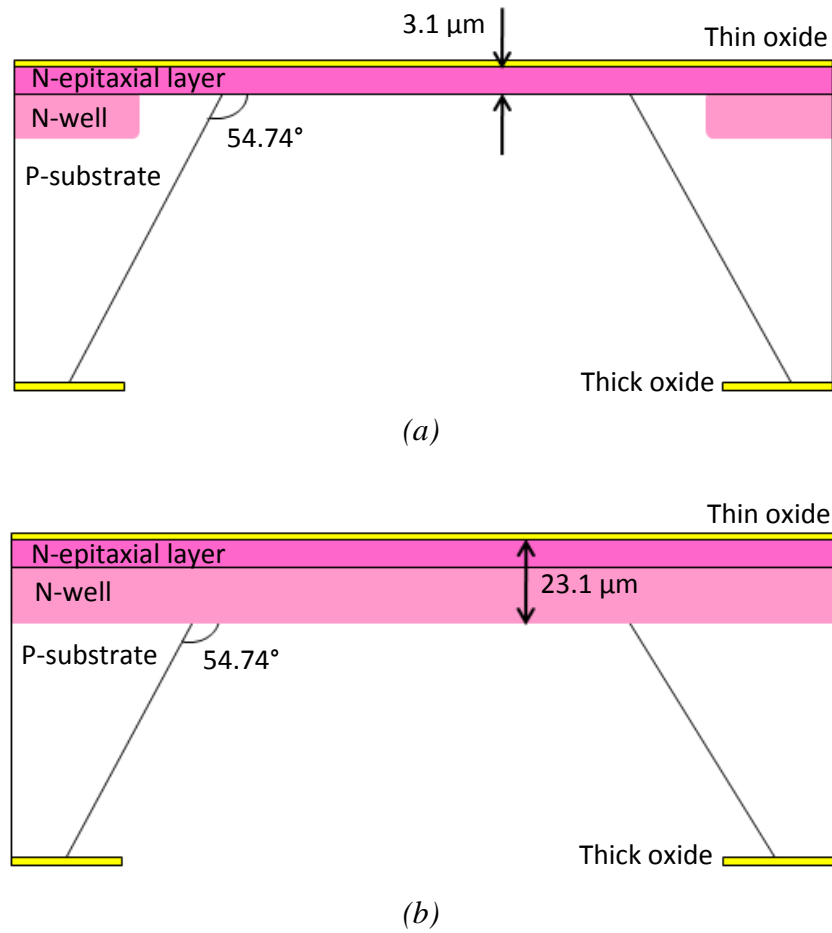
3.1 µm

Thin oxide

N-epitaxial layer

N-well

54.74°

P-substrate

Thick oxide

(a)

Thin oxide

N-epitaxial layer

N-well

23.1 µm

P-substrate / 54.74°

Thick oxide

(b)

Figure 5.11: Backside etch of silicon for (a) thin and (b) thick membranes

The anodic bonding mask was defined around the area covering the cap deflection test structures and the conduction lines. This mask was used to define the region where the thin oxide layer will not be removed by a wet etch process. Anodic bonding would only occur where the thin oxide was removed. The mask has positive polarity so was drawn over the cap deflection test structure to ensure bonding would not take place in this area. During this process, the backside of the silicon wafer was also etched so that the bottom glass could be bonded to the silicon as well. The top glass was etched before bonding to provide a cavity over the cap deflection test structure. The bottom glass had through-holes etched to allow access to the internal cavity for calibration purposes.

The 23.1 µm thick membrane includes the N-well layer whereas the 3.1 µm thin membrane design includes a mask layer defined to remove the N-well. Taking the anisotropic etch into consideration, the backside etch mask in the design of the thick membrane was defined as a square with 2034 µm long sides and the membrane created had sides of 1468 µm in length. The backside etch mask in the design of the thin membrane had 964 µm long sides and the membrane created had 398 µm long sides.

The area of the membranes were therefore well within the limits of the MultiMEMS design rules.

In order to ensure the design meets the rules set by the fabrication processes, the design was checked using a design rule checker. Once the design had passed the check, a simulation of the most stress sensitive areas of the structure was required. The maximum tolerable stress was 500×10^6 N/m^2 [5.7]. Figures 5.12 and 5.13 show the maximum stress in the thin and thick cap deflection test structures were 508.792 MPa and 449.859 MPa, respectively. The stress in the thick membrane did not exceed the maximum tolerance given by MultiMEMS and maximum stress in the thin membrane was less than 10% over the tolerance and localised. The designs therefore passed the design rule checker and so were accepted for fabrication.
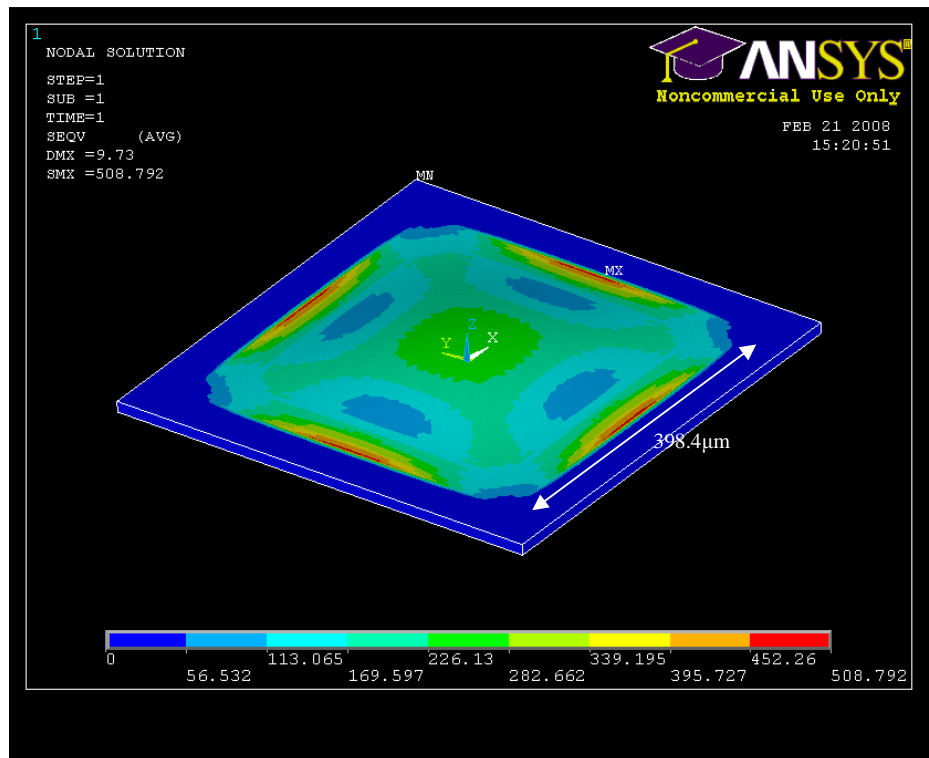
Figure 5.12: ANSYS simulation of stress in design of thin cap deflection in situ test structure.

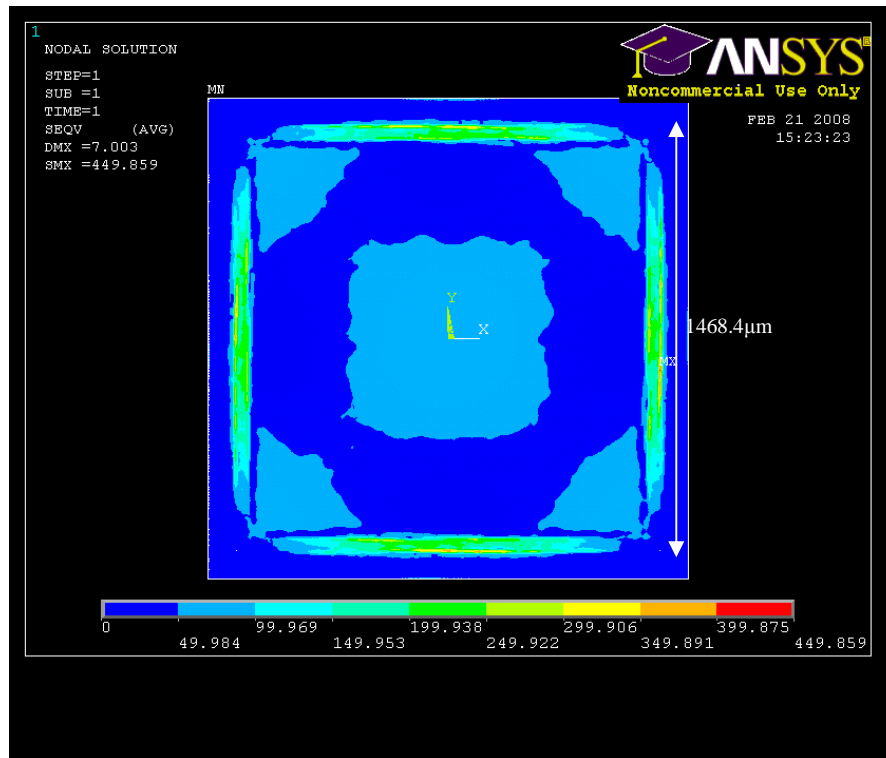*Figure 5.13: ANSYS simulation of stress in design of thick cap deflection in-situ test structure.*
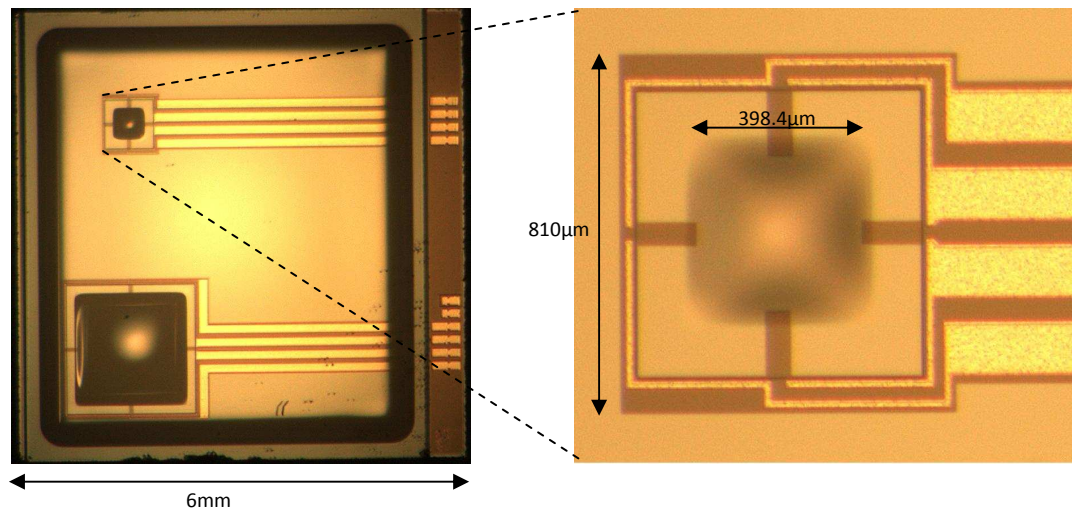

Figure 5.14: Microscope photographs of fabricated cap deflection test structure.

Figure 5.14 shows the deflection of the cap under atmospheric conditions. The membrane is deflected into the vacuum packaged cavity contained in the top glass through which the photographs in figure 5.14 have been taken.

5.4 Experimental design for calibration

In order to calibrate the in-situ test structures, holes in the bottom glass layer of the chips were made to allow access to the package cavity, preventing thereby the die to be wirebonded onto conventional ceramic chip carriers. In order to allow electrical connection to the die, a flexible polyimide substrate coated with a 17.5 µm thick layer of copper was used. The flexible copper clad substrate was patterned by printing an electrode design directly onto the copper using a conventional 1200 dpi laser jet printer, figure 5.15.
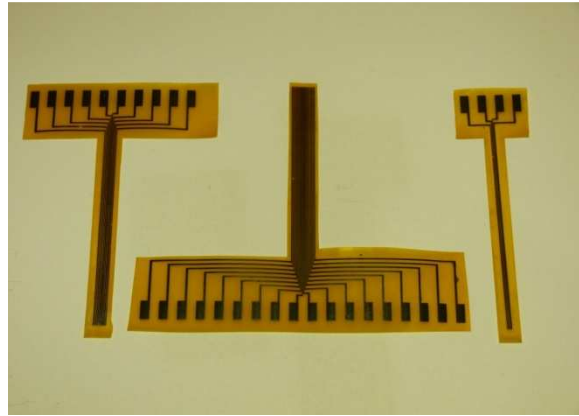
Figure 5.15: Electrode pattern printed onto copper cladded polyimide; large pads: 2 x 4 mm; central lines: 150 µm x 5 cm; central line spacing: 150 µm.

After etching in ferric chloride, the ink was removed using solvent and the structure cut from the polyimide substrate. The flexible substrate was then glued using high temperature epoxy onto the top glass of the die before wirebond connections were made from the aluminium die pads to each electrode. It is very challenging to achieve strong gold bonds on copper because copper oxidises quickly. It is extremely difficult to break through the oxide layer using the full ultrasonic power of the wire bonder. For this reason, a few nanometers of gold were electroplated onto the tips of the copper where the wirebonds were to be placed, as shown in figure 5.16.
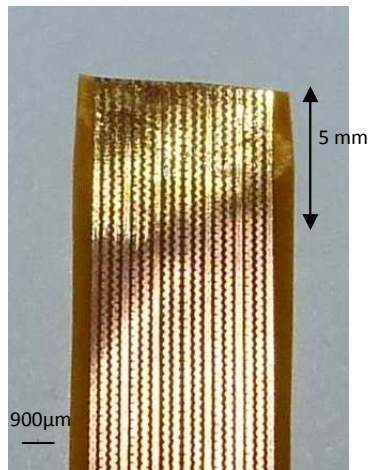
Figure 5.16: Electroplated gold on copper tracks for wirebonding purposes

Nickel is usually plated onto copper prior to the plating of gold onto nickel to prevent an alloy of gold and copper being formed as copper diffuses into the gold. This step was neglected here as this process was simply used to minimise copper oxidation to achieve strong wirebonds onto the electrode tracks. To minimise costs, a small amount of gold plating solution was purchased and the gold was electro-deposited using the following painting technique. All tracks were shorted together using a sheet of copper film and a clamp. The tracks were then connected to the cathode and a graphite stick connected to the anode. The graphite stick was tipped with cotton to absorb the plating solution, which was 'painted' onto the end of the copper tracks which had been thoroughly cleaned to remove the oxide layer, as shown in figure 5.17.

Figure 5.17: Electroplating set-up.

When wirebonding, it is standard practise to create the first bond, a ball bond, on the die pad, then to create the second bond, a wedge bond, onto the chip carrier, PCB or in this case, the copper electrodes. As the electrode tracks lie on top of a polyimide flexible substrate, it was difficult to wirebond onto them as the substrate absorbs the ultrasonic power from the wirebonder. Creating a wedge bond on the electrodes was therefore not possible. The thin layer of gold electroplated onto the copper electrodes was enough to stop the copper oxidising and to allow gold ball bonds to be deposited onto the tracks. Once these balls were created, the wire was broken away from the ball leaving a gold ball on the gold electroplated copper track. Another ball bond was then made on the corresponding die pad then the second wedge bond was made on top of the gold ball previously placed on the electrode as shown in figure 5.18.
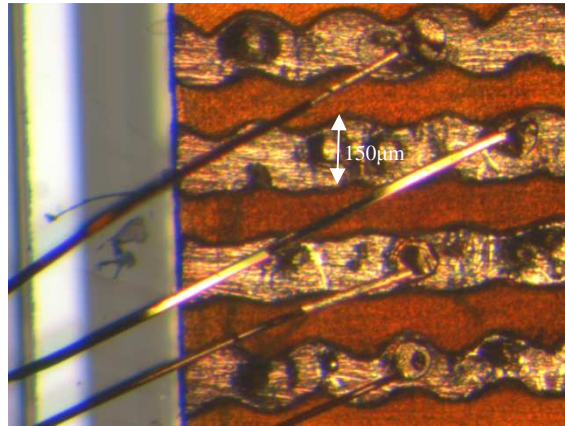
Figure 5.18: Wedge bond on top of gold ball previously bonded to the gold electroplated copper electrode.

After wirebonding the bonds were encapsulated using an epoxy resin to prevent the wirebonds being broken during handling. Once the electrical connection was made the test structures were then calibrated. The die and electrodes were placed inside a chamber to be pumped down to the lowest vacuum possible, 9.87×10^{-9} atm, using the Leybold PT50 Turbotronik NT10 pump. The chamber used for this purpose was made by modifying a standard vacuum pump adaptor. Holes were drilled into a standard cap and electrical wires sealed into these holes as shown in figure 5.19. The wires were soldered to the copper tracks on the polyimide substrate, shown in figure 5.19, completing the electrical connection from the small die to the large scale. The modified cap was fixed to the vacuum pump using a standard O-ring.
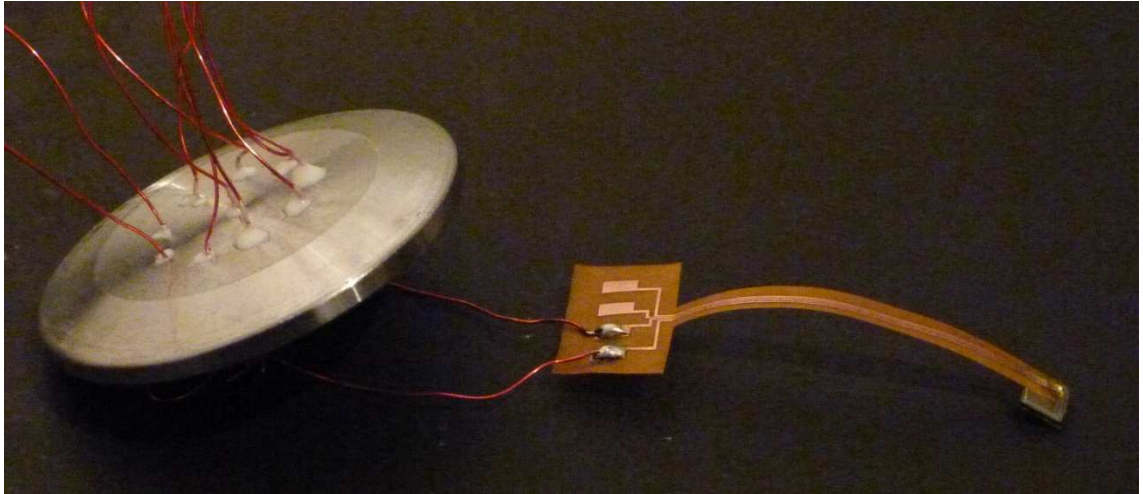
Figure 5.19: Large scale electrical connection to die.

Figure 5.20 shows the calibration set-up. On the other side of the modified cap, the electrical wires were connected to the test circuitry, which monitored the change in the test structures electrical output with pressure. A pressure sensor, either a Penning Gauge or a Pirani Gauge, was used to monitor the pressure inside the test chamber. The leak valve was used both to increase the pressure from initial vacuum conditions inside the chamber during calibration and to ensure the pressure was kept constant during measurements since the vacuum pump was continually evacuating the chamber.

(a)

132

Leak Valve

Test circuitry

Power supply

Pressure Sensor

Vacuum pump
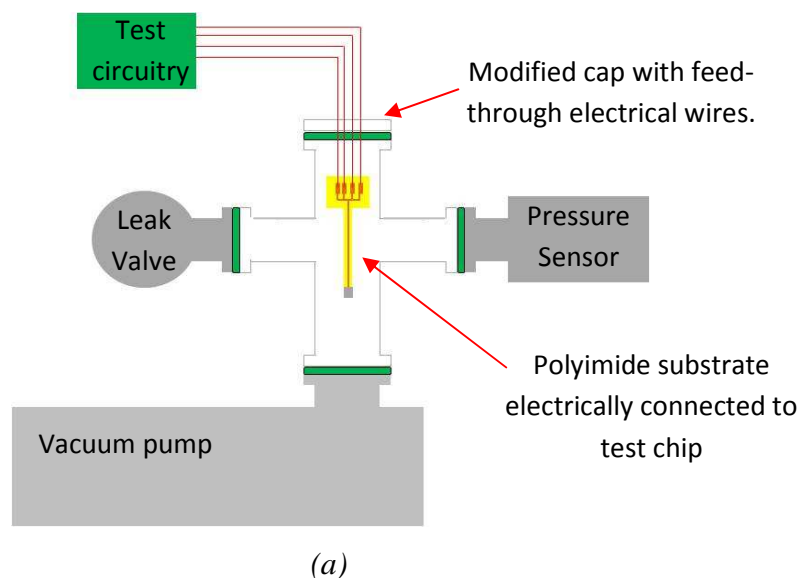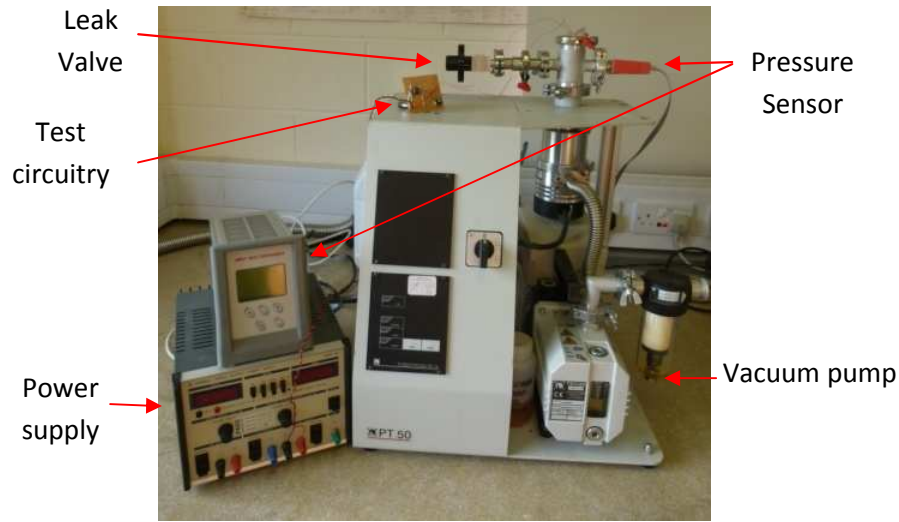
(b)

Figure 5.20: (a) Schematic, (b) experimental set-up for in situ test structure calibration.

5.5   Calibration procedure

The calibration procedure for the cap deflection test structures was straightforward. As the piezoresistors were connected in a Wheatstone bridge on chip, all that was required was a supply voltage and the change in bridge voltage was recorded as the pressure surrounding the chip was changed. The pressure was reduced to below 1×10^{-8} atm and the bridge voltage recorded. The pressure was then slowly increased using a leak valve and the change in bridge voltage was recorded. Pirani and Penning gauges were used to monitor the vacuum chamber pressure. The cap deflection structures were sensitive at near atmosphere where the Pirani gauge used to monitor the vacuum chamber pressure was reaching the end of its operating range.   To calibrate the structures at near atmosphere, small pressure sensors giving an electrical response to changing pressure were incorporated inside the vacuum chamber.

The measured data was used to plot graphs of dimensionless output, differential output pressure divided by the reference supply voltage, as a function of differential pressure defined as the difference of pressure between the chamber and the internal cavity. The internal cavity pressure should have been approximately 0.049 atm according to the design rules. The internal pressure however was determined by varying the chamber pressure until the output bridge voltage reached zero. At this pressure, the membrane was flat and the pressure inside the cavity equalled the pressure in the chamber. This

133

value was subtracted from the chamber pressure to obtain an accurate value of differential pressure.

5.6   Results

Figures 5.21 and 5.22 show the average results of both the thin and thick membranes on two cap deflection test chips. The errors bars reflect the maximum and minimum results of three test runs conducted for each membrane on each chip.

The figures show that the response of the thin membrane is linear when the differential pressure is greater than 0.1 atmosphere. The thick membranes response is linear when the differential pressure is greater than 0.45 atm, therefore the operating range of the thick membrane is narrower. The plots also show that the chip-to-chip output variations of both the thin and thick membrane were small. The cap deflection design is therefore ideal for use as a test structure.
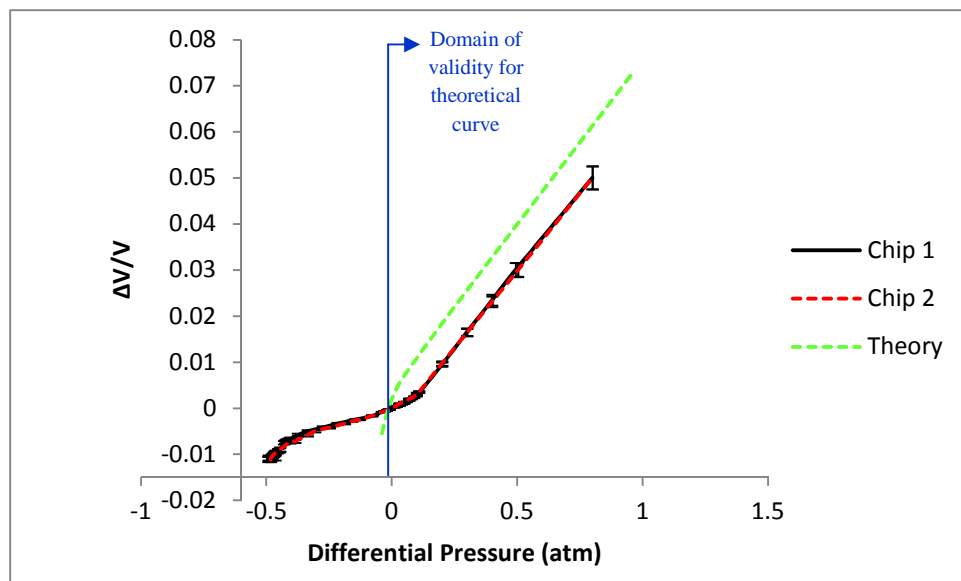

Figure 5.21: Thin membrane average differential output voltage as a function of differential pressure.
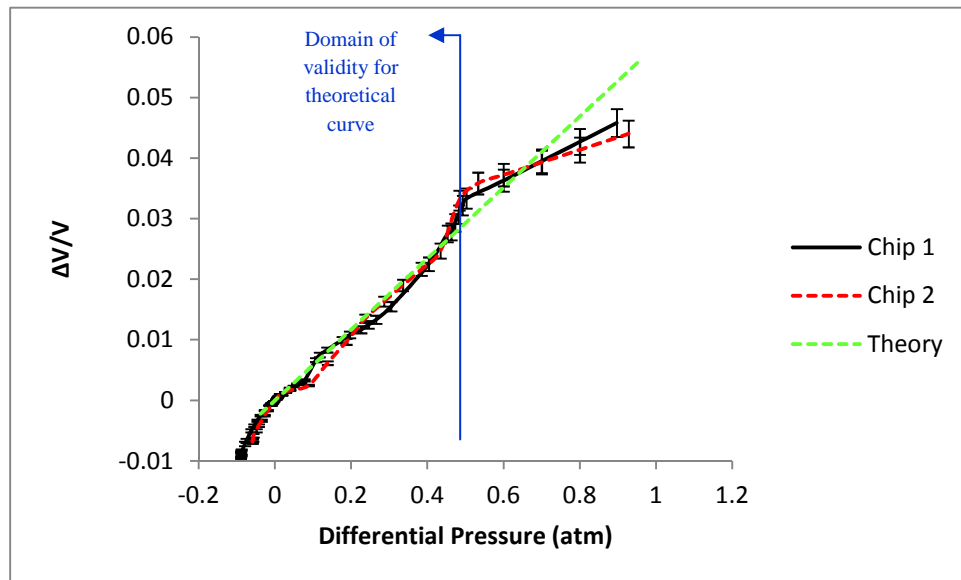
Figure 5.22: Thick membrane average differential output voltage as a function of differential pressure.

The sensitivities of the average results of the thin and thick membrane were calculated in the region where output is linear. It was found that the average sensitivity of the thin and thick membranes were 65.2 mV/V.atm and 47.5 mV/V.atm, respectively. These results show that, as expected from the ratio of membrane thickness to membrane length, the thin membrane was most sensitive. The theoretical calculations agree with this result although the calculated sensitivity values are slightly higher, 72.2 mV/V.atm and 58.6 mV/V.atm, respectively.

The thin membrane experimental results are in agreement with the theoretical results as shown in figure 5.21, showing that output is linear when the differential pressure is greater than zero. However, the dimensionless output voltage values of the theoretical results are slightly displaced from those obtained experimentally. This could be caused by inaccurate piezoresistor placement. The manufacturing process is however well established and it is unlikely that a significant error in piezoresisor positioning could be made. Another possible reason for this inconsistency could be inaccurate measurement of the differential pressure during experimental measurements. Since the calibration of the thick membrane was done in the same way and these results are not displaced from the theoretical values in the same way, it is unlikely that this caused the difference in theoretical and experimental results. However, it is possible that the cavity pressure which was quoted by the manufacturer to be 0.049 atm does not precisely match the actual cavity pressure. The use of the given cavity pressure in the theoretical results to

135

calculate the differential pressure is therefore incorrect and causes the offset from the experimental results of the thin membrane.

The experimental results of the thick membrane show some deviation from the theoretical curve as the differential pressure is increased. The analytic expressions given in the theory here are only accurate for deflections, which satisfy $w \leq 0.2h$, where w is deflection and h is the thickness of the membrane. The theory should therefore be accurate for deflection at the centre of the membrane up to 4.62 μm [5.6]. Above 0.6 atm, 2μm deflection at the piezoresistor location, (0, L/8), according to figure 5.5, the experimental curve begins to deviate from the theoretical curve at this pressure. The central deflection of the membrane is there greater than 4.62 μm and so it is expected that the experimental curve will deviate from the theoretical curve.

Given a typical cavity size of 1×10^{-5} cm^3 and assuming that the package will be stored in ambient conditions, it is possible for this test structure to measure a leak rate as low as 6.94×10^{-12} atm.cm^3.s^{-1} over an hour without a bombing procedure. Using an accelerated testing technique, it would be possible to measure this leak rate over a shorter time or indeed to measure a lower leak rate. The value of this lower leak rate is dependent on the bomb pressure and time used. A more sensitive cap deflection design would allow lower leak rates to be measured in a time suitable for use in industry for ultra high vacuum packaging applications. It may be possible to increase the sensitivity of the cap deflection test structure by placing the piezoresistors on an area of the membrane which is more stressed, for example at the edges on the membrane as shown in the ANSYS plots given in figures 5.12 and 5.13.

5.7   Conclusions and Future work

The results of the piezoresistive cap deflection test structure have proved that for some low volume applications this type of test would offer a cheap hermeticity test method provided that double cap packaging can be carried out. The test structure itself does not occupy any real estate and requires only four piezoresistors to be fabricated on the silicon cap. In a device where silicon fusion bonding or anodic bonding are used to hermetically seal packages, this test structure does not add to the fabrication steps of the device or change of the packaging method.

Future work concerning this in situ test structure includes testing and pushing both the detection range and detection sensitivity. At present, this method is not sensitive enough for some ultra low vacuum packages without the need for a long bomb time or high pressures which could potentially interfere with the test results. Future work would also include incorporating this in-situ test structure into a suitable prototype package to determine the ease and speed of use for industrial applications.

5.8   References

[5.1]   F. Gueissaz, *'Ultra low leak detection method for MEMS devices'* 18th IEEE Conference on Micro Electro Mechanical Systems, pp 524-527, 2006.

[5.2]   P.J. van der Wel, J. Stulemeijer, J.A. Bielen, F.G.A. Theunis, A. den Dekker, M.A.J. van Gils and R.J. Havens, *'Hermeticity testing of capacitive RF MEMS switches'*, IEEE CFP08RPS-CDR 46th Annual International Reliability Physics Symposium, Phoenix, 2008.

[5.3]   Fraunhofer ISIT, '*Hermeticity Testing of Vacuum-Sealed Microresonators*', Fraunhofer ISIT Achievements and Results Annual Report 2006, (http://www.isit.fraunhofer.de/german/download/JB2006A4.pdf) (11/09/2009).

[5.4]   W. Reinert, D. Kahler, M. Oldsen, and P. Merz, *'In-line Critical. Leak Rate Testing of Vacuum-Sealed and Backfilled Resonating. MEMS Devices'*, 8th International Symposium on Semiconductor Wafer Bonding, pp. 1-6, 2006.

[5.5]   A.J. Pang and M.Y.P. Desmulliez, *'Modelling and simulation of a silicon micro-diaphragm piezoresistive pressure sensor using Finite Element Analysis (FEA) tools'*, Proceeding of MEMS Design, Fabrication, Characterization, and Packaging, SPIE 4407, 327, 2001.

[5.6]   H.E. Elgamel, *'Closed form expressions for the relationships between stress, diaphragm deflection, and resistance with pressure in silicon piezoresistive pressure sensors'*, Sensors and Actuators A, 50, pp. 17-22, 1996.

[5.7]   D. Lapadatu, *'MultiMEMS design handbook version 4.1'*, Infineon Technologies SensoNor AS, 2007.

Chapter 6

Other in-situ test structures for the electrical measurement of the internal cavity pressure

6.1   Introduction

This chapter describes the theory, design and calibration of two in-situ test structures: a micro-Pirani test structure and a thermal van der Pauw test structure. The Pirani gauge is a well known pressure sensor and the device has previously been miniaturised and used to assess the hermeticity of low cavity volume MEMS [6.1, 6.2, 6.3]. The thermal van der Pauw structure is the thermal equivalent of the electrical Greek cross test structure and is used to measure the thermal sheet conductivities of thin films [6.4]. The thermal van der Pauw structure must be used in a vacuum to ensure thermal isolation [6.4]. For this reason it was thought that this test structure could also be used as a pressure sensor for sensitive hermeticity testing. Comparison of the performance of these sensors is also provided with other in-situ test structures.

6.2   Micro-Pirani test structure

6.2.1   Theory

The micro-Pirani gauge provides a measurement of the pressure inside a cavity for pressure values ranging from high vacuum to atmospheric pressure. The sensor is usually made of a free-standing metallic filament or beam surrounded by a cavity, the pressure of which is to be measured. The free-standing structure is heated through the application of a current passing through it. At thermal equilibrium, the power provided by the Joule effect is equal to the power losses caused by radiation, conduction through anchors of the beam, or by convection through the gas contained in the cavity. The micro-Pirani gauge is designed to monitor heat power loss through convection. Since this power loss is dependent on the pressure of the ambient gas, the micro-Pirani gauge can be used to determine the cavity pressure. Two monitoring strategies are possible:

   (1) Constant current supply: when equilibrium is established, the beam or filament will reach an equilibrium temperature and, therefore, a constant resistance, which is a function of the pressure within the cavity.

(2) Constant temperature monitoring: power is supplied to the beam to keep the temperature hence resistance of the beam constant using feedback control. At equilibrium, the power supplied to the gauge to maintain the beam temperature constant is a function of the cavity pressure.

To derive the physical relations between pressure, resistance and temperature behind the operation of the micro-Pirani, the first mode of operation is described. At thermal equilibrium, consider the temperature of the beam, T_b, to be uniform and the gas, cavity and anchors to be at the same temperature, T_c. The power exchanged by the convection, P_1, from the beam to the gas present in the cavity is given by:

$$P_1 = bp_c(T_b - T_c)$$ (6.1)

where p_c is the pressure of the gas in the cavity and b is a constant that depends on the beam geometry and material. The power exchanged by conduction, P_2, between the beam and anchors is given by:

$$P_2 = a(T_b - T_c)$$ (6.2)

where a is a constant depending on the beam and anchor geometry and material. The power radiated initially by the beam, P_3, is given by:

$$P_3 = c\sigma\left(e_b T_b^4 - e_c T_c^4\right)$$ (6.3)

where c is a constant dependant on the beam geometry and material, σ is the Stefan's constant, e_b and e_c are the emissivity of the beam and cavity, respectively. The resistance of the beam, in the first order, is given by:

$$R_b = R_0\left(1 + \alpha(T_b - T_0)\right)$$ (6.4)

where R_b is the resistance of the beam, R_0 is the initial resistance of the beam before current is applied, α is the temperature coefficient of resistivity and T_0 is the initial temperature of the beam. Neglected here is the fact that the temperature coefficient of

resistivity is itself temperature dependent and that the resistivity will change with the distance from the anchor. At thermal equilibrium, when a constant current, I, is applied:

$$P_1 + P_2 + P_3 = I^2 R_b \qquad (6.5)$$

But:

$$R_b = R_0\left(1 + \alpha(T_b - T_0)\right) = R_0\left(1 + \alpha(T_c - T_0)\right) + R_0\alpha(T_b - T_c) \qquad (6.6)$$

and,

$$R_b = R_c + R_0\alpha(T_b - T_c) = R_c\left(1 + \frac{R_0}{R_c}\alpha(T_b - T_c)\right) \qquad (6.7)$$

where R_c is the resistance of the cavity defined as the resistance when the temperature of the beam equals the temperature of the cavity environment. Setting $\alpha' = \alpha R_0/R_c$ gives:

$$R_b = R_c\left(1 + \alpha'(T_b - T_c)\right) \qquad (6.8)$$

Substituting in equations 6.1, 6.2, 6.3 and 6.8 gives:

$$(a + bp_c)(T_b - T_c) + c\sigma\left(e_b T_b^4 - e_c T_c^4\right) = I^2 R_c\left(1 + \alpha'(T_b - T_c)\right) \qquad (6.9)$$

Micro-Pirani gauges work in the molecular regime where the Knudsen number is greater than 0.01 and heat convection is pressure dependent [6.1, 6.2]. The Knudsen number is calculated by dividing the mean free path of the gas by the smallest dimension through which the gas flows [6.1, 6.2]. Thermal impedance is a measure of how much a materials temperature will change when a heat power is applied. Figure 6.1 shows the pressure dependence of the thermal impedance in the molecular, transitional and continuum regimes, defined by the Knudsen number [6.1, 6.2]. Thermal impedance is pressure dependent in the molecular regime.
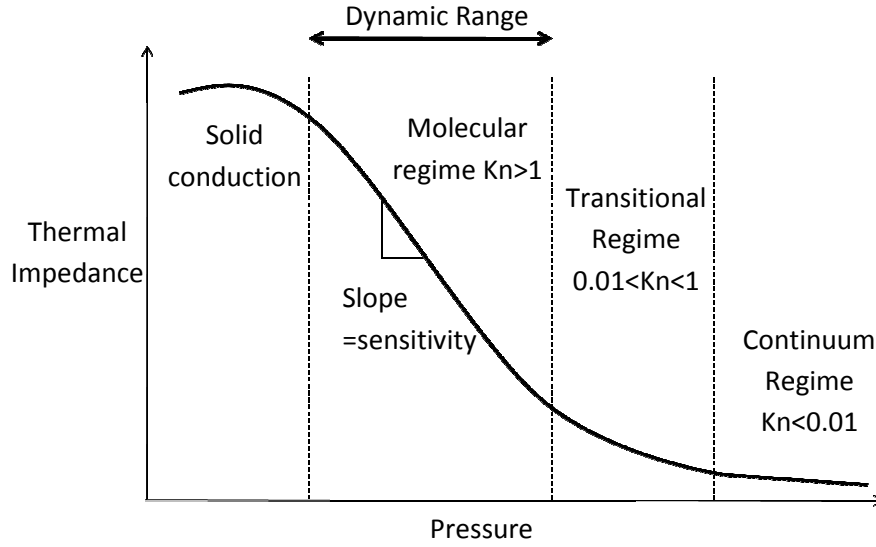
Figure 6.1: Thermal impedance as a function of pressure.

In the molecular regime, radiation losses can be neglected when compared to convective losses. So equation 6.9 becomes:

$$\left(a+bp_c\right)\left(T_b - T_c\right) = I^2 R_c\left(1 + \alpha'\left(T_b - T_c\right)\right) \tag{6.10}$$

Rearranging gives:

$$T_b - T_c = \frac{I^2 R_c}{a + bp_c - \alpha' R_c I^2} = \frac{I^2 R_c}{a + bp_c - \alpha R_0 I^2} \tag{6.11}$$

Therefore equation 6.8 becomes:

$$R_b = R_c\left(1 + \frac{\alpha R_0 I^2}{a + bp_c - \alpha R_0 I^2}\right) \tag{6.12}$$

Substituting $\kappa = \alpha R_0 I^2$ gives:

$$R_b = R_c\left(1 + \frac{\kappa}{a + bp_c - \kappa}\right) \tag{6.13}$$

When a constant current is applied, the voltage measured across the beam, $V_{measured}$, will be:

141

$$V_{measured} = IR_b = IR_c \left(1 + \frac{\kappa}{a + bp_c - \kappa}\right) \qquad (6.14)$$

Using a Wheatstone bridge arrangement to extract the change in beam resistance means the constant term, IR_c, in equation 6.14 can be neglected as the electrical circuitry measures the change of voltage. The voltage sensitivity of the micro-Pirani, S_{MP}, can be determined by dividing the change in the measured voltage by the change in cavity pressure as shown in equation 6.15.

$$S_{MP} = \frac{dV}{dp_c} = \frac{-bIR_c\kappa}{(a + bp_c - \kappa)^2} \qquad (6.15)$$

As the cavity pressure, p_c, approaches ambient atmosphere, the sensitivity of the micro-Pirani gauge decreases. This indicates that the micro-Pirani test structure is best suited to monitor the hermeticity of vacuum packaged MEMS devices. However, when p_c is small and the term bp_c no longer dominates the denominator of equation 6.15, the micro-Pirani will not be operating in the molecular regime and heat transfer is pressure independent so the test structure is outside its range of operation.

When the second monitoring strategy is used, the measured voltage change will reflect the change in power, hence current, required to maintain the constant resistance of the beam. A balanced Wheatstone bridge is used to ensure that the micro-Pirani resistance, hence temperature, is kept constant.

Now considering equation 6.5 under the constant temperature monitoring strategy, R_b is constant and I is variable so that:

$$(a + bp_c)(T_b - T_c) = I^2 R_b \qquad (6.16)$$

neglecting any contribution of radiation. Since the beam resistance is constant so too is the temperature difference of the beam and the cavity, $(T_b - T_c)$. Renaming the temperature difference of the beam and the cavity, ΔT, to avoid confusion, equation 6.16 becomes:

$$\left(a + bp_c\right)\Delta T = I^2 R_b \tag{6.17}$$

Rearranging gives:

$$I = \sqrt{\frac{(a + bp_c)\Delta T}{R_b}} \tag{6.18}$$

The current supplied to the beam will therefore decrease to keep the beam resistance hence temperature constant as the pressure in the cavity is reduced and heat convection from the beam to the surrounding gas in the cavity is reduced.

The voltage measured is related to this current by Ohm's law such that:

$$V_{measured} = \sqrt{R_b(a + bp_c)\Delta T} \tag{6.19}$$

The voltage sensitivity of the micro-Pirani, S_{MP}, can be determined by dividing the change in the measured voltage by the change in cavity pressure as shown in equation 6.20.

$$S_{MP} = \frac{dV}{dp_c} = \frac{-R_b b\Delta T}{2\sqrt{R_b(a + bp_c)\Delta T}} \tag{6.20}$$

As the cavity pressure, p_c, approaches ambient atmosphere, the sensitivity of the micro-Pirani gauge decreases. This indicates that the micro-Pirani test structure is best suited to monitor the hermeticity of vacuum packaged MEMS device. However, as with constant current strategy, when p_c is small and the term bp_c no longer dominates the denominator of equation 6.20, the micro-Pirani will not be operating in the molecular regime and heat transfer is pressure independent so the test structure is outside its range of operation.

6.2.2   Design

In order to increase its sensitivity, the micro-Pirani was designed with a long resistive meander. The design of this structure is shown in figure 6.2.
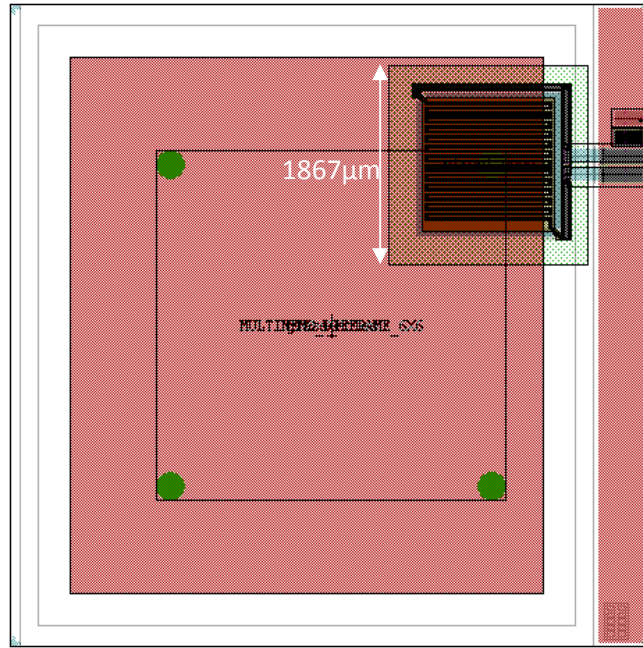
Figure 6.2: Design of the micro-Pirani in-situ test structure on chip.

Figure 6.2 shows the layout of the 6 mm x 6 mm chip, which has one micro-Pirani located in the top right hand corner. The micro-Pirani was fabricated on the silicon layer between the top glass and the bottom glass, the latter of which contained the holes giving access to the internal cavity for calibration of the test structure. Figure 6.3 shows the more detailed design of the micro-Pirani sensor.

Figure 6.3: Design of the micro-Pirani gauge

The first step was to define the regions where the N-well should not be implanted. The N-well region was necessary for most of the design except the areas, which were to be releas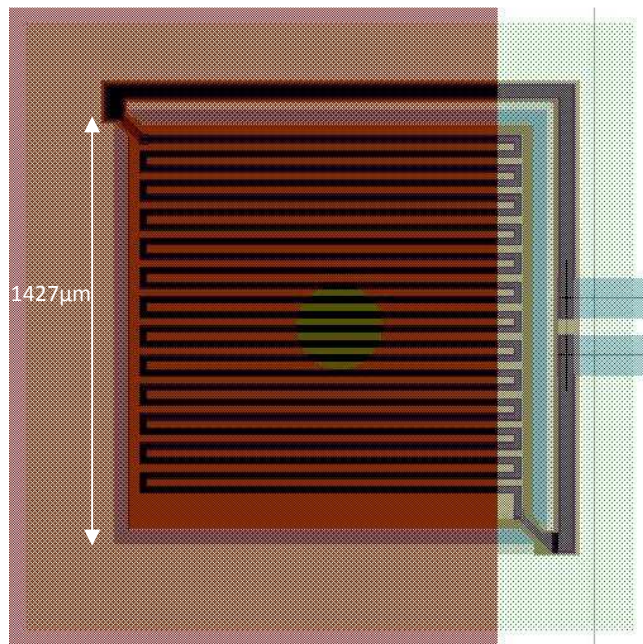ed from the substrate. As it has straight polarity a positive image was transferred to the oxide layer and so the region to be free of N-well was drawn. Figure 6.4 shows the regions where the N-well mask were defined and are represented by the darker colour which forms the outline of a square on which the brighter blue release mask is drawn.
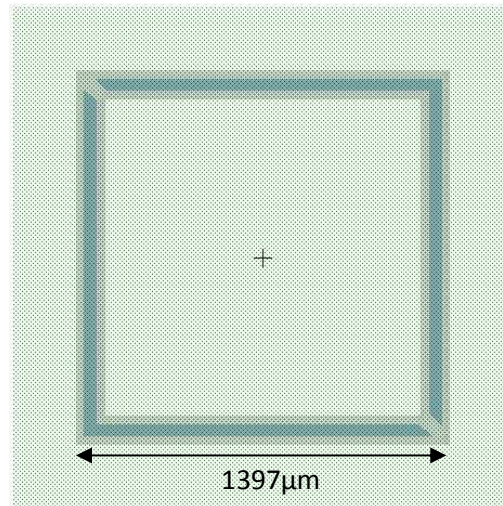

Figure 6.4: N-well and release etch regions of micro-Pirani design.

Next, the mask for the p-type buried conductors was defined. Buried conductors were used in this design to ensure that any spikes in the metal layer would not penetrate the underlying pn-junction. Also, by using the buried conductor, any breaks in the metal line would not result in device failure. The buried conductor mask had negative polarity and so the mask was drawn in regions where the buried conductor was to be implanted. The buried conductor mask was the same size as the surface resistor and metal mask so cannot be seen in figure 6.5 but is represented by the purple regions.

Surface conductors were used in the micro-Pirani design to electrically connect the micro-Pirani device to the bond pads. The use of metal conductors in the top left hand corner and bottom right hand corner, shown in figure 6.3, at 45° would have made the structure very fragile and would have compromised the MultiMEMS design rules. For these reasons surface conductors were used. The surface conductor mask had negative polarity so was drawn only where the surface conductors were required. This mask is represented by the red regions in figure 6.5.

Surface resistors were defined along the lengths of the micro-Pirani meander to increase the resistance of the meander to achieve maximum change in resistance, which would increase the sensitivity of the test structure to changing ambient pressure. The surface resistor mask had negative polarity so was drawn only where the surface resistors were required. In figure 6.5, the surface resistor mask is the same size as the buried conductor mask and the metal mask on the micro-Pirani meander. For this reason the surface resistor mask cannot be seen but is represented by the purple region in figure 6.5.
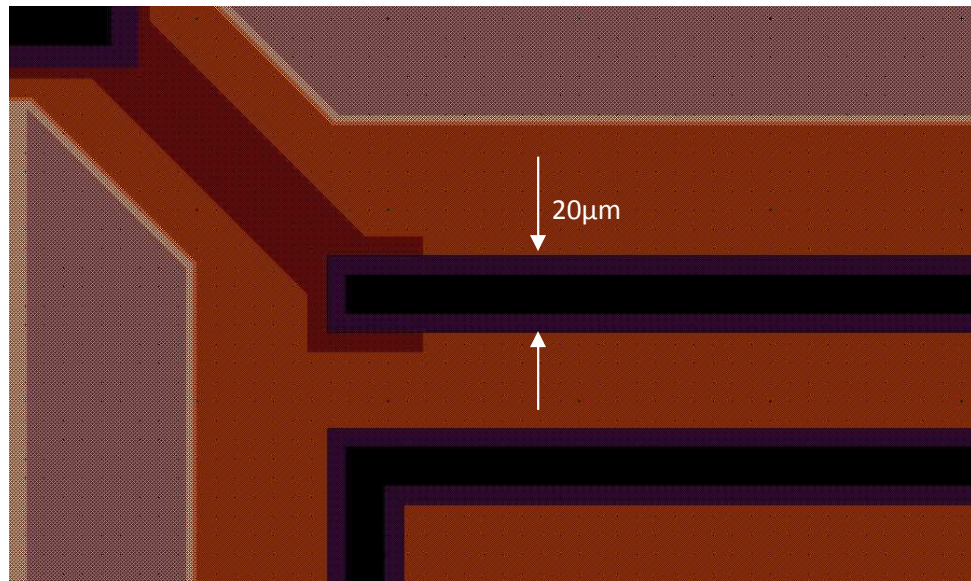
Figure 6.5: Buried conductor, surface resistor, N^+, contact hole, metal layer and anodic bonding masks.

The N^+ layer was used to provide ohmic contact to the epitaxial layer and was defined over the full membrane on which the micro-Pirani meander was designed. The N^+ regions were formed inside the epitaxial layer by implantation through the thin oxide using photoresist as the mask. The N^+ mask was drawn over the area of the membrane on which the micro-Pirani meander was drawn.

Contact holes were then defined to allow electrical contact from the silicon through the thin oxide to the metal conductor. The mask had negative polarity so was drawn only where the thin oxide was to be etched, represented by a black region in figure 6.5.

The metal conductors were sputtered and then patterned using a wet etch process and photoresist mask. The mask had positive polarity so the metal conductor mask was drawn only where the metal was to be present, represented in figure 6.5 by the purple regions.

Next the mask for backside silicon etch was defined. The backside etch mask was defined around the full structure so that the micro-Pirani meander would be on a thick membrane, 23.1 µm, as shown in figure 6.6. The backside etch was carried out using wet anisotropic bulk silicon etching and an electrochemical etch stop technique. The mask had to be designed with care to ensure that the final membrane size was correct. The backside etch mask had negative polarity so the region to be etched was defined.

Thin oxide

N-epitaxial layer

N-well

P-substrate / 57.74°

Thick oxide
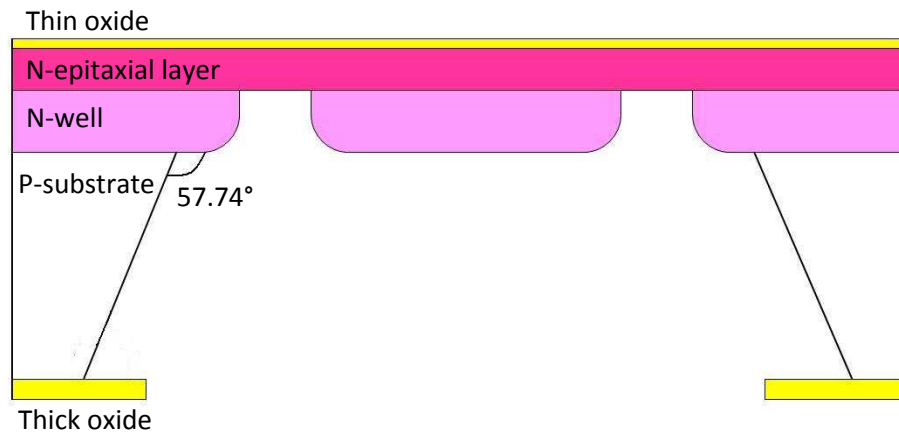
Figure 6.6: Backside etch of silicon for the micro-Pirani design.

The anodic bonding mask was defined around the N^+ region, which covers the micro-Pirani. The mask has positive polarity so was drawn over the test structure to ensure bonding would not take place in this area. The thin oxide on the backside of the silicon wafer was also etched during this step so that the bottom glass was prepared for anodic bonding. The top glass was etched before bonding to provide a cavity over the test structure. The bottom glass had through-holes etched to allow access to the internal cavity for calibration purposes.

Lastly, the release etch mask was defined. Because of the MultiMEMS design rules, it was not possible to release between the arms of the meander structure so the thick membrane on which the micro-Pirani was fabricated was released to minimise

conduction effects through the bulk silicon. It will be explained later that this lack of thermal isolation has provided experimental results that do not follow the theoretical behaviour of the sensor as described above. The release etch process was done using reactive ion etching from the front silicon surface using a photoresist mask. In previous steps, the N-well region, which covers the area of the micro-Pirani had been removed in the region to be released so that the thickness of the membrane in these regions was reduced to the thin membrane thickness of 3.1 µm during the backside etching step. The release etch mask had negative polarity so the regions to be released were drawn, represented in figure 6.4 by the blue region.

Figure 6.7 shows that the maximum stress in the micro-Pirani structures designed was in the connection from the released membrane to the substrate. The maximum stress was 547.437 MPa, which exceeded the maximum allowable stress of the manufacturers, 500×10^6 N/m^2. The design was checked by the manufacturers and accepted since the maximum stress was less than 10% over the limit and in a very localised area.
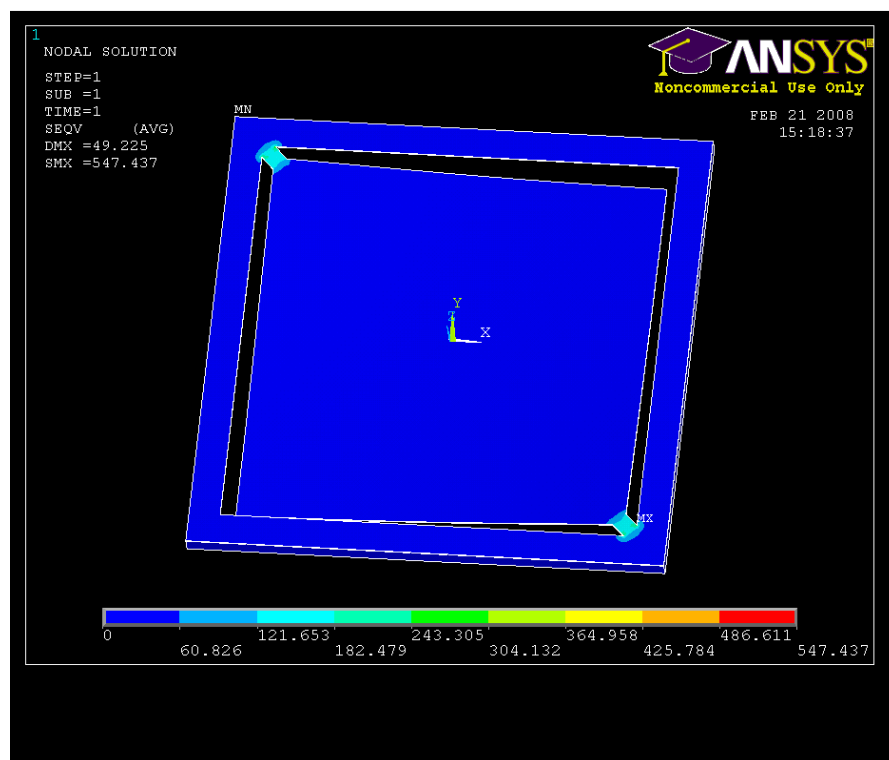

Figure 6.7: ANSYS simulation of stress in design of micro-Pirani in situ test structure.

The micro-Pirani resistive meander was fabricated on a released thick membrane. The fabricated device is shown in figure 6.8. Although the design passed the MultiMEMS

148

design rule checker, there were yield issues with this particular design due to the high stress areas shown in figure 6.7. Many of the micro-Pirani test structures were broken during dicing. All the failures were caused by breaks in the arms connecting the membrane to the substrate. The fragility of the 45° angle of the designed connection to the released membrane was the most probable reason for this. Ten successfully fabricated devices were however delivered by MultiMEMS and were calibrated to determine the structures electrical response to changing ambient pressures for use as an in-situ hermeticity test structure.
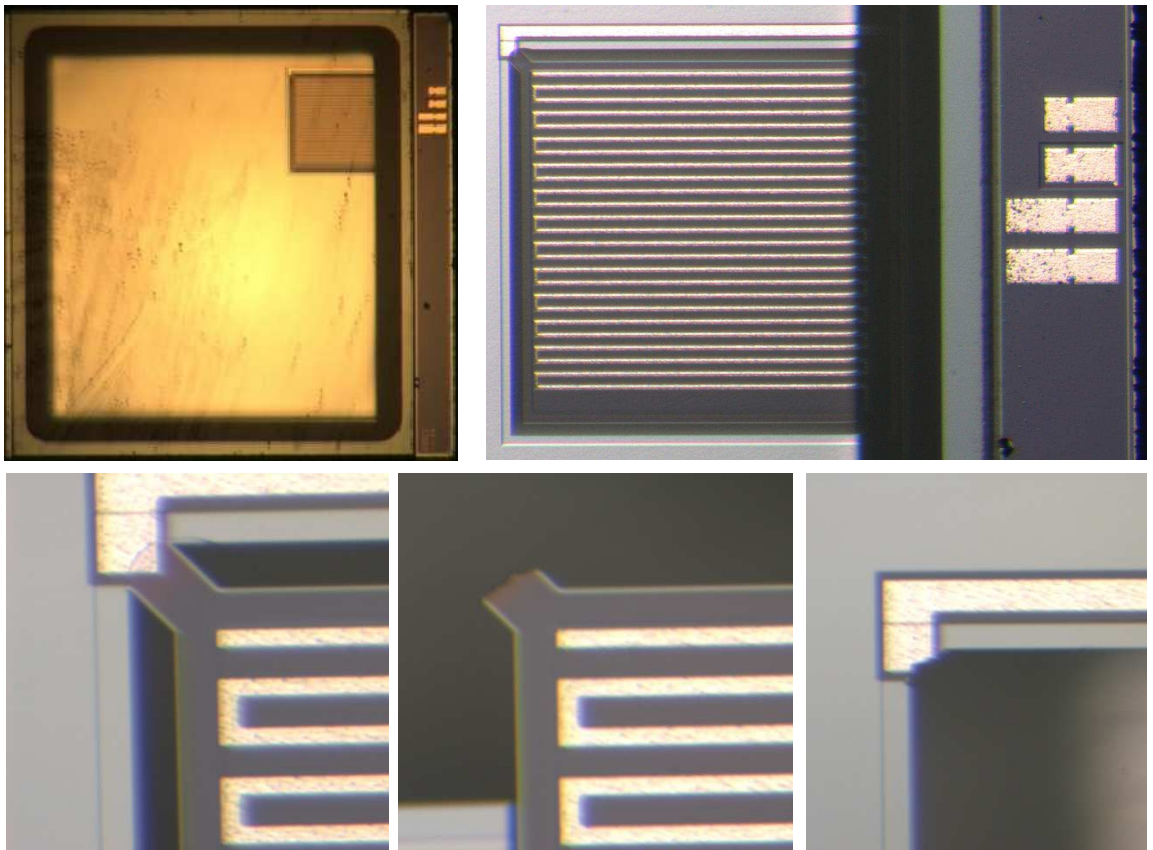
Figure 6.8: (a) and (b) Fabricated micro-Pirani test structure, (c) Connection from substrate to membrane, (d) broken connection on membrane, (e) broken connection on substrate.

6.2.3   Calibration procedure

The resistance of the first micro-Pirani test structure at room temperature in ambient conditions was measured to be 708 Ω. To calibrate the micro-Pirani test structure the bond pads of the chip were wirebonded to copper tracks on a flexible substrate as described in chapter 5. Electrical wires were then soldered to macro scale pads

connected by copper lines on the flexible substrate and via wirebonds to the chip pads. The chip and the flexible substrate were then enclosed within a test chamber as described in Chapter 5. The wires coming from the chamber were used to complete a Wheatstone bridge on a test board. The test board was designed to keep the temperature, hence resistance, of the micro-Pirani constant using a feedback loop, i.e. following the second monitoring strategy. The micro-Pirani gauge was used as one of the resistors in the Wheatstone bridge on the test circuit. Two of the other resistors were fixed and their values are shown in figure 6.9. A variable resistor was used to balance the bridge in atmospheric pressure at room temperature. The resistance of the micro-Pirani at room temperature and pressure varies significantly from chip to chip. To eliminate this error from the calibration results, the three chips chosen for calibration were of similar resistances ranging from 700 Ω to 720 Ω, in ambient conditions. The micro-Pirani was supplied with 4.9 V so the current supplied initially to the resistive meander was 7 mA. Figure 6.9 shows the circuit used to ensure the micro-Pirani was kept at a constant resistance and the Wheatstone bridge balanced.
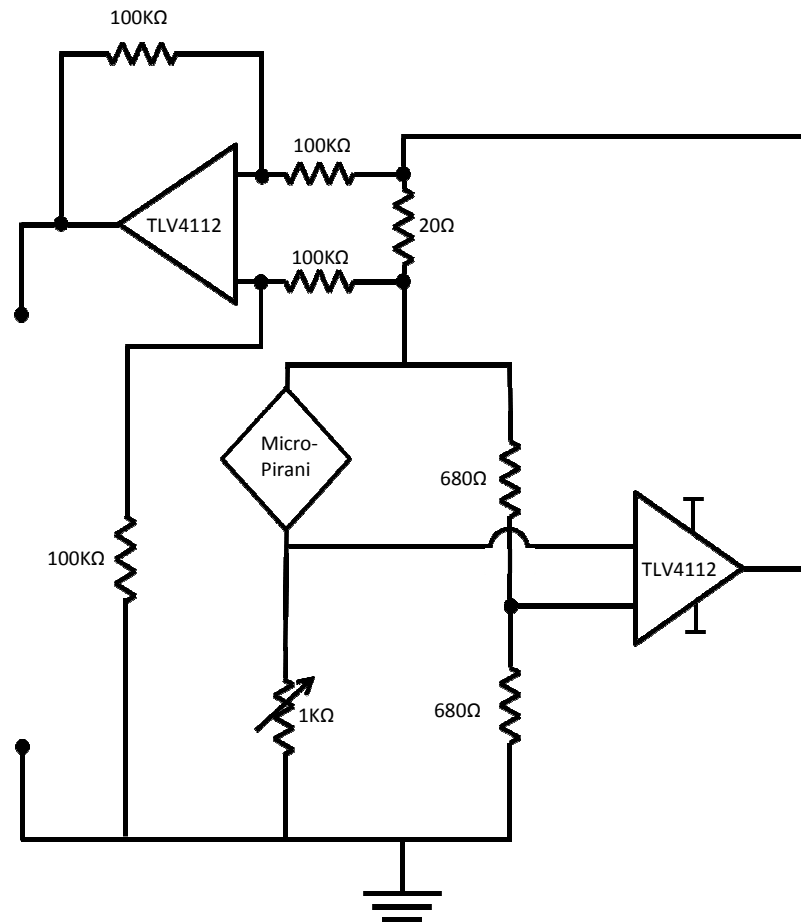

Figure 6.9: Micro-Pirani test circuitry.

The test circuit was designed so that when the resistance, hence temperature, of the micro-Pirani changes, the induced bridge voltage causes a potential difference across the input of the op-amp used as a comparator. The load draws a current from the op-amp, which is proportional to the change in bridge voltage, hence the change in the micro-Pirani resistance. This current is then fed back to balance the Wheatstone bridge and converted to a proportional voltage which can be measured using a voltmeter. This is the output voltage, which is measured for calibration purposes as the pressure surrounding the micro-Pirani is reduced. This voltage, $V_{measured}$, is related to the constant resistance of the micro-Pirani and the changing supply current by Ohm's law:

$$V_{measured} = I R_b \qquad (6.21)$$

where I is the current fed back into the test circuit to maintain the resistance, hence temperature, of the micro-Pirani and to balance the Wheatstone bridge. R_b is the constant micro-Pirani beam resistance when the constant temperature monitoring strategy is employed. Writing back equation 6.19 derived in section 6.1.1,

$$V_{measured} = \sqrt{R_b (a + b p_c) \Delta T} \qquad (6.19)$$

gives an analytical expression for the measured voltage, $V_{measured}$, where a and b are the geometry and material constants as described in section 6.1.1, p_c is the cavity pressure and ΔT is the difference in the beam and cavity temperature, a constant using the constant temperature monitoring strategy.

In the calibration experiment the ambient pressure surrounding the micro-Pirani was reduced to 10^{-5} mbar (9.869×10^{-9} atm) then increased steadily to atmosphere using the leak valve. The vacuum pump was continually evacuating the chamber so the leak valve was used to maintain the vacuum level during measurement.

6.2.4   Results

Figures 6.10 to 6.12 show the results of three different test chips. Measurements were carried out 3 times showing average results and are compared to the theoretical results

calculated using equation 6.17 where curve fitting has been used to determine the variables *a, b* and *ΔT*.
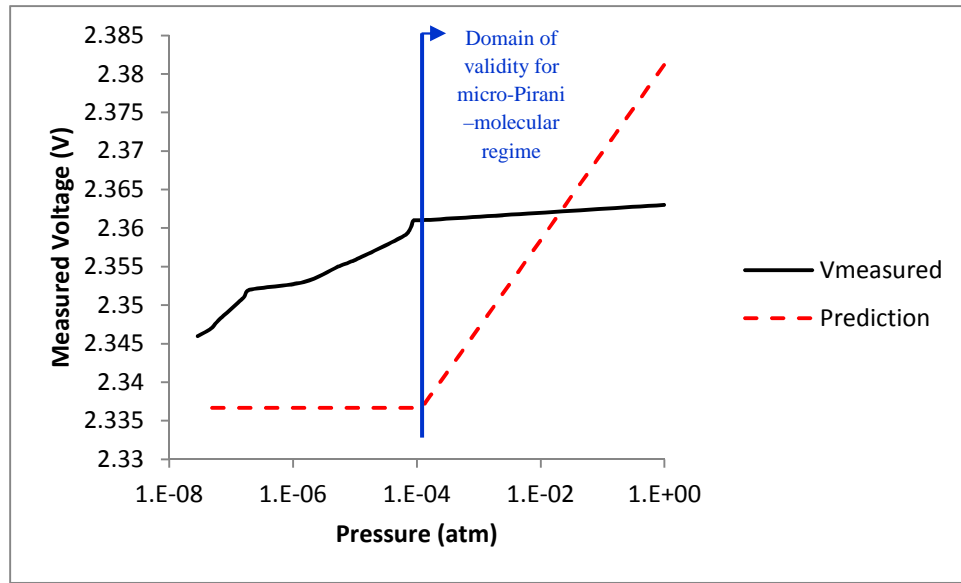

Figure 6.10: Chip 1, measured voltage as a function of cavity pressure. Error bars are shown in figure 6.13.
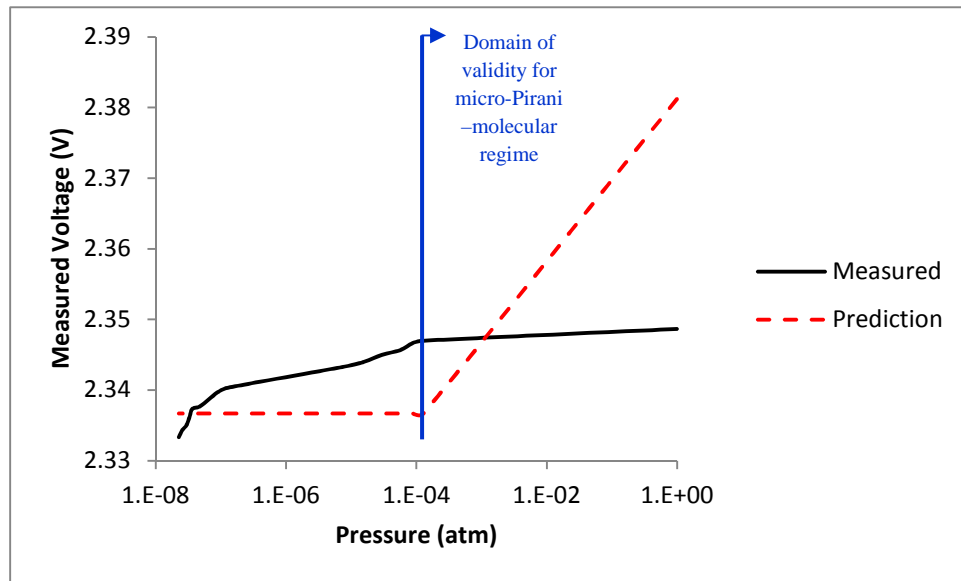

Figure 6.11: Chip 2, measured voltage as a function of cavity pressure. Error bars are shown in figure 6.13.
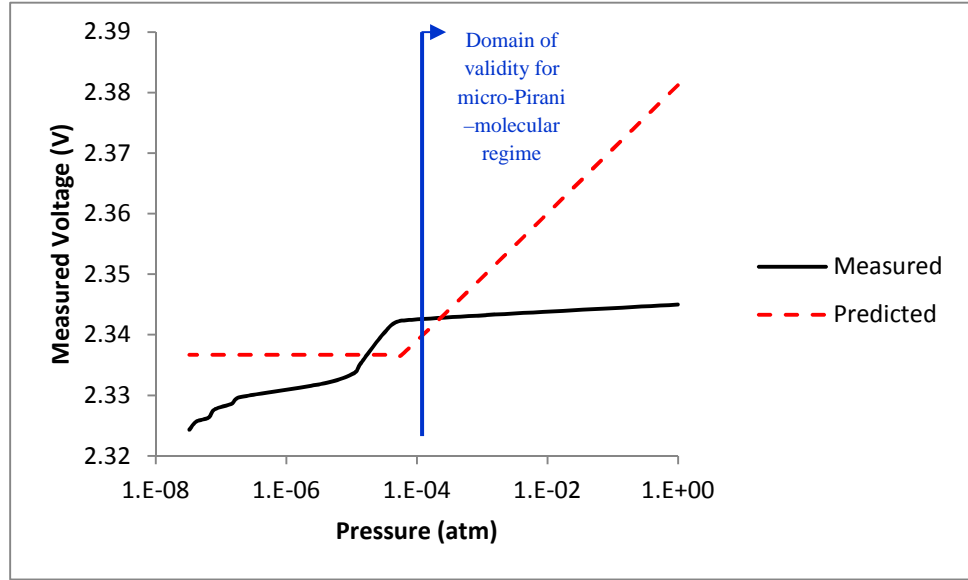
Figure 6.12: Chip 3, measured voltage as a function of cavity pressure. Error bars are shown in figure 6.13.

The predicted measured voltage indicated in figure 6.10 to 6.12 by the dashed red line was obtained using the theory given in section 6.1.1. Comparing equation 6.2, written back here for clarity, to Fourier's Law, shown here as equation 6.22, constant a is equivalent to the thermal conductivity, k, of the structure multiplied by the cross-sectional area, A, through which conduction is possible.

$$P_2 = a(T_b - T_c) \tag{6.2}$$

$$\Delta P = kA\Delta T \tag{6.22}$$

Multiplying the appropriate cross sectional area of the designed micro-Pirani by the thermal conductivity of the substrate given by the manufacturers to be 156 $Wm^{-1}K^{-1}$ gives constant a equal to 2.01×10^{-5} WmK^{-1}. Comparing equation 6.1, written back here for clarity, to Newton's law of cooling, shown here as equation 6.23, constant b is equivalent to heat transfer coefficient, h, multiplied by the surface area exposed to the ambient environment, A, per Pascal of pressure, p_c.

$$P_1 = bp_c(T_b - T_c) \tag{6.1}$$

$$\Delta P = -hA\Delta T \tag{6.23}$$

153

The heat transfer coefficient of air is known to be approximately 10 Wm^2K^{-1}. Multiplying this by the surface area of the micro-Pirani meander and dividing by atmospheric pressure gives constant b equal to 5.95×10^{-11} $Wms^2kg^{-1}K^{-1}$. The calculated values of constants a and b were used as the initial values, ΔT was initially set at 20°C, 293K, and the data was then fitted to equation 6.19. Constants a, b and ΔT were found to be 2.6×10^{-5} WmK^{-1}, 1×10^{-11} $Wms^2kg^{-1}K^{-1}$ and 300K respectively using least squares fitting set around the calculated value of a and b and the estimated value of ΔT.

Figures 6.10 to 6.12 show that according to the theory of the micro-Pirani, the designed test structure should be far more sensitive in the range 1×10^{-4} atm to ambient atmosphere. The lack of sensitivity of the test structure in this range is thought to be due to the fact that the metal meander of this design could not be released from the membrane due to the design rules of the fabrication process. In this design the meander is fabricated on a 23.1 μm thick membrane, which will conduct some heat from the metal meander, reducing heat convection and hence the test structures sensitivity to changing ambient pressure.

Substituting the values of the constants and the pressure range (in Pascals) into equation 6.19, the micro-Pirani gauge designed here is only sensitive to change of pressure in the range of 1 atm to 1×10^{-4} atm. Since the constant b is of the order 10^{-11}, the term in which it appears in equation 6.15 becomes insignificant when the pressure by which it is multiplied drops below 10 Pa or 1×10^{-4} atm. Therefore, below this pressure, one is outside the molecular regime and the output of the micro-Pirani is not pressure dependant. From figures 6.10 to 6.12 a change in the measured voltage can however be observed at pressure below 1×10^{-4} atm. Assuming that the stress in the region connecting the membrane to the bulk silicon is in compression, the membrane itself may not be perfectly parallel to the substrate. As surface resistors are used in the design and these have some piezoresistive qualities, it is possible that deflections of the membrane throughout the calibration procedure have caused changes in resistance, which are not due to heat convection at lower pressures. Measurements of the pressure using this test structure at pressure below 1×10^{-4} atm should therefore not be trusted.

Considering the valid range of pressures only, figure 6.13 shows the average response of three micro-Pirani test chips to changing ambient pressure. The error bars reflect the error calculated from the measurements of three test runs made for each chip. The error in the measurement is small, an average of 0.028 %, corresponding to a change of ± 0.6 mV. Since the change in measured voltage across the four orders of magnitude pressure range is only 2 mV this error is however significant. This error could be reduced by improving the calibration method. The pressure in the chamber was reduced using a vacuum pump, which was constantly running. A leak valve was used to hold the pressure of the test chamber to allow the measurement to be taken. To improve the calibration the test chamber should be evacuated to the appropriate level of vacuum and sealed before the measurements from the test chip are recorded. This would ensure that the environment in which the calibration is conducted is at a constant known pressure. The current calibration technique may be introducing a transient pressure around the micro-Pirani caused by the leak valve. The chip-to-chip variation in the results is ±0.03 V, an error of 1.3 %, individual chip calibration would therefore be required.
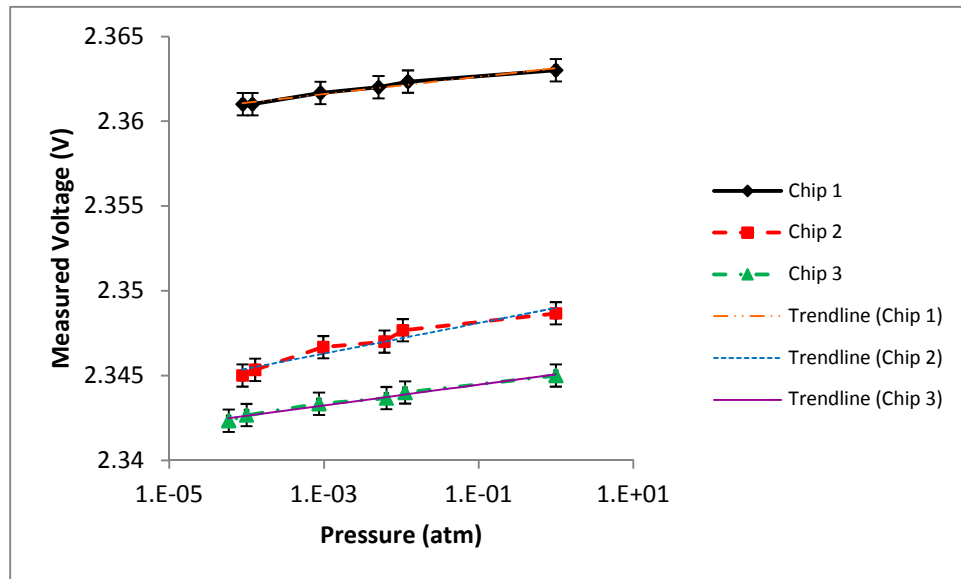
Figure 6.13: Average measured voltage as a function of cavity pressure.

The average sensitivity of the three test structures calibrated is 2.25 mV/atm. This structure is an order of magnitude less sensitive than the cap deflection test structure described in Chapter 5. The theory indicates that a similar micro-Pirani test structure with the meander released from the membrane could have a sensitivity of 45.1 mV/atm. To try to increase the change in voltage required to maintain the temperature hence resistance of the micro-Pirani, the initial temperature of the micro-Pirani structure was

increased by increasing the supply voltage. When the supply voltage was increased beyond 5 V, the micro-Pirani test structure failed. The increase in temperature increased the stress in the structure causing a break at the joint between the membrane on which the meander was fabricated and the substrate. As previously discussed this was the area of greatest stress in the design. The design of this test structure should therefore be modified in order to achieve a greater sensitivity.

Other groups have fabricated micro-Pirani gauges which have been used as hermeticity test structures with sensitivities great enough to measure leak rates of packages with cavity volumes of 1×10^{-5} cm^3 of the order 10^{-14} atm.cm^3.s^{-1} when tested in ambient conditions over an hour [6.2]. This is comparable to the sensitivity of the cap deflection test structure described in Chapter 5. Design iterations to improve sensitivity of this test structure are therefore required. The design rules of the MulitiMEMS process made it difficult however to fabricate the micro-Pirani structure in the most sensitive manner but improvements could still be made using this typical foundry process.

6.2.5 Future work

The use of a micro-Pirani gauge for hermeticity testing has been actively researched by several research groups [6.1, 6.2, 6.3]. Future work will include optimisation of the structure for greater sensitivity and improvement of the calibration method. The most important property of the micro-Pirani when used to monitor hermeticity of such packages is the sensitivity of the device at low pressure. Figure 6.14 shows a schematic of a second design of the micro-Pirani, which would increase the sensitivity of the test structure. The MultiMEMS design rules have been taken into consideration and less than 30% of the overall area would be release etched. The overall length of the meander of the micro-Pirani is less but this allows the release of the space between the arms of the meander minimising heat conduction loses. The connection to the substrate has also been changed from a 45° angle to a 90° angle which would provide a stronger connection allowing for a better yield and making the device more reliable. The N-well region should be left beneath the surface conductor in this area so that the thickness in this join is 23.1 μm after backside etching rather than 3.1 μm. Removing the surface resistors and replacing this with surface conductor beneath the metal conductor meander as stipulated by the design rules will remove any errors in measurement caused by the piezoresistive effects of the surface resistors.
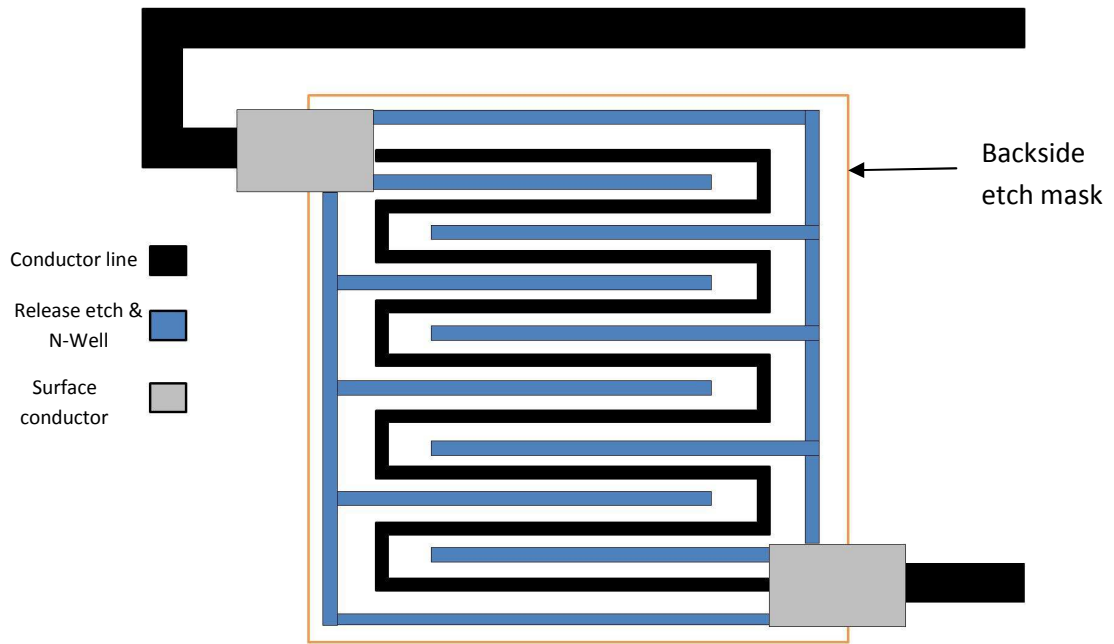
Figure 6.14: Schematic of a new micro-Pirani design.

Future work will also include reducing the footprint of the device to ensure that less chip real estate is used by the in situ test structure. As the trend towards smaller devices continues, the market will not accept a significant increase in chip size to accommodate a test structure unless this test structure could be accommodated into the lid of the package itself, which, at the moment, does not have functional structures.

6.3   Thermal van der Pauw in situ test structure

6.3.1   Theory

The principle is similar to that of the micro-Pirani test structure whereby the structure is heated and the difference in the temperature increase recorded is dependent on the ambient pressure surrounding the structure. To explain the thermal van der Pauw operation, the electrical Greek cross test structure is firstly considered. Figure 6.15 shows a schematic of both the electrical Greek cross and the thermal van der Pauw operating principles.

Figure 6.15: (a) Operating principle of the electrical Greek cross (b) Operating principle of the thermal van der Pauw

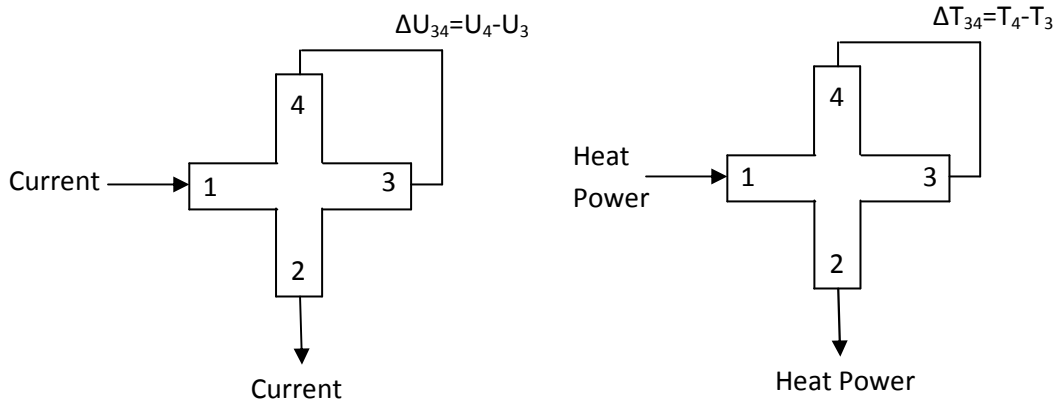A current is applied across two adjacent arms of the electrical Greek cross structure and the potential difference across the opposite adjacent arms is measured [6.4]. The electrical sheet resistance is then extracted. In the thermal case a heat power or current is applied across two adjacent arms and the temperature or resistance change across the two opposite adjacent arms is measured [6.4]. Ordinarily the thermal sheet conductivity is then extracted but, when used as a hermeticity test structure, the change in resistance should be maximised to ensure that the structure is sensitive to changing ambient pressure. As in the case with the micro-Pirani structure, this structure will only work in the molecular regime of gaseous convection where thermal conductance is pressure dependent [6.1].

6.3.2 Design

Figure 6.16 shows the design of the thermal van der Pauw hermeticity test structure. One thermal van der Pauw test structure was fabricated in the bottom left hand corner of the 6 mm x 6 mm chip. The masks for the different layers contained in the thermal van der Pauw structure were drawn according to the design rules and in the order described in section 6.2.2. The outermost square defined in figure 6.16 (b) was the backside etch mask, which was used to form the thin membrane on which the van der Pauw structure is fabricated.

(a)   *(b)*
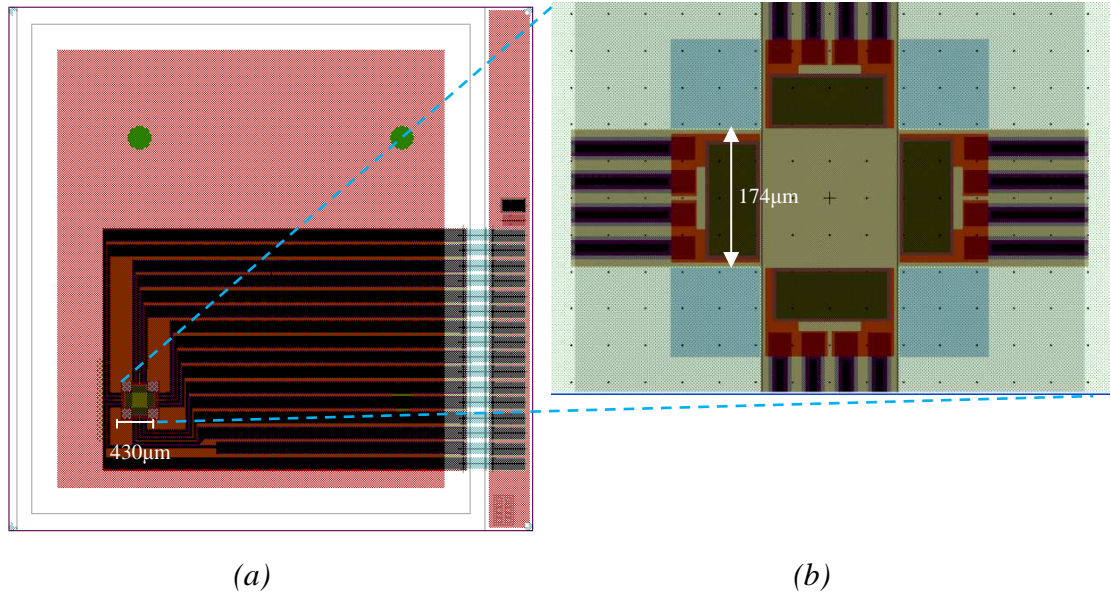
Figure 6.16: Thermal van der Pauw Design (a) full die (b) Greek cross.

The 690 µm x 690 µm N-well mask was set inside the backside etch mask and was drawn in the region where the N-well was not required to enable the fabrication of the thin membrane. The squares in the corners of the thermal van der Pauw structure represent the release mask which, as described in section 6.2.2, had negative polarity and was therefore drawn where the release etch was to take place. The arms leading to the central cross consist of four independent lines of surface conductor and metal conductor with a defined contact hole for electrical connection. The independent conductor lines on each arm of the structure provide four-point connection to a surface resistor at the intersection of the cross. Figure 6.17 shows the meandering layout of the surface resistors. A rectangular metal plate was defined over the surface resistor with contact hole for electrical connection to ensure that the heat was dissipated homogenously.
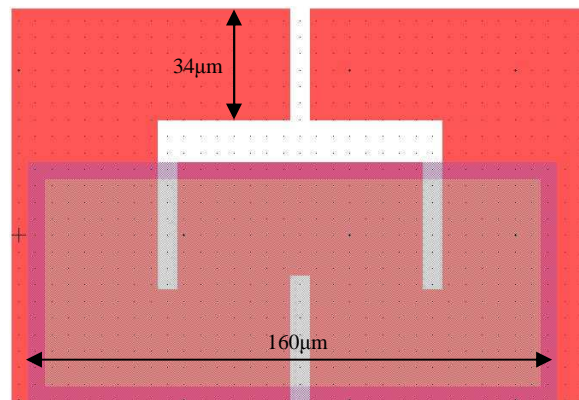
Figure 6.17: Surface resistor and metal cap mask design.

159

As with the micro-Pirani test structure an anodic bonding mask was defined over the thermal van der Pauw structure to ensure the thin oxide layer remained and no bonding would take place over the test structure. The top glass has an etched cavity to allow the test structure freedom to move. The bottom glass is bonded with holes to allow access to the internal cavity.

Figure 6.18 shows the maximum stress in the thermal van der Pauw test structure designed was 157.45 MPa. The stress did not exceed the maximum tolerance given by MultiMEMS, 500×10^6 N/m^2, and the design passed the design rule checker so was accepted for fabrication.
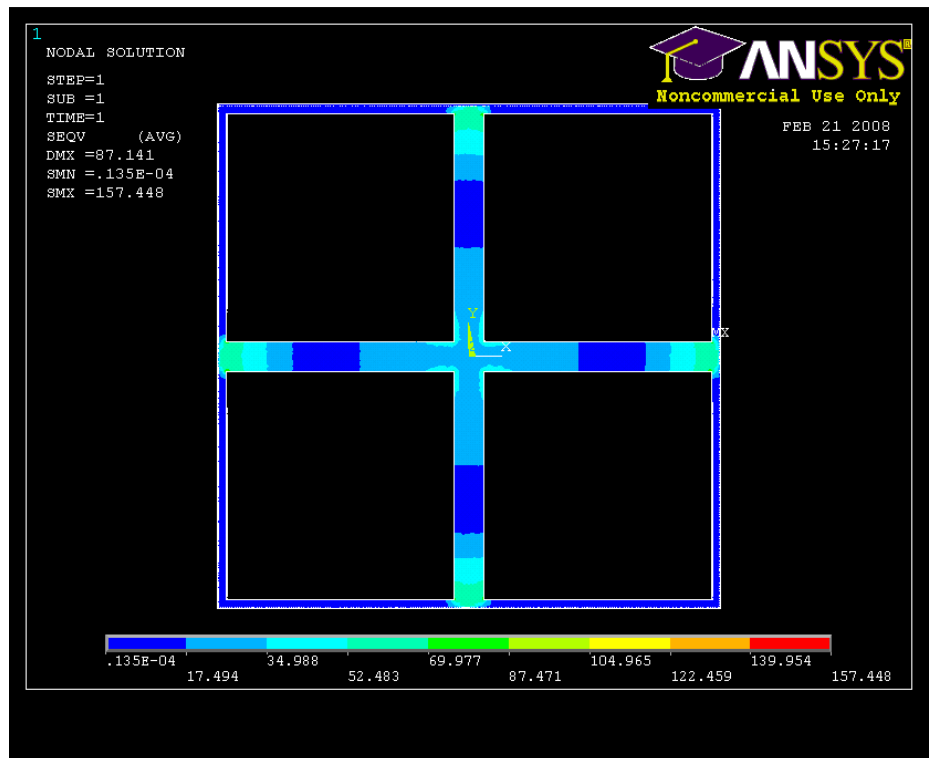
Figure 6.18: ANSYS simulation of stress in design of thermal van der Pauw in situ test structure.
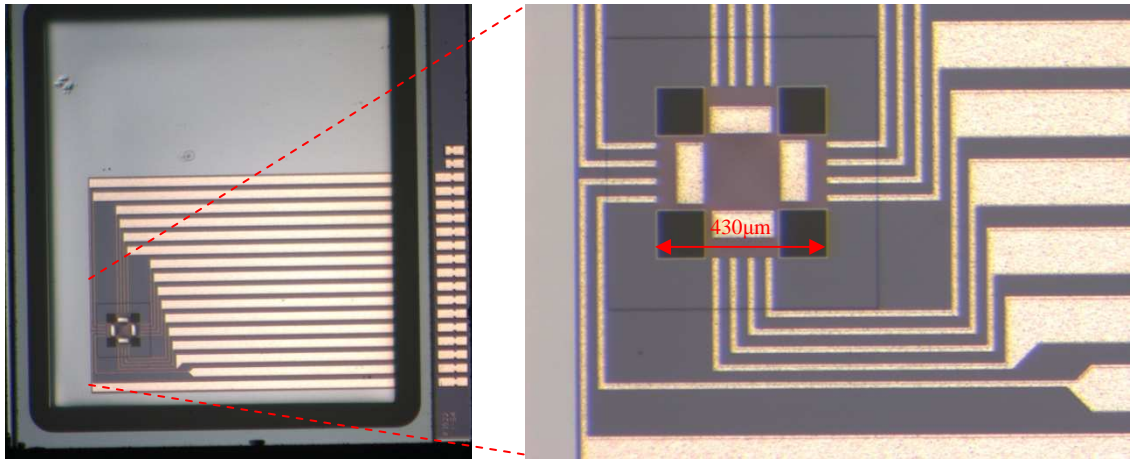
Figure 6.19: Microscope photograph of fabricated thermal van der Pauw test structure.

6.3.3   Results

It was not possible to direct heat power into or out of the Greek cross at the centre of the thermal van der Pauw test structure. It was however possible to use one resistor as a heater and measure the change in resistance, hence temperature, across the other three resistors as well as the heated resistor itself since it was connected in a four point configuration. Each test structure could therefore be tested four times increasing the reliability of the extracted data.

Before a test circuit for calibration of the thermal van der Pauw structure could be designed, it was necessary to measure the resistance of each resistor at room temperature in ambient pressure. When this test was conducted it was found that the resistance in each arm of all three wirebonded and electrically connected test chips varied over time significantly by as much as 40 %.

After examining the design and the MultiMEMS handbook, it was found that surface resistors and piezoresistors are formed in the same way. The only difference in the layout of surface resistors designed for use as heaters and those designed for use as piezoresistors is the orientation [6.5]. Piezoresistors should be oriented along the <110> crystallographic direction as the coefficients of piezoresistivity exhibit their maximum values in this direction. Surface resistors indended for use as heaters could be oriented any way [6.5]. It was therefore clear that the surface resistors used in the thermal Van der Pauw structure were acting as piezoresistors and since the cavity was open to the

161

ambient environment, the cross was moving freely causing the values of resistance to change dramatically.

It was not possible to test the thermal van der Pauw as a hermeticity test structure due to the fact that the resistance change was varying due to piezoresistive effects and not due to temperature change.

6.3.4 Future work

Future work includes research to determine whether or not redesigning this test structure using the MultiMEMS design rules is possible. It would be advantageous to find another way to create the heater in the thermal van der Pauw structure so that deflection of the cross under varying pressures and through handling of the device itself are not an issue.

6.4 Summary of in-situ test structures

Two in-situ test structures were designed to monitor internal cavity package pressure for hermeticity testing purposes.

The micro-Pirani test structure fabricated suffered from a design fault which caused the membrane on which the micro-Pirani was fabricated to break from the substrate during dicing, causing yield issues. The results of three chips were collated and it was found that the design was not as sensitive as the cap deflection test structure. However, with some design iterations to improve yield and release the meander from the membrane, this type of test structure could be more sensitive and prove to be a beneficial addition to the portfolio of test techniques for low cavity volume packages.

The thermal van der Pauw test structure could not be calibrated since the resistors used as heating elements had piezoresistive properties so when the pressure inside the cavity was changed, the membrane on which the resistors were placed deflected and the change in resistance due to heat convection could not be extracted independently of the change due to mechanical movement. The thermal van der Pauw test structure does theoretically offer the advantage of multiple testing from one structure making it an

162

attractive design for use as an in situ test structure. Future work to determine the range and sensitivity of the thermal van der Pauw test structure includes design iterations and a change in fabrication process.

One of the advantages of using in-situ test structures for leak detection is that the structure is inside the package so no false positive or false negative testing is possible as can be the case with some external test methods such as the helium fine leak test. They will measure leak rates caused by gas flow through leak channels, permeation or outgassing although it is not always possible to distinguish between these initially. However, if a leak is present, monitoring the leak rate over time will indicate the leak mechanism; a leak caused by gas flow through a leak channel will continue until the pressure inside the package equals the pressure outside but this rate will slow as the pressure difference is reduced. A permeation leak will take some time to show since the gas must first be absorbed onto the package material surface, then diffuse through the material and finally desorbs inside the package before it will affect the test structure; and a leak rate caused by outgassing will generally not be apparent until during or after high temperature bonding. The curve of cavity pressure change over time for each type of leak is different so the leak type present can be deduced from the output data of the test structure over time.

All of the designed in-situ test structures described in this thesis give an electrical response to changing ambient pressure. This is advantageous in industry as electrical tests can be conducted on wafer making them quick and cheap. These test structures can be used to monitor internal cavity pressure during accelerated testing and at any stage throughout the device lifetime for health monitoring purposes or as a failure analysis technique. Further iterations of these in-situ test structures should not only reduce the footprint required but lead to improved sensitivity and a wider operating range.

Table 6.1 is carried forward from Chapter 4 and the results of the newly characterised in-situ test methods included in this chapter and the cap deflection technique described in Chapter 5 are highlighted in blue. In-situ test structures designed by other researchers have also been added. This table should be used as a living document and updated as the current test methods are improved and new test methods are discovered.

Test Method	Detectable range limitations	Practical limitations	Leak types detected	Suitable package materials	Unsuitable package materials
Helium fine leak	Volume limitation: $> 2.6\times10^{-3}$ cm^3 Min. detectable leak rate: 1.28×10^{-10} atm.cm^3.s^{-1}	Increased dwell time required when surface sorption present causing larger volume limit	Leak channels: molecular leaks	Silicon Metals Ceramics	Polymers Glass Epoxies
Radioisotope fine leak	Min. detectable leak rate: 10^{-12} atm.cm^3.s^{-1}	Licensing, handling and disposal of radioisotopes	Leak channels: Molecular and viscous (combinational test)	Silicon Metals Ceramics Glass	Polymers Epoxies
Optical leak detection	Min. detectable leak rate: 10^{-10} atm.cm^3.s^{-1}	Calibration of every package type required	Leak channels Permeation (of tracer gas)	Any material as long as cap thickness and flexibility is appropriate	Rigid cap materials.
Cumulative helium leak detection	Min. detectable leak rate unclear: $10^{-10} - 10^{-14}$ atm.cm^3.s^{-1}	Calibrating system to ensure lowest possible detection limit	Leak channels	Silicon Metals Ceramics	Polymers Glass Epoxies
Residual gas analysis	10^{-16} depending on MS sensitivity	Destructive and very expensive	Leak channels Permeation Outgassing	Any material	n/a
FTIR leak detection	Volume limitation: $> 7.36\times10^{-4}$ cm^3 Min. detectable leak rate: depends on sample and experimental parameters, typically, 10^{-11} atm.cm^3.s^{-1}	Min. detectable leak rate and volume limitations dependent on min. partial pressure measurement which is sample dependent and must be calibrated	Leak channel: molecular leak (Howl-Mann method) Permeation – rate cannot be converted to equivalent standard leak	Silicon Some glass	IR absorbing glass Polymers Ceramics Epoxies Non IR transparent metals (for N$_2$O tracer gas Howl-Mann method)
Raman spectroscopy	n/a distinction between fine and gross only	Slow test procedure can be improved by increased signal to noise ratio.	Leak channels Permeation Outgassing	Glass Silicon IR/visible or UV transparent polymers and epoxies	Ceramics IR/visible or UV non-transparent polymers and epoxies
Q-factor testing	10^{-14} atm.cm^3.s^{-1}	Requires calibration before packaging using impedance analyser or LCR meter	Leak channels Permeation Outgassing	Any package material but device must be resonant	All packing materials are suitable
Neon Ultra-fine leak test	9.86×10^{-17} atm.cm^3.s^{-1}	Requires calibration before packaging using ring-down method	Leak channels Permeation	Any package material but must be resonant	All packing materials are suitable

Test Method	Detectable range limitations	Practical limitations	Leak types detected	Suitable package materials	Unsuitable package materials
Copper test patterns	4.935×10^{-16} atm.cm^3.s^{-1}	Slow test procedure can be accelerated using bombing technique and increasing temperature. Bombing gas must contain oxygen	Leak channels Permeation (of O$_2$)	Optically transparent cap material – silicon, some glass	IR absorbing glass Polymers Ceramics Epoxies Non IR transparent metals
Cap deflection in situ test structure	10^{-15} atm.cm^3.s^{-1}	Flexible cap with piezoresistors connected in Wheatstone bridge required but no chip real estate needed. Subsequent packaging required for mechanical protection.	Leak channels Permeation Outgassing	Any subsequent packaging material suitable	All subsequent packing materials are suitable
Micro-Pirani in situ test structure	10^{-14} atm.cm^3.s^{-1}	Space on chip required for test structure	Leak channels Permeation Outgassing	Any package material	All packing materials are suitable
Thermal van der Pauw in situ test structure	To be determined	Space on chip required for test structure	Leak channels Permeation Outgassing	Any package material	All packing materials are suitable

Table 6.1: Summary of hermeticity test methods

6.7   References

[6.1]   C. H. Mastrangelo, Ph.D. Thesis, *'Thermal Applications of Microbridges'*, Berkeley, CA, 1991.

[6.2]   B.H. Stark, J. Chae, A. Kuo, A. Oliver and K. Najafi, *'A high performance surface-micromachined Pirani gauge in SUMMIT V^{TM}'*, Proceedings of 18th IEEE Conference on Micro Electro Mechanical Systems, pp 295-298, 2006.

[6.3]   X. Wang, C.Liu, Z. Zhang, S. Liu and X. Luo, *'A micro-machined Pirani gauge for vacuum measurement of ultra-small sized vacuum packaging'*, Sensors and Actuators A, 161, pp108-113, 2010.

[6.4]   O. Paul, L. Plattner and H. Baltes, *'A thermal van der Pauw test structure'*, Proceedings of IEEE International Conference on Microelectronic Test Structures, 12, pp. 56-61, 1999.

[6.5] S. Hafizovic and O. Paul, *'Temperature-dependant thermal conductivities of CMOS layers by micromachined thermal van der Pauw test structures'*, Sensors and Actuators A, 97-98, pp. 246-252, 2002.

Chapter 7

Conclusions and Future Work

7.1   Summary and Conclusions

The research and development work undertaken and presented in this Engineering Doctorate thesis was conducted for use by the author's sponsoring company MCS Ltd. MCS Ltd offer failure and materials analysis, most often but not exclusively to the electronics and microelectronics industries. MCS Ltd had a desire to work also in the MEMS industry. For this reason, before work commenced, it was essential to establish that there was a demand for a hermeticity service in the MEMS and Microelectronics industries. The market survey, available in Appendix C, shows that hermeticity testing was indeed of interest to potential customers of MCS Ltd and so research commenced. The aim of this research was multifold: (1) to gain sufficient knowledge of the theory of hermeticity testing to sell this knowledge in the form of consultancy through MCS Ltd, (2) to develop further several currently available hermeticity test methods for application to MEMS and small cavity volume packaging devices and (3) to develop novel ex-situ and in-situ test structures. This work has been conducted as a series of small projects with a common theme, hermeticity of MEMS and microelectronic packages, within the scope of the Engineering Doctorate to address the business needs of the sponsoring company, MCS Ltd.

7.1.1   Research findings

To better understand the complex nature of hermeticity testing of packages with ultra low internal cavity volumes, the leak types typically present in MEMS and microelectronic packaging have been described and are considered when assessing the applicability of each hermeticity test method. The existing leak detection techniques have been scrutinised to establish their limits when applied to low cavity volume packages and packages made using new types of materials for various applications. It is the first time that a comprehensive table of the different technologies has been drawn up with their potential detection sensitivities in terms of minimum detectable leak rate.

167

Moreover, through the use of the Lambert-W function, it has been possible to provide a closed form expression of the upper limit of validity of the Helium fine leak test, which is intended to help practitioners in pushing this commercial hermeticity test method to acceptable limits.

Two optical test techniques, FTIR and Raman spectroscopy have been investigated with regards to their applicability to replace the traditional leak test methods for some MEMS and microelectronic applications for which traditional test techniques are unsuitable. The FTIR method has proven to be a useful method to determine the molecular leak rate of packages containing glass. Raman spectroscopy can be used to qualitatively determine any leak type; molecular, permeation or outgassing. No external test method has been proven to have the sensitivity required to detect, in a non-destructive manner, the ultra low leak rates that adversely affect some MEMS devices.

Three different in-situ test structures were therefore considered: a micro-Pirani, a thermal Van der Pauw and a piezoresistive cap deflection test structure were designed to give an electrical response to changing ambient pressure. The cap deflection technique proved to be the most sensitive test structure fabricated although it is expected that design iterations would improve the sensitivity of the micro-Pirani test structure. The thermal van der Pauw test structure requires significant further work to determine practically the applicability of this structure as a hermeticity test structure. A table providing a complete summary of new and existing hermeticity test methods was provided in chapter 6 and therefore not reproduced here. Table 7.1 however, is a more user-centric table and shows a summary of all commercially available and researched hermeticity tests methods according to package materials and leak types.

7.1.2   SEMI standards

The standards currently used have proven to be somewhat out-of-date particularly where sample cavity volumes are concerned. Throughout this study, the author has contributed as part of an international task force towards a set of new standards for hermeticity testing of MEMS packages. A draft copy of the SEMI permeation standard due for publication in late 2011 can be found in Appendix E.

The author will continue to work with the Task Force to complete the permeation standard and write a further hermeticity testing standard focussed on outgassing.

7.1.3   *Hermeticity testing at MCS Ltd.*

As part of the Engineering Doctorate, it was necessary to transfer the knowledge gained through conducting this work to the sponsoring company, MCS Ltd. The information contained within this thesis has been disseminated to the company on several occasions. Two journal papers and two peer reviewed conference papers have been written with MCS Ltd and published. A white paper has been written and posted on the company's website to describe the issues concerning the traditional test methods and details of the expertise and test technique offered by MCS Ltd. This white paper is available in Appendix D.

The author will continue to work with MCS Ltd on a consultancy basis for hermeticity testing and other MEMS relating failure analysis techniques.

Package Material Seal Type Leak Type	Package/Test Requirements		Hermeticity test
Metal/ceramic package 'Hermetic seal' Molecular leak	$V \geq 0.052$ cm^3	$L_{min} > 1.28 \times 10^{-10}$ atm.cm^3.s^{-1}	Helium fine leak with gross test, Radioisotope leak test, CHLD, Optical leak test, FTIR, In-situ
		$L_{min} < 1.28 \times 10^{-10}$ atm.cm^3.s^{-1}	Radioisotope, CHLD, FTIR, In-situ
	2.6×10^{-3} cm$^3 \leq V \leq 0.052$ cm^3	$L_{min} > 1.28 \times 10^{-10}$ atm.cm^3.s^{-1}	Helium fine leak with gross test (dwell < 3 mins), Radioisotope leak test, CHLD, Optical leak test, FTIR, In-situ
		$L_{min} < 1.28 \times 10^{-10}$ atm.cm^3.s^{-1}	Radioisotope, CHLD, FTIR, In-situ
	$V \leq 2.6 \times 10^{-3}$ cm^3		Radioisotope, CHLD, Optical leak test, FTIR, In-situ
Packages containing glass Molecular leak			Radioisotope, FTIR, In-situ
Near-hermetic Polymer seals Permeation leak	Qualitative		FTIR, Radioisotope, Raman
	Quantitative		In-situ
Any packaging Any seal Outgassing	Qualitative		Raman, In-situ, RGA
	Quantitative		In-situ, RGA

Table 7.1: Recommended hermeticity test methods dependent on package type, leak types and hermeticity requirements

7.2 Future Work

7.2.1 FTIR and Raman spectroscopy techniques

Future work concerning the use of FTIR spectroscopy as a hermeticity test technique includes the calibration of the air leak of a near hermetic package which contains permeable materials to the measured nitrous oxide leak rate. To do this a case-study should be carried out where in-situ pressure sensors are near-hermetically packaged and tested using FTIR spectroscopy in the future. For calibration purposes, one set of these packages should be bombed in nitrous oxide at the desired pressure for the desired length of time. The remaining packages should be bombed in air at the same pressure for the same length of time. The pressure sensor output should be monitored over time to determine the calibration factor necessary to determine the air leak rate from the nitrous oxide leak rate. This calibration factor will be unique to the package type tested and re-calibration must be performed for differing package dimensions and materials.

The FTIR test method should also be conducted on the packages bombed in nitrous oxide to determine the accuracy of the FTIR method in determining the partial pressure of tracer gas within packages and hence leak rates. Future work also includes investigating the use of different tracer gases with different infra-red absorption peaks for use with different packaging materials.

The Raman spectroscopy technique should be investigated using a suitable objective lens which allows the incident light to be focussed within the cavity. Work should be continued to determine whether a sufficient signal to noise ratio can be achieved to make the method quantitative. It is expected that work on this technique will continue within the MISEC group and with support from Renishaw Plc through a feasibility study. This method has a potential to be used on-line as a failure analysis technique.

7.2.2 Hermeticity test structures

Future work concerning the piezoresistive cap deflection test structure includes placing the piezoresistors on the highest stress regions of the membrane, i.e. the edges. This will increase the sensitivity of the test structure. This test technique should be used on a

suitable prototype device to determine the usefulness of this test technique when compared to traditional hermeticity test methods.

Design iterations are required for the micro-Pirani test structure. The meander should be released from the membrane and be completely freestanding to ensure maximum heat convections and therefore sensitivity as a pressure sensor. The footprint of the test structure should also be reduced to ensure that minimum chip real-estate is used for the in-situ test structure. It would be advantageous to make a nanoscale size free standing meander, potentially even reducing the traditional micro-Pirani sensor to a single carbon nanotube or a nano-wire.

An alternative fabrication technique for the thermal Van der Pauw test structure is required which uses stress independent resistors as heaters. This test structure measures pressure by monitoring the temperature change due to heat convection. The sensitivity of the structure fabricated here was adversely affected by the piezoresistive properties of the resistors used. Further work is required to determine if this test structure is valid for use as an in-situ hermeticity test structure.

7.2.3   Electrical Breakdown test structure

In-situ test structures based on electrical breakdown are a novel concept developed by the author of this thesis in collaboration with her supervisor, Prof. Marc Desmulliez. The concept uses the fact that electrical breakdown at micron separations occurs at relatively low voltages and does not obey Paschen's law [7.1]. The potential required to achieve breakdown is pressure dependent and so a test structure can be designed to monitor the pressure within cavities and hence be used as an in-situ test structure.

Electrical breakdown occurs when the gas present surrounding two electrodes is ionised and subsequent collisions with other gas molecules leads to the gap between the electrodes being 'bridged'. Paschen's Law gives the voltage required to cause breakdown at the macro scale. The modified Townsend theory reflects the breakdown of Paschen's Law at small electrode separations [7.1, 7.2, 7.3]. Dhariwal et al. prove that in ambient air breakdown occurs at 12V when the electrode gap is 0.25 µm [7.1]. In his thesis, Torres investigated the effect of reduced pressure on electrical breakdown at micrometer separations [7.2]. As expected, the breakdown voltage increases when

pressure is reduced since the availability of gas molecules to be ionised is reduced and collisions are less frequent. Torres found that the breakdown voltage was almost pressure independent when the electrode space was less than 4 µm [7.2]. Above 10 µm, breakdown voltage follows Paschen's law, so for pressure dependent breakdown at low voltages the optimum electrode separation is between 4 µm and 10 µm.

It is expected that this technique will be best suited to MEMS devices since it would be challenging to use microelectronics CMOS processing techniques to fabricate free-standing electrodes. To enable multiple tests, the current which flows just before breakdown can be measured and the voltage can be stopped before catastrophic failure.

This work will be continued by Prof. Marc Desmulliez and a PhD student within the MISEC group at Heriot-Watt University.

7.3   References

[7.1]   R.S. Dhariwal, J.-M. Torres and M.Y.P. Desmulliez, *'Electric field breakdown at micrometre separations in air and nitrogen at atmospheric pressure',* IEE Proceedings Science, Measurement and Technology, 147(5) , pp. 261-265, 2000.

[7.2]   J.-M. Torres, PhD Thesis, *'Electrical breakdown at micrometer separations'*, Heriot-Watt University, UK, 2000.

[7.3]   M. Radmilović-Radjenović and B. Radjenović, *'An analytical relation describing the dramatic reduction of the breakdown voltage for the microgap devices'*, Journal of EuroPhysics Letters, 83, 2008.

[7.4]   R. Tirumala and D. B. Go, *'Analytical formulation for the modified Paschen's curve'*, Applied Physics Letters, 97, 2010.